Bernhard Obereder, BSc

Improvement of Current Ophthalmological MRI Methodology by Using the "medEyeTrack" System

Master's Thesis

Institute of Medical Engineering
Graz University of Technology
Kronesgasse 5, A - 8010 Graz
Head of the Department: Univ.-Prof.Dipl.-Ing.Dr.techn. Rudolf Stollberger

Supervisor:
Univ.-Prof.Dipl.-Ing.Dr.techn. Rudolf Stollberger

Evaluator:
Univ.-Prof.Dipl.-Ing.Dr.techn. Rudolf Stollberger

Graz, March 2014

EIDESSTATTLICHE ERKLÄRUNG

Ich erkläre an Eides statt, dass ich die vorliegende Arbeit selbstständig verfasst, andere als die angegebenen Quellen/Hilfsmittel nicht benutzt und die den benutzten Quellen wörtlich und inhaltlich entnommenen Stellen als solche kenntlich gemacht habe.

Graz, am ....
Name

STATUTORY DECLARATION

I declare that I have authored this thesis independently, that I have not used other than the declared sources/resources and that I have explicitly marked all material which has been quoted either literally or by content from the used sources.

....
date Name

Abstract

MR image quality in ophthalmological MRI can be substantially reduced by motion artifacts, which may hinder the reliable diagnosis as well as accurate radiotherapy treatment planning of uveal melanoma. There is still no known general method to prevent motion artifacts caused by movement of the eyes and blinking. Previous studies describe several approaches, including different fixation schemes and special MR sequences with blinking pauses, to minimize motion artifacts caused by eye movements and blinking with non-invasive methods. All these methods only achieved limited success. This work presents a new approach to prevent motion artifacts resulting from movements of the eye. The detectability of eye motion with an eye tracker (medEyeTrack) was used to trigger a 3D TurboFLASH sequence using the external trigger signal interface of an MR scanner. This new approach showed significant improvement in anatomical recognizability and reduction of the artifact level present in the resulting MR images. The achieved enhancement in image quality dramatically improves the accuracy of radiation therapy treatment planning. Results of this thesis will serve as an important basis for further work aiming to prevent motion artifacts in ophthalmological MRI imaging.

Keywords: medEyeTrack, motion, artifacts, magnetic resonance imaging, ophthalmology

Kurzfassung

Die MR-Bildqualität in der ophthalmologischen MRT kann durch Bewegungsartefakte stark reduziert werden und in Folge eine zuverlässige Diagnose sowie eine genaue Bestrahlungsplanung von Aderhautmelanomen stark beeinträchtigen. Derzeit ist keine allgemeine Methode bekannt, um Bewegungsartefakte, verursacht durch Augenbewegungen und Blinzeln, zu verhindern. Vorangegangene Studien beschreiben verschiedene nicht-invasive Methoden um Bewegungsartefakte durch Augenbewegungen und Blinzeln zu minimieren, darunter verschiedene Fixationsmethoden und spezielle MR-Sequenzen mit Blinzelpausen. Alle diese Verfahren erzielten nur begrenzte Erfolge. Diese Arbeit stellt einen neuen Ansatz zur Verhinderung von Bewegungsartefakten durch Augenbewegung vor. Die durch einen Eye Tracker (medEyeTrack) detektierten Augenbewegungen wurden verwendet um eine 3D TurboFLASH Sequenz zu triggern. Diese neue Methode zeigte eine signifikant verbesserte anatomische Erkennbarkeit und eine Reduktion von Artefakten in den resultierenden MR-Bildern. Die erreichte Verbesserung der Bildqualität erhöht die Genauigkeit der Behandlungsplanung der Bestrahlungstherapie drastisch. Die Ergebnisse dieser Arbeit dienen als wichtige Grundlage für weiterführende Arbeiten mit dem Ziel Bewegungsartefakte in der ophthalmologischen MR-Bildgebung zu verhindern.

Schlüsselwörter: medEyeTrack, Bewegung, Artefakte, Magnetresonanztomographie , Ophthalmologie

Danksagung

Ich bedanke mich bei Herrn Univ.-Prof. Rudolf Stollberger für die Ermöglichung und Betreuung dieser Arbeit. Danken möchte ich auch allen Institutsangehörigen für die tolle Zusammenarbeit und für anregende und spannende Diskussionen, allen voran bei Peter Opriessnig für seine tatkräftige Unterstützung bei all meinen Fragen. Bei Johannes Strasser möchte ich mich für seine Hilfestellungen und das Korrekturlesen dieser Arbeit bedanken. Auch bei Eva Haas möchte ich mich für die gute Zusammenarbeit und für die zahlreichen Male, die sie sich als Testperson zur Verfügung gestellt hat, bedanken.

Des Weiteren gilt mein Dank Herrn Dr. Gerhard Thallinger für die Unterstützung bei der statistischen Auswertung.

Ein großes Dankeschön auch an alle, die sich als Testpersonen für diverse Messungen zur Verfügung gestellt haben.

All dies wäre nicht möglich gewesen ohne meine Eltern Aloisia und Karl Obereder, die mir diese Ausbildung ermöglicht haben und mich immer bei meinen Entscheidungen unterstützt und bestärkt haben. Ihr Vertrauen und Ihr Glauben an mich machten mich stark. Ich widme ihnen diese Arbeit.

Im Speziellen möchte ich mich bei Kathrin Herzog bedanken, die mich in allen Belangen unterstützt wo sie nur kann und mich immer wieder nach vorne blicken lässt. Sie glaubt an mich, auch wenn ich das nicht mehr kann. Danke dafür.

Contents

List of Abbreviations

MRI	Magnetic Resonance Imaging
MR	Magnetic Resonance
B_0-field	Main Magnetic Field
B_1-field	Radio Frequency Magnetic Field
RF	Radio Frequency
SE	Spin Echo
TSE	Turbo Spin Echo
FLASH	Fast Low Angle Shot
SPACE	Sampling Perfection with Application Optimized Contrasts by Using Different Flip Angle Evolutions
VISTA	Volumetric Isotropic TSE
FFE	Fast Field Echo
IR-TFE	Inversion Recovery Turbo Field Echo
bSSFP	Balanced Steady-State Free Precession
STIR	Short Tau Inversion Recovery
FSE	Fast Spin Echo
FAISE	Fast Acquisition Interleaved Spin Echo
RARE	Rapid Acquisition with Relaxation Enhancement
GRASSE	Gradient Recalled Acquisition in the Steady State
MP-RAGE	Magnetization Prepared Rapid Gradient Echo
TrueFISP	True Fast Imaging with Steady State Precession
TE	Echo Time
TR	Repetition Time
FOV	Field Of View
ROI	Region Of Interest
SNR	Signal to Noise Ratio
OCT	Optical Coherence Tomography
US	Ultrasound
UBM	Ultrasound Biomicroscopy
CT	Computed Tomography
LINAC	Linear Accelerator
PTV	Planning Target Volume
ETL	Echo Train Length
ESP	Echo Spacing
NEX	Number of Excitations
TE_{eff}	Effective TE
SAR	Specific Absorption Rate
FID	Free Induction Decay
SOS	Sum Of Squares
TTL	Transistor Transistor Logic
ANOVA	Analysis of Variance
L7	Siemens 3 T Loop 7 cm coil
TFL	TurboFLASH
ECG	Electrocardiography

Chapter 1

Introduction

1.1 Motivation

There are several ophthalmologic methods for the evaluation of the small structures in the human eye such as slitlamp biomicroscopy [1], Scheimpflug photography [2], optical coherence tomography (OCT) [3] and ultrasound (US) or ultrasound biomicroscopy (UBM) [4]. These methods provide high resolution illustration of the human eye. OCT offers a spatial resolution of 2 - 25 µm [1, 3] while for UBM a spatial resolution of 30 - 50 µm at a depth of penetration of 4 - 5 mm is described [1, 5]. All these techniques are mainly limited by optical distortion and thereby necessary post processing, requirement of contact with the eye, which is unfavorable for the patient, and limited penetration posterior to the iris and sclera. The pigment layer of the iris represents an additional barrier to all the mentioned techniques, except UBM, and therefor a diagnostic evaluation of the dorsally located structures is impossible. Imaging the whole orbital anatomy distortion free however is key to successful clinical diagnosis. Magnetic Resonance Imaging (MRI) on the other hand offers the possibility to image the anatomy of the human eye both in anterior and posterior regions, making it a principal tool for ocular research. Due to its great soft tissue contrast and the lack of ionizing radiation exposure [6, 7] it is currently used for evaluation of the anterior and posterior chambers of the eye, for examination of the orbits and for tumor diagnostics [8]. Especially in tumor diagnostics and treatment, MRI is lately evolving to be the gold standard imaging system. In combination with US, high resolution MRI has emerged as an important imaging modality for pretreatment evaluation, for example by facilitating the detection of local tumor extent or the diagnostic confirmation [9]. MRI is also becoming increasingly important in the planning of stereotactic irradiation techniques of uveal melanoma, where contrast enhanced images are needed to determine the target volume for melanoma treatment [10, 11]. This prospective study was conducted to evaluate and improve the current ophthalmological MRI methodology and to assess the feasibility of triggered MR sequences using the medEyeTrack system.

1.2 Characterization of MR Imaging of the Eye

The eye consists of different tissues with very diverse densities. Its size and the dimension of severy small structures within the eye make it a very difficult anatomical part to image with MR imaging. In the following a brief introduction of the anatomy of the orbit and the bulb and their imaging characteristic is given.

1.2.1 Anatomy of the Orbit

The orbit is essentially a bony socket for the eyeball (bulb) containing muscles, nerves, vessels, lacrimal organs and surrounding fatty tissue. This eye socket is formed by seven bones: the frontal, sphenoid, zygomatic, ethmoid, lacrime, maxillary and palatine bones as shown in Figure 1.1. The orbit is structured in eight compartments according to anatomical structures as illustrated in Figure 1.2. Lacrimal gland, bulb, optical nerve and the muscles each represent a separate compartment. The orbital septum is a membranous sheet that divides the orbit in a pre- and a postseptale compartment. The postseptal compartment is again divided into several compartments such as the subperiostal compartment which is located between the bone and the extraconal compartment. The eye muscles separate the intraconal and the extraconal compartment from each other, whereby the intraconal compartment is filling the space between the muscles [11–13].

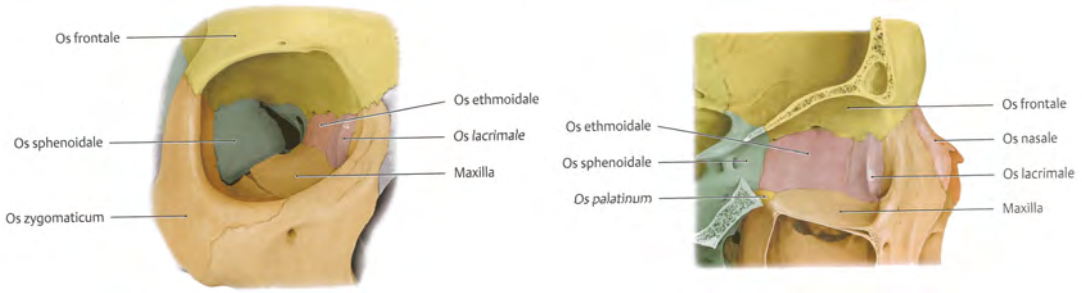

(a) frontal (b) lateral

Figure 1.1: Anatomy of the orbit. Frontal and lateral view of the orbit [12].

1.2.2 Anatomy of the Bulb

The ocular bulb is spherically shaped and about 2,4 cm in diameter (Figure 1.3). It is embedded in the bony eye socket and is surrounded by fatty tissue which is separated from the bulb by a membrane, the fascia bulbi (capsula of Ténon). This membrane envelopes the eyeball from the optic nerve to the limbus and creates a socket for the eyeball to move in. The bulb is composed of three coats. The outermost layer consists of the sclera and the cornea. The sclera is the white part of the eye and consists of connective tissue, it coates the whole bulb and gives it its form. The anterior transparent part of the sclera is

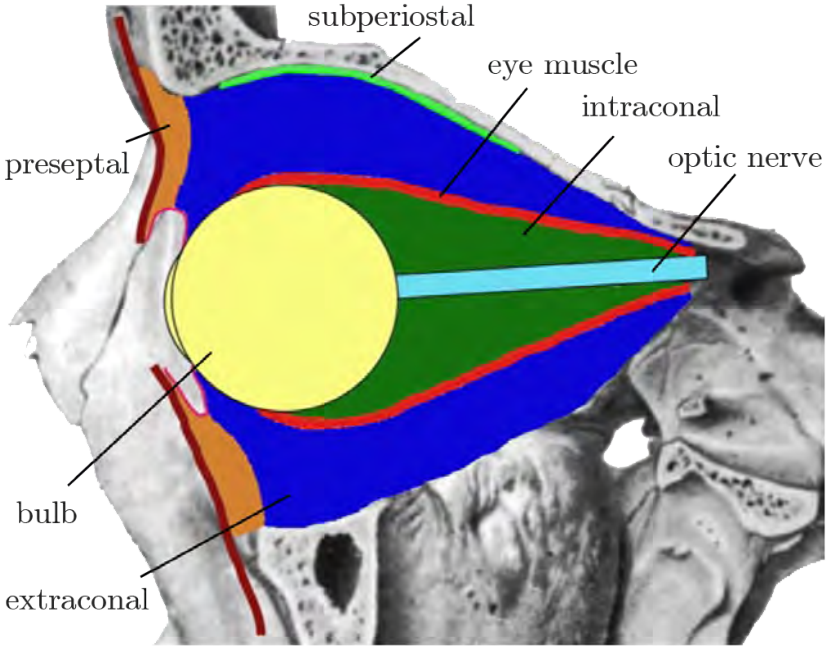

Figure 1.2: Seven of the eight compartments of the orbit. For more clearness the lacrimal gland is not included in this figure (located in the extraconal compartment) [14].

the cornea. The middle coat layer of the bulb is composed of the choroid, cilliary body and iris. These three parts together are often referred to as uvea. The innermost of the bulb layer is the retina which is the light-sensitive part of the eye. All these coats enclose the aqueous humor, the vitreous body and the lens. The lens is laterally connected to the cilliary body and divides the bulb in two departments, the anterior and posterior chamber. The anterior chamber is filled with the aqueous humor, a transparent and gelatinous fluid similar to plasma. The posterior chamber is filled with vitreous humor or vitreous body which is similar to the aqueous humor a transparent, colorless gelatinous mass. The lens is composed of three parts: the lens capsule, the lens epithelium and the lens fibers. The outermost layer is the lens capsule, the middle layer is the lens epithelium which is only located on the anterior side of the lens. The lens fibers are the inner most layer and form the bulk of the lens. Under normal pathological conditions the different layers of the bulb can hardly be distinguished by MR imaging techniques. However ablations of different layers, which can result from pathological processes, can be detected [15–17]. The most important structures in ophthalmological MRI and especially for uveal melanoma imaging are described hereafter.

Vitreous body The vitreous body is a transparent gel and lies between the lens and the retina. With approximately 4 ml it forms more than two-thirds of the ocular volume. It consists of 98% - 99% water bound to a mesh work of collagen fibrils. Further components of the vitreous body include small amounts of soluble proteins, hyaluronic acid and some

salt. In infancy the vitreous body is thick, composed of well balanced collagen network and mostly homogeneous. With age the density drops and it becomes more liquid [13,18].

Retina The retina is the thin sensory inner layer of the bulb. It is thinnest at the ora serrata (100 µm) and thickest near the optic disk margins (560 µm). Its outer surface is connected to the choroid and its inner surface is in contact with the vitreous body. It extends from the scalloped margin of the ora serrata anteriorly to the optic nerve head (see Figure 1.3). It is roughly divided into two layers: the inner photoreceptor layer also called neuroretina and the outer pigment epithelium layer [13].

Choroid The choroid is the thin mid layer of the bulb. It extends from the ora serrata to the optic nerve and is thickest beneath the fovea centralis (located close to the optic disk) (300 µm) and thinnest at the ora serrata (100 - 150 µm). The choroid is mostly a vascular layer and is supplied by the short posterior cilliary arteries. On the inside its surface is smooth and firmly attached to the pigment epithelium of the retina. Its outer surface is more rough and firmly attached to the sclera [13].

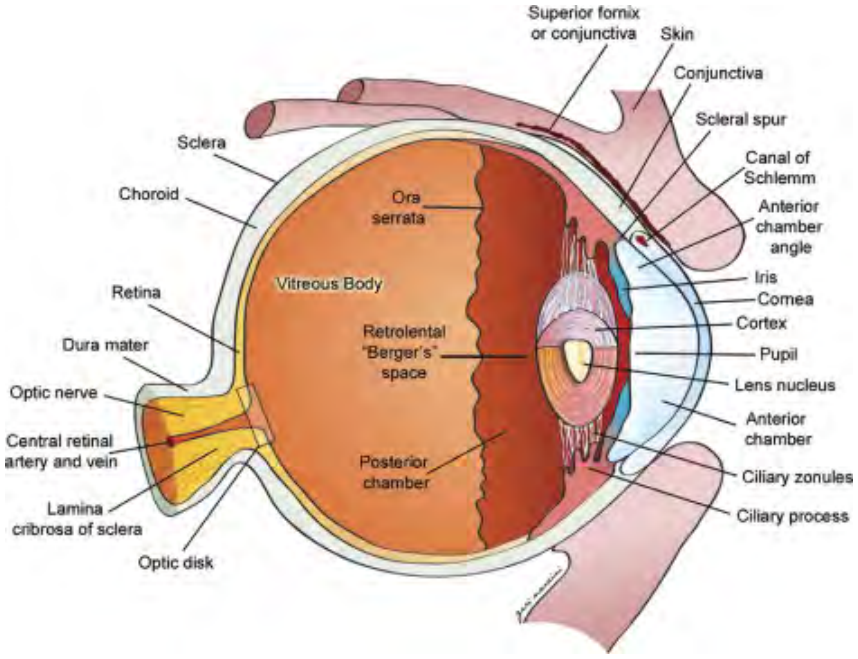

Figure 1.3: Anatomy of the ocular bulb [18].

1.2.3 Image Characteristics

Some of the eyes' structures have a very high water content, for example the aqueous humor in the anterior chamber or the vitreous humor in the posterior chamber (see Section 1.2.2). Therefore, MRI contrast can be achieved due to different water content of contrary structures, or due to differences in relaxation properties characterized by

their T_1, T_2 and T_2* relaxation times [19]. To depict the anatomical structures of the bulb normally T_1 weighted imaging is chosen. T_2 weighted images are commonly used for differential diagnostic imaging, for example to differentiate bleeding from tumor tissue [11]. Also T_2 weighted images are primarily used for pathologies [6].

T_1 weighted imaging In T_1 weighted (T_{1w}) imaging (Figure 1.4a), the following signal intensities can be observed: In the case of T_{1w} images, the aqueous and vitreous humor are expected to have a low signal, hence they appear dark. The lens appears hyperintense (gray) compared to the vitreous/aqueous humor [6]. The lens capsule has a high signal intensity, lens nucleus and lens cortex have both lower intensities compared to the capsule but are differentiable [11]. Cilliary body and iris have slightly hyperintense signals [11, 18]. The sclera shows low signal intensity compared to the inner layers of the bulb (choroid, retina) which makes the sclera easily differentiable from the inner layers. In vivo, the choroid and retina are not reliably distinguishable, both appear as hyperintense structure [6, 11]. In exams of enucleated bulbs the retina can be distinguished and has an even higher signal than the choroid [11]. The optic nerve has a similar signal intensity as the cerebral white matter (appears gray), the optic nerve sheet is slightly hypointense compared to the nerve [6].

T_2 weighted imaging In T_2 weighted imaging (Figure 1.4b), the following signal intensities can be observed: The main signal in an MR image of the eye stems from the aqueous and vitreous humor due to their high water content of >98%. Hence aqueous and vitreous humor show hyperintense signals on T_2 weighted images. The lens appears hypointense and is therefore good distinguishable from the aqueous and vitreous humor. Cilliar body and iris show hypointense signals [8, 18] and thus may be obscured by the very high T_2 signal intensity of aqueous and vitreous humor [18]. In T_2 weighted images the sclera shows the same hypointense signal as the cornea. Compared to the vitreous humor the nervus opticus shows a slightly hypointense signal. The highly vascular choroid layer shows a hyperintense signal contrary to the retina with its hypointense signal. In vivo, the different layers of the bulb are not reliably distinguishable, but MR microscopy is able to produce high resolution images that make a differentiation in 3 layers feasible. Langer et al. even showed a differentiation between the two main layers of the retina [8].

1.2.4 Artifacts in Ophthalmological MRI

Like other imaging modalities, MRI is vulnerable to image artifacts. Artifacts occur when one or more assumptions, on which the imaging principle or reconstruction algorithm depend, are violated. Often more than one artifact is present in one image. In MRI it is hard to definition an artifact. This is partly because of the vast variety of occurring phenomena and partly due to the fact that some of the so-called artifacts are obstructive

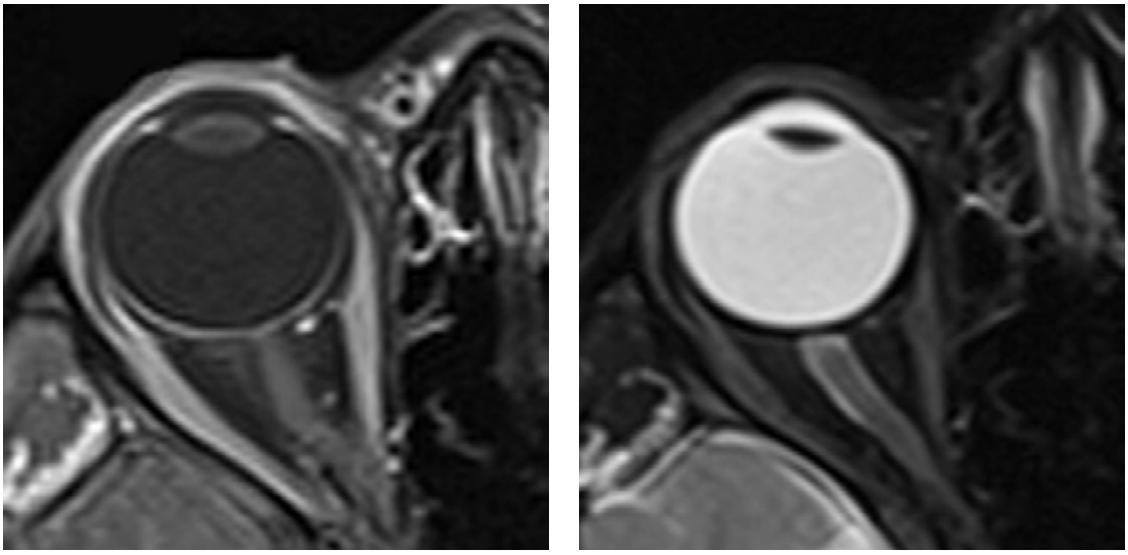

(a) T_1 weighted (b) T_2 weighted

Figure 1.4: Anatomy of the orbit in a T_1 (a) and T_2 (b) weighted image showing the different structures of the eye [18].

in one modality while representing a feature in another. For example the variations of susceptibility or magnetizability of materials lead to blurring, displacement and signal loss in one application but this same effect is the foundation of functional MRI. In general, we can define an artifact as any image content that does not correspond to the dimension of the imaged object or to random noise. Common sources of artifacts can be divided in four groups as seen in Table 1.1 [20]. The most important artifact sources in ophthalmological MRI are discussed below.

Motion and flow Classic MRI sequences are relatively time-consuming, their duration can range from seconds up to minutes. Standard image reconstruction techniques assume a perfectly stationary object/patient. Due to motion introduced by physiological processes and voluntary or involuntary patient movement during long scan durations, this is rarely the case and makes MRI sequences very vulnerable for any kind of motion during the scan time. There are two kinds of motion, random motion such as patient movement, peristalsis, swallowing and eye movement and periodic motion such as the pulsatile flow of the vascular system and the cerebrospinal fluid and normal activities of the cardiac and respiratory cycles. Theoretically there are two ways of motion effecting the outcome of an image, depending on when the motion occurs in the scan process. It can take place during the data acquisition interval effecting the frequency encoded sampling, or between data acquisition intervals effecting the phase encoding direction [20]. In practice, motion artifacts tend to appear in the phase encoding direction as ghost images or diffuse image noise (blurring). The reason for this behavior is that frequency encoded sampling takes place during a single echo, which is in the range of milliseconds, and which is

Resonant offset	Main field inhomogeneity Magnetic susceptibility Chemical shift
Motion and flow	Respiration Cardiac cycle Blood and cerebrospinal fluid flow Peristalsis and swallowing Voluntary patient motion
Hardware limitations	Gradient nonlinearities Concomitant gradients Timing errors radio frequency (RF) field non uniformity Limited dynamic range
Miscellaneous	Prescription: aliasing, slice overlap, magic angle RF interference Truncation

Table 1.1: Sources of MRI artifacts [20].

thereby normally too fast to be affected by motion. Phase encoded sampling though takes up to minutes due to collection of all k-space lines and is thereby mostly affected by physical movements which are in the range of milliseconds to seconds of duration. Periodic movements mainly cause ghost images, their intensity increases with the signal intensity of the moving tissue and the amplitude of the movement. Non-periodic movements cause diffuse image noise. Both cases produce blurring, loss of resolution and a lower signal to noise ration (SNR) in the image [21, 22]. For MR imaging in ophthalmology the main eye movements besides voluntary movements are drifts, tremors, involuntary saccades and blinking [19] (see 1.3.1).

Magnetic Susceptibility Every tissue and structure is, to a certain point, prone to the magnetic field and hence is magnetizable itself. The characteristic of a material to become temporarily magnetized, when it is placed in a large magnetic field, is called magnetic susceptibility. Bone, like air, has a very low susceptibility, most tissues in the human body have mid-range susceptibility while molecules containing iron such as hemoglobin in blood have the highest tendency to become temporarily magnetized. Differences in magnetic susceptibility of adjacent tissues or media will alter the resonant frequency at a specific position. This frequency alteration typically occurs along air-tissue interfaces, around metallic bodies or near surgical implants or clips. Since the Fourier reconstruction assumes a linear relationship between frequency and spatial position any phenomena that disturbs this relationship will generate artifacts [20, 21, 23].

Partial volume effect Partial volume effects occur mostly in border regions between different tissues or if structures are smaller than the spatial resolution. If one voxel includes

parts of different tissues and structures, the signal intensities in that voxel are averaged and not handled separately. Hence, an intermediate signal is produced and information about the underlying tissue or structure is lost. This is of major relevance in application of MRI in opthalmology due to the very small structures of the eye [23].

1.3 State of the Art in Ophthalmological MR Imaging and Current Methodology

1.3.1 MR Imaging of the Orbit

In the past couple of years many new MRI techniques have been developed and ophthalmology has greatly benefited from applying these techniques. MRI has provided physiological and structural information for clinical diagnosis and treatment in ophthalmology [7, 24] and has become the method of choice in imaging ocular and orbital pathology and anatomy due to its great soft tissue contrast and the lack of ionizing radiation exposure [6, 7]. Orbital surface coils, MR contrast agents, fat suppression techniques and fast pulse sequences allow this noninvasive modality to be superior to other ocular imaging devices [6, 7, 24]. Ocular imaging should always be adapted to the problems of each individual patient. However, there are some general recommendations for orbital and ocular lesion imaging by Mafee et al. [25].

T_1 and T_2 weighted images using spin echo (SE) or fast spin echo (TSE) sequences should be used [7, 25, 26]. Mafee et al. [25] suggest that T_2 weighted TSE sequences can be imaged with or without fat saturation although a recent study by de Graaf et al. discourages from doing so because of SNR loss [9]. Also for ocular lesions precontrast and postcontrast T_1 weighted images are suggested [7, 25, 26]. These suggestions have found broad use in many orbital and ocular lesion imaging publications over the past years [18, 27–34]. Recent studies have shown that normal spin echo techniques have limited ability to detect calcification [34,35]. High resolution 3D T_2 weighted TSE showed some promising results [32, 35] but an even more effective sequence to detect calcification seems to be T_2 weighted gradient echo imaging [35]. Therefore gradient echo T_2 weighted imaging such as 3D steady state free precession sequences may replace T_2 weighted spin echo applications in the future [9]. Additionally to the already suggested sequences, short tau inversion recovery (STIR) that can detect optic nerve infiltration, may be used [36]. Several present studies have also demonstrated the use of new promising sequences for ocular imaging of various applications including 3D fast low angle shot (FLASH) [37, 38], balanced steady state free precession (bSSFP) [39], TSE sequence with variable flip angle (SPACE) [40], 3D spoiled gradient fast field echo (3D FFE) [41] and inversion recovery turbo field echo (3D IR-TFE) [41].

A crucial part of effective orbital MRI is the choice of an appropriate coil. Though

it may be the most convenient and practical approach to use the head coil it should only be used in justified exceptions, for example when imaging both the orbits and the optic chiasm is of importance [7]. For the required resolution the head coil usually gives insufficient signal to noise (SNR) values, therefore scanning (at least for 1,5 T) should always be performed with small surface coils. Studies by Lemke et al. have shown an increase in diagnostic accuracy by using such coils [28, 34]. With 3 T a main advantage is the increase in achievable SNR, and the subsequent higher resolution images compared to 1,5 T [9]. A prospective study by Erb-Eigner et al. concluded that the influence of the used small loop surface coils (diameter 4 cm and 7 cm) on SNR and image quality in ocular MRI is higher than the influence of magnetic field strength [40]. In both, a phantom and a patient experiment, the use of surface coils led to a higher SNR at both field strengths (1,5 T and 3 T). The same study also demonstrated that the head coil at 3 T does not reach the SNR values of small surface coils at 1,5 T. Therefore the usage of small surface coils is always recommended. Depending on the imaging problem several surface coil types with different diameters exist. For example for bulb diagnostic, microscopy coils with a diameter from 4 to 6 cm are usable. Surface coils with a diameter of 8 to 10 cm, which are usually used to image the whole orbit at one side, and coils with a diameter of 12 cm to display the orbits and the optic chiasm [26] are also available. Several of these coil types have been intensively used in orbital and ocular lesion imaging publications, throughout all field strengths, over the past years [28, 30, 32, 34, 38, 40–44].

The majority of artifacts in orbital MRI arise from voluntary and involuntary movements of the eyes. The main eye movements, besides voluntary movements and blinking, are drifts, tremors and involuntary saccades. Due to the very small maximum spatial displacement of these movements they normally do not lead to identifiable artifacts. The major source of artifacts are voluntary movements and blinking [19]. Bert et al. tested several approaches to minimize motion artifacts due to eye movement. Subjects fixated the non-imaged eye on a target and images where acquired with the imaged eye open, held closed, taped closed and taped closed with overlying water-soaked gauze. It was found that the setting with the eye taped closed with water-soaked gauze produced the best images and images obtained with the eye held closed by the subject showed the highest amount of artifacts [45]. Berkowitz et al. demonstrated a new approach to prevent blinking artifacts by introducing a special cyclic blink protocol where subjects were asked to withhold blinking during a 12 s imaging period and blink to their need in a 3 s rest period.

1.3.2 Current Methods at the University Hospital Graz

1.3.2.1 Planning Stereotactic Radiotherapy of Uveal Melanoma

Complete immobilization of the eye is a very important part for successful radiosurgical treatment of uveal melanoma. In order to prevent eye movement, a retrobulbar anesthetic

block in combination with subsequent fixations of the four rectus muscles with sutures (Figure 1.5a) to the stereotactic frame mounted to the head (Figure 1.5b) is used. This procedure is necessary to guarantee a constant and controlled eye position throughout the whole treatment [46]. The stereotactic frame provides the coordinate system for the computer tomograph (CT) and the linear accelerator (LINAC). Four pins are used to anchor the frame to the patient's head, the pins are hand-screwed into the outer shell of the skull under local anesthesia [47]. The imaging protocol includes CT and MRI scans. The MRI scan normally takes place a day before the stereotactic radiotherapy. The CT scan is performed subsequently to the attachment of the stereotactic frame to the patient's head and immobilization of the eye. In MR imaging the tumor boarders are depicted much sharper, much like in B echo scans, compared to the CT [46]. Therefore it is the primary imaging technique for treatment planning. CT imaging is still needed for providing the coordinate system. At the moment MR and CT images are fused for treatment planning to maximize the superposition of both image types in order to ensure a maximum accuracy for tumor selection. After data fusion, the tumor region is identified by hand and a 1 mm safety margin is added to create the planning target volume (PTV). For treatment planning a conformation technique is used [48].

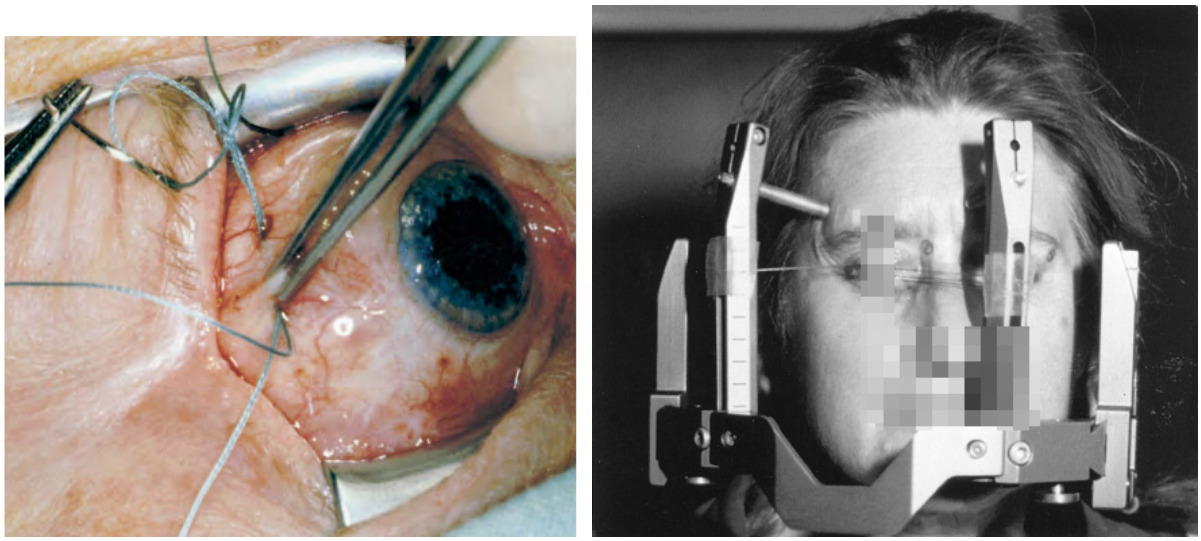

(a) (b)

Figure 1.5: Photograph showing the suture insertion into a rectus musculus (a). Photograph showing a mounted stereotactic frame with sutures attached similar to the one used at the University Hospital Graz (b) [46].

1.3.2.2 MR Imaging

Currently a T_1 weighted gadolinium-enhanced MR protocol is used to image the eye pre- and post-contrast on a Siemens MAGNETOM Verio 3 T using a Siemens 32 channel head coil. The contrast enhanced imaging allows the delimitation of subretinal fluid from the

tumor [46]. A 3D FLASH sequence is employed to depict the whole head in order to be able to fuse the MR data with the CT data. A matrix of 256 x 256 pixel is used with a FOV of 230 mm and a slice thickness of 1 mm which leads to a voxel size of 0.89 x 0.89 x 1 mm. Echo time (TE) and repetition time (TR) are chosen to be 3.56 ms and 7.31 ms, respectively. The flip angle is 10°, averaging is set to one, the bandwidth is 219 Hz/pixel and acquisition time is 3:31 min.

1.3.2.3 MR Artifact Prevention

To prevent artifacts currently the patients are told to close and hold their eyes still as good as possible during the entire acquisition time.

1.4 Aim of this Study

MRI has become the method of choice in imaging ocular and orbital pathology and anatomy due to the lack of ionizing radiation exposure and its great soft tissue contrast [6, 7]. With the usage of small surface coils and the choice of the appropriate MRI sequences MR imaging can provide the needed physiological and structural information for clinical treatment and diagnosis in ophthalmology [7, 24]. At the University Hospital Graz for example, MRI is used together with CT for planning of radiotherapy in ophthalmological tumors. Especially, for stereotactic radiotherapy planning for uveal melanoma treatment it is crucial to have artifact free images with the highest possible resolution while still maintaining optimal contrast and signal to noise values. Apart from simplifying the planning procedure, optimal MR images also highly advance the treatment outcome.

The aim of this prospective study was to first of all incorporate a recently developed eye tracking solution (medEyeTrack), as part of a cooperation between Medical University of Graz (Department of Therapeutic Radiology and Oncology), Graz University of Technology (Institute for Computer Graphics and Vision) and M&R Automation GmbH [49], into the existing MR protocol. Second, the existing MR protocol needed to be expanded with applicable new MRI sequences for interaction with the medEyeTrack (triggerable) and optimized for the use in ophthalmology in general. Furthermore, this study elucidates the influence and practicability of a small surface coil in the application of ophthalmological MR imaging. Lastly, this work should clarify the feasibility of a triggered MR sequence to avoid motion artifacts due to voluntary eye movement in high resolution MR imaging of the orbit.

Chapter 2

Sequence Theory

2.1 Turbo Spin Echo (TSE)

2.1.1 TSE Introduction

For this kind of MR sequence many names have arisen over time, including Turbo Spin Echo (TSE), Fast Spin Echo (FSE), Fast Acquisition Interleaved Spin Echo (FAISE), Rapid Acquisition with Relaxation Enhancement (RARE). In a general sense, for all these sequences, TSE will be used in this thesis. TSE is a fast turbo spin echo sequence that applies an RF excitation pulse followed by several RF refocusing pulses to produce multiple spin echoes, a so called echo train [50, 51]. Contrary to a conventional spin echo sequence (SE) every echo in this echo train is distinctively phase encoded in order to fill multiple k-space lines after every RF excitation pulse (see Figure 2.1 for a principle explanation). Unlike for the SE sequence, with this method numerous k-space lines can be acquired during one single TR period. This reduces the total scan time substantially. Considering a single sliced 2D scan with 16 distinctively phase encoded echoes, compared to a conventional SE sequence with otherwise same scan parameters the total scan time can be reduced by the factor 16. Not only its primary advantage, the reduction in scan time, but also its excellent image quality makes TSE a valuable and largely accepted tool in clinical diagnosis. In fact, especially for T_2 weighted imaging it has replaced the conventional SE sequences. Known downsides of TSE sequences include ghosting, blurring, edge enhancement, RF power deposition and altered image contrast caused by magnetization transfer effects and hyperintense lipid signal [52].

2.1.2 TSE Sequence

A 2D TSE sequence starts with a 90° RF excitation pulse followed by a 180° refocusing pulse after a time τ. This leads to an echo at the time 2τ. After acquisition of this echo, another 180° refocusing pulse pancake-flips the dephased magnetization vectors around the

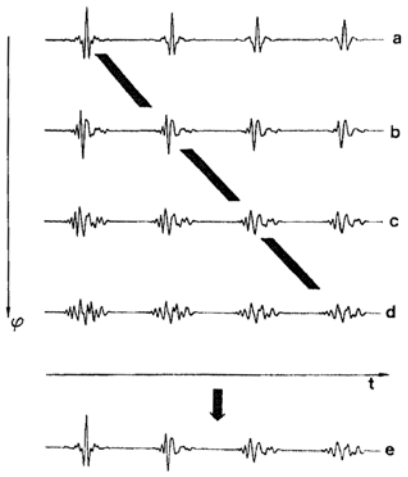

Figure 2.1: Echo imaging principle. Every echotrain (a-d) is distinctively phase encoded. In TSE imaging only one echo train is sampled and every single echo of the echotrain is phase encoded separately (e) [50].

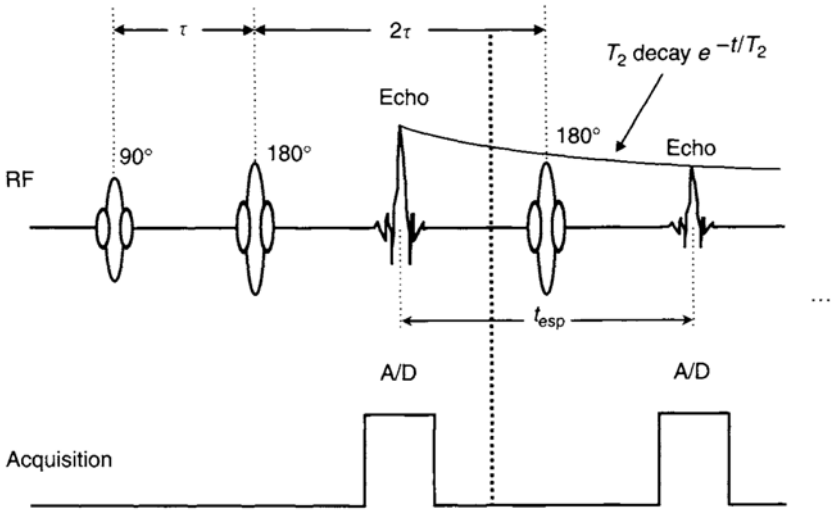

Figure 2.2: Sequence diagram for comparison of conventional SE sequence (stops at dotted vertical line) and TSE sequence [52].

axis of the pulse, at timepoint 3τ and leads to another echo at 4τ (depicted in Figure 2.2). If the second echo is distinctively phase encoded it can be used to sample a second line in the k-space. Typically, the distance between the RF refocusing pulses is double the time delay τ between the excitation pulse and the first refocusing pulse [52]. The echo train can be elongated by additional 180° refocusing pulses as long as substantial decay of the transverse magnetization by T_2 does not take place. The formed echo train after one single 90° RF excitation pulse hence can sample multiple k-space lines and therefore shorten the acquisition time. The total number of produced echoes is called the echo train length (ETL or N_{etl}). Provided that all echoes are distinctively phase encoded then N_{etl} is the same as the number of refocusing pulses and the number of k-space lines acquired per TR. In TSE sequences ETL is a very important parameter. It equals the scantime reduction factor compared to a conventional SE sequence. Longer ETL means shorter scan time. In practice there are two limiting factors for ETL, the time interval between two back-to-back echoes, also called the echo spacing (ESP or t_{esp}), and the tissue T_2 relaxation time [52]. The scan time can be calculated with Equation 2.1 (single-slice acquisition assumed) where N_{shot} is the number of shots, NEX is the number of excitations or number of averages, N_{phase} is the number of phase encoding steps, int takes only the integer part of its argument and modulo (mod) gives the remainder of a integer devision [52].

$$T_{scan} = TR * N_{shot} * NEX \tag{2.1}$$

with

$$N_{shot} = \begin{cases} N_{phase}/N_{etl} & if(N_{phase}\ mod\ N_{etl}) = 0 \\ int(N_{phase}/N_{etl}) + 1 & if(N_{phase}\ mod\ N_{etl}) \neq 0 \end{cases} \tag{2.2}$$

To achieve more robustness regarding the RF magnetic field (B1-field) inhomogeneity, the phases of the refocusing pulses are shifted by 90° compared to the excitation pulse [53]. Figure 2.3 depicts that simultaneously with each of the RF pulses a slice selection gradient is applied. Additional a slice-rephasing gradient is needed after every excitation pulse. Combined with this gradient a so called "crusher" is applied in order to zero the unwanted signals and enable the desired. Frequency encoding is achieved by identical readout gradient lobes. To center the window a prephasing gradient is applied between the first refocusing and the excitation pulse. Phase encoding is accomplished with a gradient applied between each refocusing pulse and the readout gradient. To ensure the signal coherence, a phase rewinding gradient goes along with the phase encoding gradient [52].

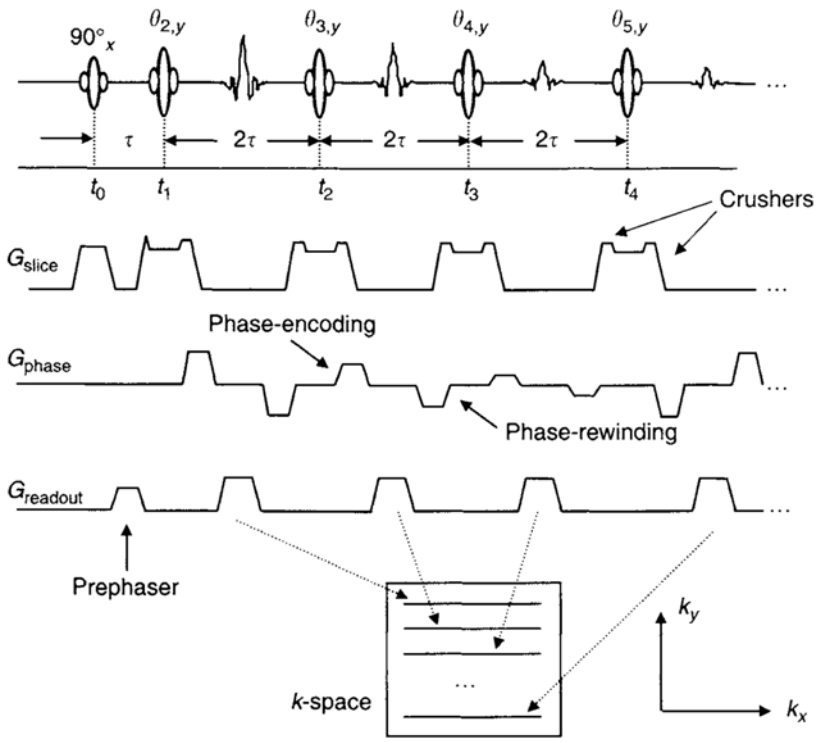

Figure 2.3: Sequence diagram of a 2D TSE sequence. The $90°_x$ is the RF excitation pulse. $\theta_{2,y}$, $\theta_{3,y}$, $\theta_{4,y}$ and $\theta_{5,y}$ depict the refocusing pulses. The axis along which the RF puls is applied is specified with the subscript x or y [52].

2.1.3 TSE Contrast

The echo amplitude decays according to Equation 2.3 (assuming refocusing pulses are 180°) where n is the echo index that lies between 1 and N_{etl} [52].

$$S(n) = S_0 \, e^{-n \, t_{esp}/T2} \tag{2.3}$$

Each individually encoded echo in the echo train has its own specific TE value which is calculated using Equation 2.4.

$$TE = n \, t_{esp} \tag{2.4}$$

This fact leads to a k-space that is non-uniformly T_2 weighted. Generally the image contrast is mostly dependent on the low frequencies in the k-space center [54,55], therefore the effective TE (TE_{eff}) for a TSE sequence is defined as the time when the central k-space line is acquired. In order to achieve a T_2 weighted image, one of the later echoes in the echo train is used for the center k-space line and the other echoes are used to fill the remaining k-space. To influence the degree of T_2 weighting different echoes can be assigned to the center k-space line (see Figure 2.4). Strongly T_2 weighted images therefore require a very long ETL. Note that TE_{eff} can only be a multiple of t_{esp} and is limited by N_{etl} * t_{esp}.

For T_1 weighted images a very early echo in the echo train is used (i.e. $TE_{eff} = t_{esp}$) to sample the center k-space line, all the subsequent echoes are used to sample the remaining k-space [52].

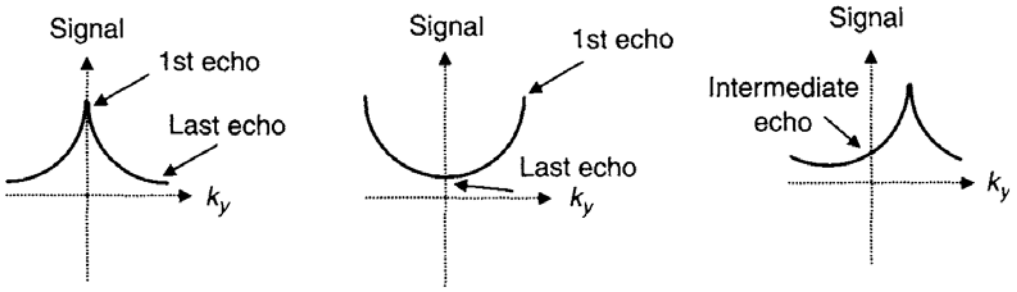

(a) T_1 weighted (b) heavily T_2 weighted (c) moderatly T_2 weighted

Figure 2.4: TSE sampling schemes. Different echoes are assigned to the center k-space line. For all three cases two shots are assumed [52].

2.1.4 TSE Image Artifacts

There are three major artifacts that can arise with TSE sequences: blurring, edge enhancement and ghosting.

Blurring The nonuniform T_2 weighting of the image described by Equation 2.3 introduces a weighting function $W(k_y)$ (also called T_2 weighting function) in phase encoding direction. For a specific tissue the weighting function can be described with Equation 2.5 where n is a function of the k-space line index in phase encoding direction [52].

$$W(k_y) = e^{-n(k_y)\, t_{esp}/T_2} \tag{2.5}$$

Taking the T_2 weighting function into account the TSE k-space data can be described with Equation 2.6.

$$S(k_x, k_y) = S0(k_x, k_y) * W(k_y) \tag{2.6}$$

This Equation shows that the image obtained by applying the Fourier transform on $S(k_x,k_y)$ is the convolution of the ideal image with the T_2 weighting function. The weighting function is a Lorentzian-like function and leads to blurring of the image. With conventional SE sequences this blurring does not take place because $W(k_y) = 1$. Tissues with short T_2 lead to more blurring in the resulting image than tissues with long T_2. There are several approaches to minimize such blurring artifacts including deconvolution with

a previously acquired T_2 map, deconvolution with an average T_2 value along the phase encoding direction and blur reduction with signal averaging (NEX $\geq$ 2) [52].

Edge Enhancement For T_2 weighted TSE images the early echoes are used for filling the borders of the k-space. In the boarder regions of the k-space high frequency is predominant. Therefore the T_2 weighting function induces a high pass filtering of the k-space data in phase encoding direction. This results in an enhancement of the edges in phase encoding direction of the image. The artifact can be reduced with the same methods used for blur reduction [52].

Ghosting This is another common artifact along the phase encoding direction in TSE imaging. In k-space data, phase errors are almost always present. Consistent phase errors across the whole k-space do not produce any ghosting artifact (conventional SE imaging). Ghosting is only introduced if the phase error is changing over the course of the phase encoding direction. This is the case with TSE imaging. Low frequency ghosts are generated by high-frequency phase variation in the k-space and vice versa [52].

2.1.5 Specific Absorption Rate (SAR)

The specific absorption rate is defined by Equation 2.7 where E is the total RF energy, t_{exp} is the exposure time and M is the unit mass in kilograms.

$$SAR = \frac{E}{t_{exp}\, M} \tag{2.7}$$

Due to the fact that in TSE imaging multiple RF refocusing pulses, with high flip angles, are applied in a very short time SAR can be very high. SAR increases as the square of the field strength as well as the square of the flip angle [21], meaning it is of particular importance with field strengths of 3 T and higher [52]. To exploit the full time reduction potential of the TSE sequence without exceeding SAR limits, several methods have been developed for reducing SAR [52]. Reducing the flip angle ($<180°$) is an effective way to decrease SAR because SAR is proportional to $(B_1)^2$ [56–58]. Using hyperechoes is another approach to reduce SAR. Here a refocusing pulse train is applied which has a 180° refocusing pulse in the middle and refocusing pulses with lower flip angles are mirrored symmetrically around it. These RF pulses are typically between 60° and 130° [51, 52]. Usually the so called hyperecho (flip angle = 180°) is used to sample the center k-space line. This method reduces SAR considerably without affecting the Signal to Noise Ratio (SNR) [58].

2.2 SPACE

2.2.1 SPACE Introduction

The fact that spin echo based sequences are resistant to artifacts from the main magnetic field (B_0) and RF inhomogeneities and that they offer a variety of image contrasts, make them particularly desirable and widely used in clinical MRI [59,60]. Especially, TSE pulse sequences (described in 2.1) are of great interest because they combine the desired behavior of spin echo sequences with a considerable speed advantage [59]. However as described in section 2.1.5 SAR can severely limit the usage of TSE sequences in multi slice or 3D imaging [60]. 3D imaging has several advantages in characterization and evaluation of complex anatomy and pathology [59, 60] but usually is very time consuming, especially for T_2-weighted applications, and therefore not widely used in clinical MRI [60]. Speed increase by lengthening the echo train is limited by T_2 decay which will induce several known artifacts, described in section 2.1.4. In order to enable fast spin echo based 3D imaging, MR-equipment manufacturers have introduced optimized 3D TSE sequences over the past few years, with a variety of different sequence names. Examples of such sequences are Volumetric Isotropic TSE Acquisition (VISTA; Philips Healthcare), CUBE (GE Healthcare) and Sampling Perfection with Application optimized Contrasts by using different flip angle Evolutions (SPACE, Siemens Healthcare). In a general sense, for all these sequences, SPACE will be used in this publication.

2.2.2 SPACE Sequence

To make 3D single-slab TSE imaging practical for clinical use, time efficiency has to be increased considerably. In order to achieve this goal, several adjustment to existing TSE sequences had to be made including considerably lengthening the usable duration of the echo train by using variable flip angle refocusing RF pulses [61, 62] and shortening the echo spacing [63–65].

Shorter Echo Spacing For imaging only a single slab, spatial selection of the RF pulse is not required and thus can be replaced by a short, rectangular and non spatially selective RF pulse to minimize the pulse duration [63–65]. If the data sampling period is in the range of a few milliseconds (bandwidth is moderate to high), the replacement of a conventional spatial selective RF pulse with a very short non spatial selective RF pulse ($<$1 ms) offers a substantial cutback in echo spacing. This enables the sampling of an increased number of echoes after each excitation pulse for a given echo train length [63].

Longer Echo Trains For typical TSE pulse sequences, as described in section 2.1, the ETL is limited by T_2 relaxation times. For clinical use the echo train duration

is typically less than two to three times the T_2 value of the tissue of primary interest for long TE_{eff} (T_2 weighted). For short TE_{eff} (T_1 or proton-density weighted) echo train duration is normally shorter than the T_2 value of the tissue of primary interest [63]. Using longer echo trains leads to well known artifacts described in section 2.1.4. For biological tissues, where T_1 values normally exceed T_2 by a large amount, constant low flip angles that are lower than 180° can be used to introduce T_1 dependence to the evolution of the echo train to elongate it [66]. In the case of refocusing flip angles lower than 180° the transversal magnetization is not fully pancake-flipped in the transversal plane. It is partially left intact, partially tipped onto the longitudinal axis (either +z or -z) and only partially refocused in the transversal plane. With further low refocusing flip angles also the longitudinal magnetization is partially left alone, partially inverted and partially excited to the transverse plane to form a stimulated echo. With the subsequent low refocusing pulses (<180°) any of these magnetization components is further divided [52]. Such a phase evolution can be depicted by a phase diagram which was introduced by Henning in 1988 [66]. An example of such a phase diagram can be seen in Figure 2.5. After a refocusing pulse transversal magnetization is going to accumulate phase until it eventually forms a spin echo and is affected by the next RF pulse. On the contrary, the longitudinal magnetization remains constant unless an adjacent RF refocusing pulse excites it to the transverse plane [52]. One remarkable character of the formation of stimulated echoes is that, while the magnetization is in the longitudinal plane it experiences T_1 decay. Compared to a normal spin echo, which is determined exclusively by T_2, T_1 significantly impacts the amplitude of the stimulated echo. This is particularly striking in biological tissue where T_1 is several times longer than T_2. Thus the time between the excitation and the forming of an echo can be much longer with stimulated echoes compared to conventional spin echoes. Hence, stimulated echoes are from major importance in greatly extending the usable echo train length of a TSE sequence [59]. Examples for using low flip angles for RF refocusing pulses can be found in Figure 2.6. Figure 2.6a and 2.6b show a constant flip angle of 180° and 60°, respectively. The corresponding signal evolutions throughout the echo train can be seen in the middle column. It can be seen that the signal for 60° constant flip angle starts to exceed the signal from 180° for echo times greater than approximately 200 ms. This can be explained by the fact that both spin echoes and stimulated echoes contribute to the overall signal for the 60° RF refocusing pulse. The T_1 time for the tissue in this example is around 10 times larger than the T_2 time and therefore enables stimulated echoes to intensively contribute to the very late echoes in the echo train. The right column in Figure 2.6 depicts two quantities that are useful for evaluating the performance of the refocusing RF pulse. The dashed lines show the fraction of magnetization in the longitudinal plane. As mentioned above this is the fraction of magnetization that is "stored" along the z-axis and generates stimulated echoes. Throughout the echo train the dashed line for the 180° refocusing RF pulse is zero, because

all of the magnetization is refocused in the transversal plane. For the 60° refocusing RF pulse on the other hand, as expected, the stored fraction of the magnetization is significantly higher. This stored magnetization decays with T_1 and is responsible for higher amplitudes at very late echo times. The solid lines are depicting the fraction of magnetization in the transverse plane that generates the signal. This indicates how effective the transverse magnetization is used to generate signal. It can be seen that the transversal magnetization is used much more effectively by the 180° than by the 60° refocusing RF pulse. Especially with early echo times the transverse magnetization fraction is used very poorly and never reaches 1 at late echo times. Despite the effect that the signal in later echo times is higher than with 180°, the 60° constant flip angle approach has still room for improvement, especially regarding the efficiency of transversal magnetization usage [59]. To improve usage of transversal magnetization Alsop et al. [56] described an approach that ramps down the flip angle from a fairly high value at the beginning of the echo train to a constant value that is used throughout the majority of the echo train. Such a flip angle scheme can be seen in Figure 2.6c. Compared to Figure 2.6b the overall signal evolution could be improved and the signal intensities for long echo times are even higher. Also the very right column of Figure 2.6c depicts a much better use of the transversal magnetization [59]. A variation of the flip angle throughout the entire echo train can even further improve the signal evolution as can be seen in Figure 2.6d. Particularly for echoes in the center region of the echo train a massive increase in signal intensity can be observed compared to the constant 180° refocusing RF pulse. At 400 ms (center echo) a 10 fold increase in signal intensity compared to the constant 180° refocusing RF pulse can be denoted. The third column of Figure 2.6d offers valuable information of how such high signal intensities can be achieved with a variable flip angle scheme. In early echo times a large fraction of the magnetization is stored along the longitudinal axis (dashed line) and as the echo train advances this magnetization is gradually converted into the transversal plane. Therefore it is possible to maintain relatively high signal amplitudes throughout the echo train, especially in the mid section. The solid line indicates that this sequence also makes very good use of the transversal magnetization, the fraction stays at 1 for almost the entire length of the echo train [59].

2.2.3 SPACE Contrast

Contrast behavior of the SPACE sequence compared to conventional TSE sequences is strongly dependent on the flip angle scheme used for refocusing RF pulses. Flip angle schemes currently used for SPACE imaging can be divided into three main categories: (1) relatively high, constant flip angles, (2) variable flip angle scheme or initial flip angle ramp down with subsequent low, constant flip angles with short to moderate TE_{eff}, and (3) variable flip angle scheme or initial flip angle ramp down with subsequent low, constant

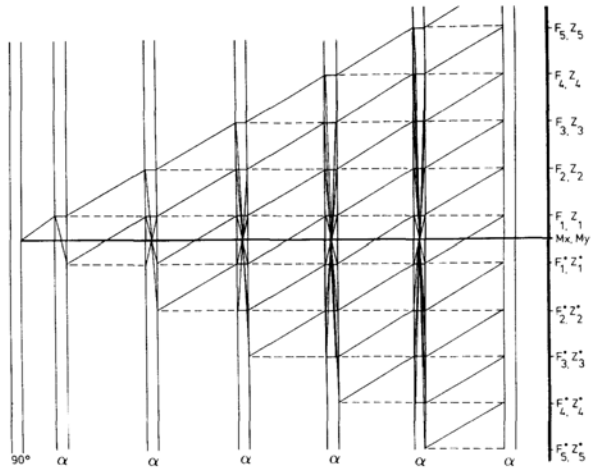

Figure 2.5: Extended phase diagram by Henning 1988 representing the spin evolution of a TSE sequence with arbitrary flip angle α. The labeling on the side are different spin states. The solid lines are connecting the different states of the spin system right after and right before a pulse. Dashed lines represent the evolution of the z coherences. An echo is produced between the pulses whenever a solid lined crosses the horizontal M_x, M_y line [66].

flip angles with long TE_{eff}. The contrast behavior for category 1 is essentially the same as for conventional TSE sequences using the same flip angle [59]. For category 2 and 3 the contrast behavior may be significantly different compared to constant 180° refocusing RF pulses [62] and depends on TE_{eff} as well as on the flip angles prior to TE_{eff} [51, 67]. The signal at TE_{eff} is composed of both stimulated echoes and spin echoes. The magnetization leading to a stimulated echo is stored in the longitudinal plane and decaying with T_1. Thus the time this magnetization spends in the transverse plane decaying with T_2 is reduced, resulting in a decreased T_2 contribution to the signal at TE_{eff} compared to constant 180° refocusing RF pulses, and the echo time reflecting the contrast of the corresponding image is shorter than TE_{eff} [59]. However, there is a way to calculate the influence of stimulated echoes on the image contrast. Also an echo time which reflects the contrast of the image, the so called "contrast-equivalent" TE, can be determined [51, 67]. The flip angle scheme has almost no influence on the contrast for short TE_{eff} (category 2). Thus, the contrast-equivalent TE and the actual TE_{eff} are very similar in this case [59]. On the other hand, for long TE_{eff} (category 3) the flip angle scheme has a major influence due to the fact that late echoes in the echo train are used to sample the center k-space line. Therefore the calculated contrast-equivalent TE and the actual TE_{eff} may differ substantially [59]. Summed up for SPACE imaging the contrast-equivalent TE and the actual TE_{eff} may be quite different and some authors and manufacturers do use these terms interchangeably which may lead to confusion. It is particularly important to emphasize that these are two different parameters and both are very important to describe the contrast behavior of a SPACE sequence [59]. TE_{eff} is the echo time corresponding to the center of k-space and

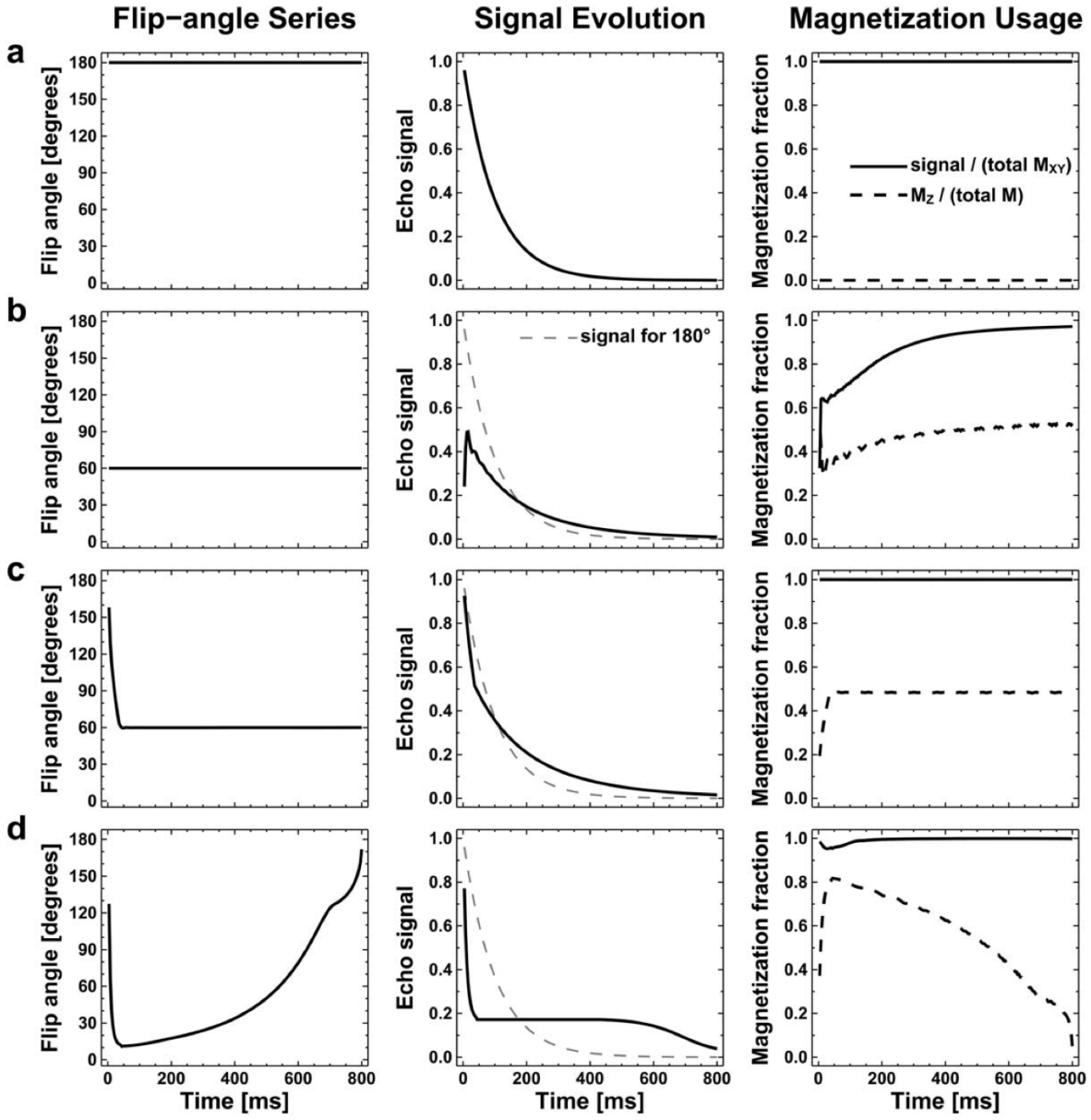

Figure 2.6: Variable flip angle schemes to elongate the echo train duration. Four different flip angle schemes for refocusing RF pulses (left column) over an 800 ms echo train length with the according echo signal amplitude evolution (middle column) and fraction of transverse magnetization, which generates signal (solid line) and the fraction of longitudinal magnetization which stores magnetization (dashed line), (right column) are depicted. Echo train length = 200, echo spacing = 4 ms, $T_1 = 100$ ms, $T_2 = 100$ ms, TR relative long to T_1 , M magnetization, M_{XY} transversal magnetization, M_Z longitudinal magnetization [59].

the contrast-equivalent TE is a calculated value to compare the contrast of a 3D TSE sequence with variable RF refocusing pulses to a conventional 2D TSE sequence with constant 180° refocusing RF pulses.

2.2.4 SPACE Image Artifacts

Signal Evolutions for Variable Flip Angles In Figure 2.6 it is shown that it is possible to use variable flip angle schemes to hold the signal level constant for a significant amount of the echo train length. However, this signal evolution is specific for one tissue and relaxation time dependent. Therefore it may look in some way different for other tissues with deviant relaxation times. Across a range of similar tissue types the signal evolution will be alike and will not produce noticeable artifacts. If the relaxation times differ a lot a weighting function will be introduced like described in section 2.1.4 which will lead to considerable blurring artifacts [59]. As also described in section 2.1.4 there are several approaches to minimize such blurring artifacts including deconvolution with previously acquired T_2 maps, deconvolution with an average T_2 value along the phase encoding direction and blur reduction with signal averaging (NEX $\geq$ 2) [52].

FID Artifacts The advantages of using variable refocusing flip angle schemes with flip angles considerably lower than 180° also comes with some problems. As described in section 2.2.2 fractions of the magnetization are converted to the longitudinal plane, regrow with T_1 between the subsequent refocusing RF pulses (of course also between the excitation pulse and the first refocusing RF pulse) and are flipped to the transverse plane with later RF pulses to generate stimulated echoes. By converting the magnetization to the transverse plane also a free induction decay (FID) is generated. The amplitude of this FID is indirectly proportional to the flip angle, so for low flip angles a high FID amplitude is observed. Furthermore the amplitude is also dependent on the T_1 value of the specific tissue. Short T_1, compared to the length of the echo train, allows the transversal magnetization to become relatively large and result in a large FID. Long T_1 compared to the ETL will, on the other hand, not result in a large FID signal even with relatively low flip angle values for the refocusing RF pulse. These generated FID signals are partly captured and lead to intensity ripples in certain parts of the image. The FID signals are only strong for tissues with short T_1 (i.e. fat) compared to the echo train duration when very low flip angles are used for the refocusing RF pulses. Hence, FID artifacts only occur if this combination is existing in the area imaged [59]. To avoid FID artifacts averaging has proven to be very effective [68]. Also the application of spoiler or crusher gradients can significantly attenuate such artifacts [59].

Slab-Selective Imaging Owing to the fact that with slab-selective imaging the refocusing RF pulse affects the whole sensitive volume of the RF coil, that is used for

transmission, FID artifacts, as described above, can arise even from outside of the volume of interest and get back folded into the image. Presaturating the volume outside the imaged area can, in many cases, prevent such artifacts. However, presaturating applied before the echo train may be ineffective for tissue with very short T_1 in combination with low flip angles for refocusing RF pulses. The reason for this is, that due to the short T_1 time a large amount of longitudinal magnetization will regrow during the echo train and is captured during image acquisition. Averaging very effectively attenuates artifacts introduced from outside the volume of interest [59].

2.3 3D TurboFLASH

2.3.1 3D TurboFLASH Introduction

Haase et al. introduced a fast low angle shot (FLASH) sequence in 1986 to massively shorten scan time for gradient echo imaging [69]. To establish T_1 contrast, an inversion (180°) or a saturation (90°) pulse in conjunction with a FLASH sequence can be used [70]. This technique is also called snapshot FLASH [71], snapshot gradient-recalled acquisition in the steady state (GRASSE) [72] or TurboFLASH [70, 73]. In a general sense, for all these sequences, TurboFLASH will be used in this publication. It can be quite challenging to adapt the 2D approach introduced by Haase et al. for a 3D TurboFLASH sequence. During the long duration of a 3D imaging sequence the effect of the preparation pulse (inversion or saturation) applied at the beginning of the sequence, will get lost [74]. This problem is solved by applying a preparation pulse at certain points within the sequence. In general, a 3D TurboFLASH is called magnetization prepared rapid gradient echo (MP-RAGE) and typically consists of a three step cycle: (1) magnetization preparation for contrast control, (2) data acquisition with a short TR gradient echo sequence (FLASH) and (3) magnetization recovery for additional contrast control [75]. Such a sequence is schematically depicted in Figure 2.7.

2.3.2 3D TurboFLASH Sequence

In Figure 2.8 a schematic sequence diagram for a TurboFLASH sequence can be seen. First, a preparation pulse α transfers the longitudinal magnetization to a defined starting point, normally this is an inversion pulse (180°) or a saturation (90°) pulse. Between the preparation pulse and the first excitation pulse is a waiting period TI_1. Then a train of subsequent small excitation pulses β, with an echo spacing of TI_2, generates a set of gradient echoes. After the echo train follows a recovery time t_r. Following each excitation, the longitudinal magnetization is eliminated with the spoiler gradient S [76]. The repetition time TR can be calculated with the following Equation:

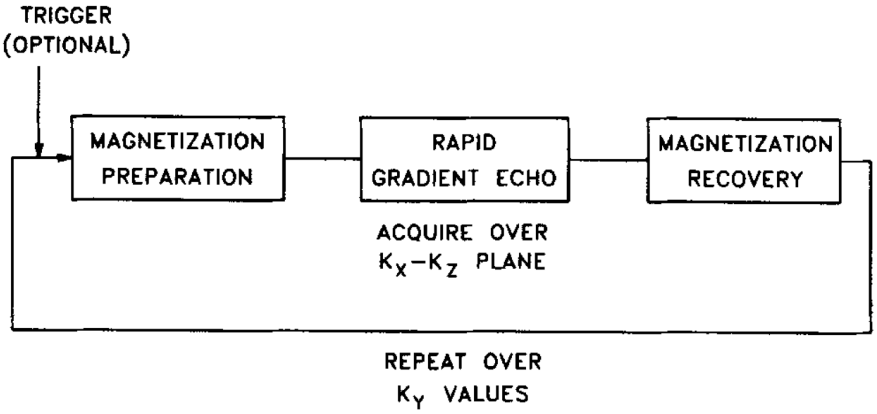

Figure 2.7: Schematic diagram of a 3D MP-RAGE sequence [75].

$$TR = TI_1 + (N-1)\,TI_2 + t_r \tag{2.8}$$

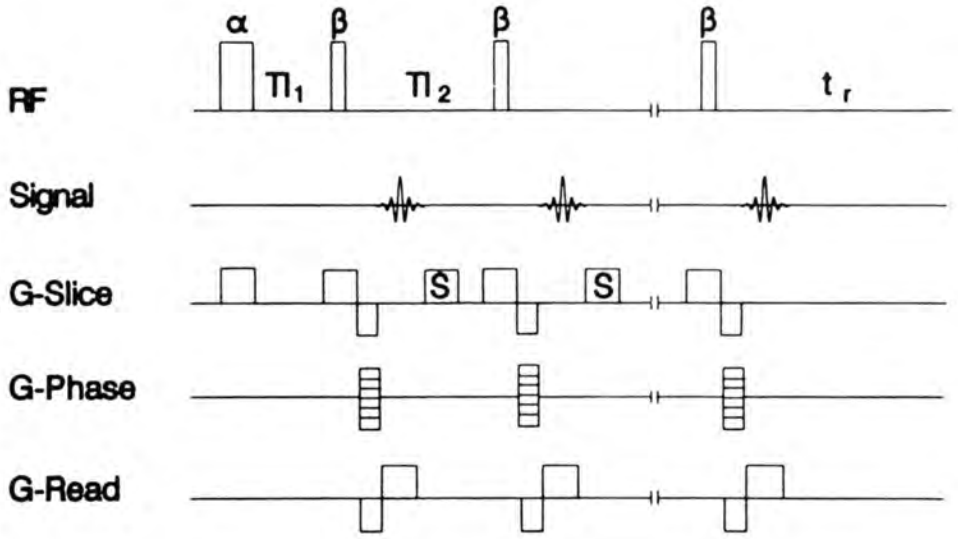

Figure 2.8: Schematic sequence diagram of a TurboFLASH sequence. First a preparation pulse α transfers the longitudinal magnetization to a defined starting point. Then a train of subsequent small excitation pulses β generates a set of gradient echoes After each excitation the longitudinal magnetization is eliminated with the spoiler gradient S [76].

In general for 3D sequences every phase encoding step in plane has to be carried out in the "slice" direction (z) also to fill the whole 3D k-space. The MP-RAGE fills this k-space in a special way. Within one cycle of the sequence, as depicted in Figure 2.7, the rapid gradient echo train fills one line of every slice (in the z direction). Hence, the turbo factor set on the scanner is always equal to the slices in the slab. This cycle is repeated for every phase encoding step (ky) in the image, and before every line cycle the magnetization is prepared [74, 75]. During the rapid gradient echo acquisition the longitudinal magnetization recovers according to the specific T_1 time and causes artifacts.

The amount of recovery is dependent on many variables like the preparation pulse α, the excitation pulse β, the waiting period TI_1 and the echo spacing TI_2 [70]. To minimize this T_1 decay these parameters can be optimized [77, 78] so that the longitudinal magnetization reaches a steady state where the T_1 relaxation compensates the loss of longitudinal magnetization [69]. This steady state can be reached within the first three rapid gradient echo cycles [70]. The signal contribution along the phase encoding direction in every single image plane is on the other hand always constant and thereby no blurring artifacts arise unless the images are reformatted and reconstructed in the slice encoding direction [74]. Figure 2.7 indicates the use of an optional trigger to initiate each cycle. This can be particularly useful for imaging structures with periodic motion [75]. The MP-RAGE sequence provides several advantages like continuous coverage with very thin slices in reasonable measurement time [74]. Its cyclic nature makes it particularly attractive for imaging structures with periodic motion (triggered) [75]. Additionally imaging time is much shorter compared to other existing steady-state acquisition schemes due to the separate magnetization preparation [75] and variable contrast (T_1 and T_2) as well as particularly good T_1 contrast due to different magnetization preparation pulses [75].

2.3.3 3D TurboFLASH Contrast

MP-RAGE can be used to produce T_1 as well as T_2 weighted images. By varying the magnetization preparation pulse or set of pulses the contrast can be dictated. For a T_1 weighting normally an inversion (180°) or a saturation (90°) pulse followed by a delay is used. Preparing the magnetization with an inversion pulse leads to a very strong T_1 weighting [75]. In fact, an inversion preparation pulse allows for a better control over T_1 weighting and leads to greater T_1 weighting compared to SE imaging [70, 74]. The waiting period TI_1 between the preparation pulse and the first excitation pulse plays a major role in contrast. This time is comparable to the inversion time of inversion recovery sequences. It controls the signal of different tissues and with the change of this parameter certain tissue types can be attenuated. Also, the excitation flip angle β plays a very important role in contrast behavior. The steady state in which the T_1 relaxation compensates the loss of longitudinal magnetization is determined by T_1 of the tissue and the excitation flip angle β. Therefore the T_1 contrast is strongly influenced by the flip angle [69]. A pulse set of 90° - 180° - 90° enables the MP-RAGE sequence to be used to produce T_2 weighted images [75] although MP-RAGE imaging is mostly used for T_1 weighted imaging. The contrast behavior of different tissues with the MP-RAGE sequence can be theoretically simulated by techniques introduced by Brix et al. [76].

2.3.4 3D TurboFLASH Image Artifacts

The fact that during the rapid gradient echo acquisition the longitudinal magnetization recovers according to the specific T_1 time of the tissue [70], introduces a weighting function (as described in 2.1.4) along the depth or slice encoding direction. The nonuniform T_1 weighting of the image leads to blurring [74]. As a result of acquiring all the in depth lines after one single preparation pulse before moving on to the next in plane line of the k-space leaves the in plane resolution compromised. All the data in one image plane is acquired with the same degree of relaxation and therefore does not show any blurring artifacts [21]. The blurring artifacts in phase encoding direction do not come into account until the data is reformatted and slices are reconstructed in depth direction [74].

Chapter 3

Methods

3.1 Signal to Noise Ratio

For Signal to Noise Ratio (SNR) measurements two different sequences were used in this study: a single sliced fast low angle shot (FLASH) sequence (TR = 25 ms, TE = 10 ms, FOV = 180 mm, matrix = 128, NEX = 1, slice thickness = 2.5 mm, flip angle = 10°, bandwidth = 260 Hz/pixel, acquisition time = 0:32 min) and a single sliced true fast imaging with steady precession (TrueFISP) sequence (TR = 4.32 ms, TE = 2.16 ms, FOV = 180 mm, matrix = 128, NEX = 1, slice thickness = 2.5 mm, flip angle = 40°, bandwidth = 558 Hz/pixel, acquisition time = 7.5 s). Both sequences were proton density weighted in order to limit T_1 and T_2 influences. All available filter settings were turned off and coil combine mode was set to sum of squares (SOS) for both sequences. Measurements were examined with a FLASH and a TrueFISP sequence with three different coil settings: only head coil, only loop coil and both in combination. The used coils were the standard head coil Siemens Head/Neck 20 A 3 T Tim Coil and the Siemens 3 T Loop 7 cm coil (Siemens, Erlangen, Germany). Head coil and surface coil where set up in combination and different coil combinations were realized via the scanner software. Every sequence was set up to have 10 measurements in order to avoid drift and to guarantee a steady state. All images were analyzed using an in-house image processing tool named "Perseus" and customized scripts in MATLAB (The MathWorks Inc., Natick, USA).

3.1.1 SNR Calculations

SNR values were calculated using the difference method suggested by the National Electrical Manufacturers Association (NEMA) [79]. For this method two images were acquired in the exact same manner. A pixel-by-pixel difference image (hereafter referred to as [image3]) was calculated as follows:

$$[image3] = [image1] - [image2] \tag{3.1}$$

Two statistical measurements, the signal intensity S and the standard deviation δ describing the noise, were required in order to calculate the SNR. For the difference method both of these values needed to be calculated from the same region of interest (ROI). The signal intensity was calculated as the mean of the ROI from image 1 and image 2 (hereafter referred to as S1 and S2, respectively), the standard deviation was calculated from [image 3], also using the same ROI. The SNR was calculated as follows:

$$SNR = \frac{(S1 + S2)/2}{\delta/\sqrt{2}} = \frac{S1 + S2}{\delta * \sqrt{2}} \tag{3.2}$$

3.1.2 SNR Phantom Measurements

For phantom measurements 10 scans were conducted using a Siemens plastic bottle (1900ml 8624186 K2285). The loop coil was taped directly on top of the phantom bottle for better stabilization, placed in the middle of the head coil and secured with sand bags to prevent motion. In order to guarantee independent measurements, the setting was disassembled and reassembled for every single measurement. The bottle as well as the loop coil were completely removed and repositioned. Before every measurement the phantom was given 10 min to settle in order to prevent incorrect SNR values due to motion of the fluid. For SNR analysis an eye sized ROI was placed within the phantom. The ROI was arranged in an average distance from the surface coil to an eye. For the SNR distance dependency measurement the signal intensities S1 and S2 were calculated using an intensity profile along a straight line (anterior-posterior) using Perseus, instead of using an ROI. For the standard deviation a ROI in the difference image was used covering the entire region of the drawn intensity line.

3.1.3 SNR In Vivo Measurements

For the in vivo SNR measurements 11 healthy, all men from age 22 to 28, test subjects were scanned. All subjects gave written informed consent, and the study was approved by the institutional ethics committee. The loop coil was placed over the left eye and medical tape and a velcro strip were used to lock the loop into position in order to prevent motion artifacts (Figure 3.1). The subjects were placed centered in the 20 channel head coil. Due to noise canceling head phones that made head movements nearly impossible no further head fixation was needed. On top of the head coil a mirror was installed to enable the test subjects to gaze on a projection screen at the foot end of the scanner. The test persons were instructed to fixate a cross that was shown on the screen in order to minimize eye movement during the scan. The ROI for SNR analysis was placed in the vitreous humor in a manner that maximizes the area of the ROI while targeting mainly a homogeneous region that is not affected by artifacts.

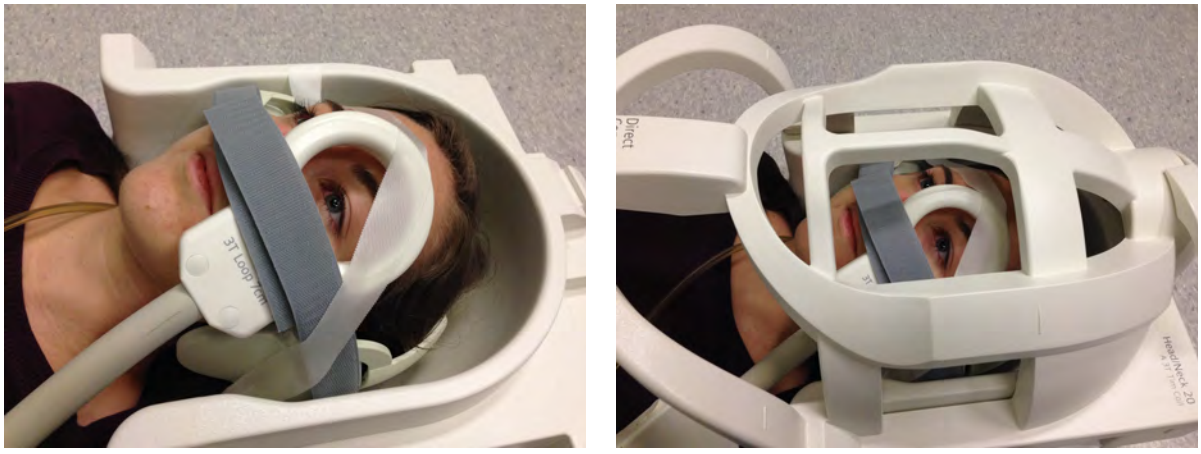

(a) (b)

Figure 3.1: For in vivo SNR measurements the small surface coil was placed over the left eye and fixated with a velcro strip and medical tape (a). Sequences were measured with three different coil settings: only head coil, only loop coil and both in combination (b).

3.2 Simulation of MR Sequences

3.2.1 TurboFLASH

The TurboFLASH sequence was simulated using MATLAB with the following formalism according to Brix et al. [76]. The longitudinal magnetization M_n just before the n-th read-out pulse is given by the equation 3.3 where $1 \leq n \leq N$, $c_\beta = \cos\beta$, $E_2 = e^{-TI_2/T_1}$, $F = (1 - E_2)/(1 - c_\beta E_2)$

$$M_n = M_{eq}\left[F + (c_\beta\, E_2)^{n-1}\,(Q - F)\right] \tag{3.3}$$

In this equation Q is the quotient of the longitudinal magnetization M_1 and the equilibrium magnetization M_{eq} where M_1 is just before the first interrogation pulse. The spin system can be seen to be in a steady state after some sequence cycles. The quantity Q in the steady state can be obtained by calculating the longitudinal magnetization $M(TR)$ from the condition $M(0) = M(TR)$, where $TR = TI_1 + (N-1)TI_2 + t_r$ is the sequence repetition time. Therefore for Q we get

$$Q = \frac{(F\, c_\alpha\, c_\beta\, E_r\, E_1\,[1 - (c_\beta\, E_2)^{N-1}]) + (c_\alpha\, E1\,(1 - E_r) - E_1 + 1)}{1 - c_\alpha\, c_\beta\, E_r\, E_1\,(c_\beta\, E_2)^{N-1}} \tag{3.4}$$

where $c_\alpha = \cos\alpha$, $E_1 = e^{-TI_1/T_1}$ and $E_r = e^{-t_r/T_1}$. Included in this Equation is the information about the evolution of the spin system across the whole sequence cycle which also includes the undisturbed recovery period t_r. This information is very important for stabilizing the tree-parameter fit. The amplitude S can now be calculated using

$$S = |s_\beta \, M_n \, e^{-TE/T_2^*}| \tag{3.5}$$

where $s_\beta = \sin\beta$, T_2^* is the characteristic decay constant of the FID and TE is the echo time.

3.2.2 Turbo Spin Echo

3.2.2.1 General Solution for Bloch Equations

The Turbo Spin Echo Sequence was simulated using a Bloch Equations based simulation algorithm in MATLAB. The Bloch Equations written in a compact form is given by:

$$\frac{\delta M}{\delta t} = M \times \gamma B - \frac{M_x i + M_y j}{T_2} - \frac{(M_z - M_o)k}{T_1} \tag{3.6}$$

[80,81]. A special solution to the Bloch Equations can be expressed in the form of rotation matrices if it is assumed that $1/\mathrm{T}_1$ and $1/\mathrm{T}_2 \ll \gamma \, \mathrm{B}_1$, where γ is the gyromagnetic ratio and B_1 is the radio frequency magnetic field. A simple rotation in direction of the x, y and z axes, about an angle φ can be written as follows:

$$R_x(\varphi) = \begin{pmatrix} 1 & 0 & 0 \\ 0 & \cos\varphi & -\sin\varphi \\ 0 & \sin\varphi & \cos\varphi \end{pmatrix} \tag{3.7}$$

$$R_y(\varphi) = \begin{pmatrix} \cos\varphi & 0 & \sin\varphi \\ 0 & 1 & 0 \\ -\sin\varphi & 0 & \cos\varphi \end{pmatrix} \tag{3.8}$$

$$R_z(\varphi) = \begin{pmatrix} \cos\varphi & -\sin\varphi & 0 \\ \sin\varphi & \cos\varphi & 0 \\ 0 & 0 & 1 \end{pmatrix} \tag{3.9}$$

In the same manner the free precession around the z axis over a time period τ can be expressed in the form of the following matrix, with Δf as the tissue off-resonance [81,82].

$$P(\tau) = \begin{pmatrix} \cos 2\pi\Delta f\tau & -\sin 2\pi\Delta f\tau & 0 \\ \sin 2\pi\Delta f\tau & \cos 2\pi\Delta f\tau & 0 \\ 0 & 0 & 1 \end{pmatrix} \tag{3.10}$$

Taking T_1 and T_2 relaxation over a time period τ into consideration results in a multiplication with the following matrix:

$$C(\tau) = \begin{pmatrix} e^{-\tau/T_2} & 0 & 0 \\ 0 & e^{-\tau/T_2} & 0 \\ 0 & 0 & e^{-\tau/T_1} \end{pmatrix} \tag{3.11}$$

and a summation of the following matrix:

$$D(\tau) = (I - C(\tau)) \begin{pmatrix} 0 \\ 0 \\ M_0 \end{pmatrix} = \begin{pmatrix} 0 \\ 0 \\ M_0 \left(1 - e^{-\tau/T_1}\right) \end{pmatrix} \tag{3.12}$$

In Equation 3.12 I represents the identity matrix. For reasons of simplification Equations 3.10 and 3.11 will be combined and from here on referred to as A(τ):

$$A(\tau) = C(\tau)\, P(\tau) \tag{3.13}$$

In conclusion, the magnetization M at timepoint τ can be expressed by:

$$M(\tau) = A(\tau)\, M_0 + D(\tau) \tag{3.14}$$

where M is a 3D vector representing the magnetization (M_x, M_y, M_z), A is a 3×3 matrix and B is a 3D vector. As seen above, A and B are functions of T_1, T_2, and various rotation and precession angles.

3.2.2.2 Simulation of the Bloch Equations for Turbo Spin Echo

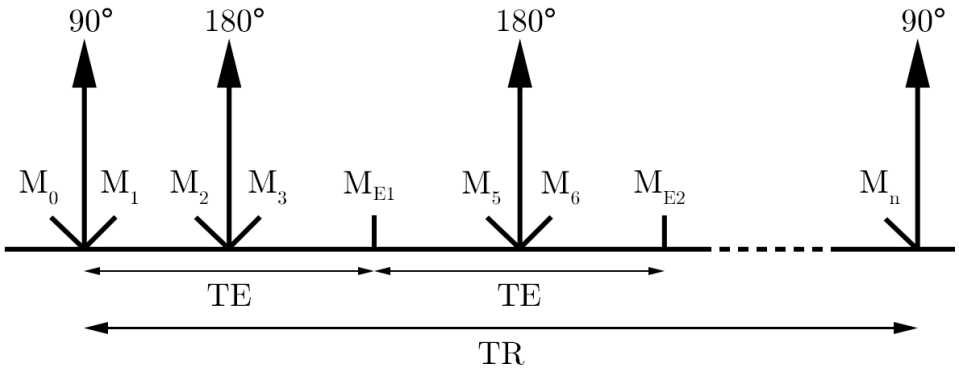

Figure 3.2: A TSE sequence applies an 90° RF excitation pulse followed by several 180° RF refocusing pulses to produce multiple spin echoes, a so called echo train. Magnetizations at several time points throughout the sequence are marked wit M_1 - M_n. Magnetizations at echo times are marked with M_{E1} and M_{E2}. In steady state M_n equals M_0.

By using the formalism introduced in Section 3.2.2.1 and the approach to simulate MR sequences with rotation matrices used by Hargreaves et al. [82] the magnetizations in Figure 3.2 are related by:

$$
\begin{aligned}
M_5 &= A(TE/2)\, M_{E1} + D(TE/2) \\
M_6 &= R_x(180°) M_5 \\
M_{E1} &= A(TE/2)\, M_6 + D(TE/2)
\end{aligned}
\tag{3.15}
$$

If M_{E1} is represented by M_k and M_{E2} by M_{k+1} then M_k and M_{k+1} are related in the same way as M_{E1} and M_{E2} and represent the magnetizations at consecutive echo times. Solving Equation 3.15 for M_k yields

$$
M_{k+1} = A_{TE}\, R_{refoc}\, A_{TE}\, M_k + A_{TE}\, R_{refoc}\, D_{TE} + D_{TE} \tag{3.16}
$$

with

$$
\begin{aligned}
A_{TE} &= A(TE/2) \\
R_{refoc} &= R_x(180°) \\
D_{TE} &= D(TE/2).
\end{aligned}
$$

For a correct estimation of the magnetization at each echo time the start value for the magnetization already has to be the magnetization in the steady state. This magnetization is calculated for ETL = 2 by evaluating the following relationships of the magnetizations seen in Figure 3.2.

$$
\begin{aligned}
M_1 &= R_{flip}\, M_0 \\
M_2 &= A_{TE}\, M_1 + D_{TE} \\
M_3 &= R_{refoc}\, M_2 \\
M_{E1} &= A_{TE}\, M_3 + D_{TE} \\
M_{E2} &= A_{TE}\, R_{refoc}\, A_{TE}\, M_{E1} + A_{TE}\, R_{refoc}\, D_{TE} + D_{TE} \\
M_n &= M_0 = A_{TR}\, M_{E2} + D_{TR}
\end{aligned}
\tag{3.17}
$$

where

$$
\begin{aligned}
A_{TR} &= A(TR - ETL * TE) \\
A_{TE} &= A(TE/2) \\
R_{refoc} &= R_x(180°) \\
R_{flip} &= R_y(90°) \\
D_{TE} &= D(TE/2) \\
D_{TR} &= D(TR - ETL * TE).
\end{aligned}
$$

Solving Equations 3.17 for M_1, with a representation by M_{ss}, yields the steady state

magnetization right after the 90° excitation pulse. Further generalization of the equation for application of arbitrary echo train length leads to

$$M_{ss} = inv(I - X) * Y \tag{3.18}$$

where the matrices X and Y are representing the relaxation and rotation propagated through the whole echo train including the 90° excitation pulse. In order to acquire, these matrices A(τ) and D(τ) are propagated through the entire echo train by Equations 3.19.

$$\begin{aligned} A_{k+1} &= A_{TE}\, R_{refoc}\, A_{TE}\, A_k \\ D_{k+1} &= D_{TE} + A_{TE}\, R_{refoc}\, (D_{TE} + A_{TE}\, D_k) \end{aligned} \tag{3.19}$$

where

$$\begin{aligned} &k = 1, ..., ETL \\ &A_{k=1} = I \\ &D_{k=1} = \begin{bmatrix} 0 \\ 0 \\ 0 \end{bmatrix} \end{aligned}$$

The 90° excitation pulse is taken into account by expanding the matrices $A_{k=ETL}$ and $D_{k=ETL}$, propagated already through the echo train by

$$\begin{aligned} X &= R_{flip}\, A_{TR}\, A_{k=ETL} \\ Y &= R_{flip}\, (D_{TR} + A_{TR}\, D_{k=ETL}). \end{aligned} \tag{3.20}$$

The calculated steady magnetization from Equation 3.18 is inserted into Equation 3.16 to estimate the magnetization for every echo of the echo train. The signal generated at every echo time can be calculated as follows:

$$S = |M_x + iM_y| \tag{3.21}$$

The magnetization at different echo times throughout the echo train was simulated for thousand random off-resonances ranging from -70 Hz to +70 Hz. The final signal amplitude was obtained by calculating the mean of these thousand resulting magnetizations.

3.2.3 Spin Echo

The SE sequence was simulated using a Bloch Equations based simulation algorithm (Section 3.2.2.1) in MATLAB. By using this formalism and the approach to simulate MR

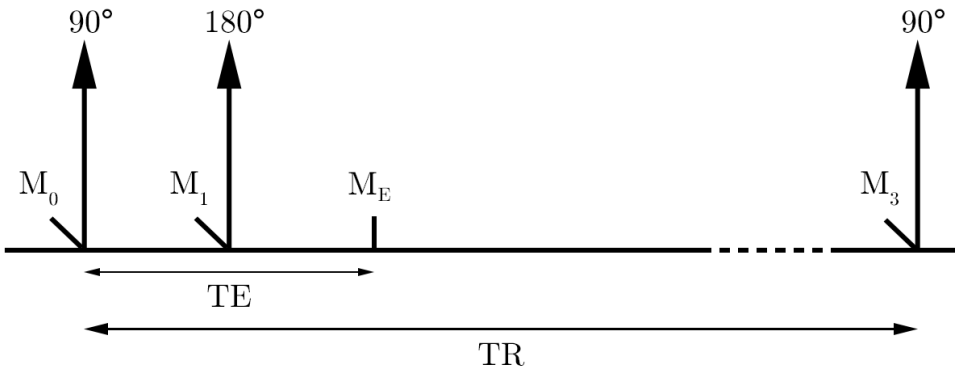

Figure 3.3: A SE sequence applies an 90° RF excitation pulse followed by an 180° RF refocusing pulse to produce a spin echo at time point TE. Magnetization at several time points throughout the sequence are marked with M_1 - M_3. Magnetizations at the echo time TE is marked with M_E. In steady state M_3 equals M_0.

sequences with rotation matrices used by Hargreaves et al. [82] the magnetizations in Figure 3.3 are related by:

$$\begin{aligned} M_1 &= A_{TE}\, R_{flip}\, M_0 + D_{TE} \\ M_E &= A_{TE}\, R_{refoc}\, M_1 + D_{TE} \\ M_3 &= M_0 = A_{TR}\, M_E + D_{TR} \end{aligned} \tag{3.22}$$

where

$$\begin{aligned} A_{TR} &= A(TR - TE) \\ A_{TE} &= A(TE/2) \\ R_{refoc} &= R_x(180°) \\ R_{flip} &= R_y(90°) \\ D_{TE} &= D(TE/2) \\ D_{TR} &= D(TR - TE). \end{aligned}$$

Solving Equation 3.22 for M_E and letting it be represented by M_{ss} results in

$$M_{ss} = inv(I - A_{TE}R_{refoc}A_{TE}R_{flip}A_{TR}) * (D_{TE} + A_{TE}R_{refoc}(D_{TE} + A_{TE}R_{flip}D_{TR})). \tag{3.23}$$

The signal generated at the echo time TE can be calculated using Equation 3.21. The signal for a given SE sequence can also be determined using Equation 3.24 [52] and would lead to the same signal amplitude for the SE sequence. This was done for verification of results.

$$S = M_0 \left(1 - 2\, e^{-(TR-TE/2)/T_1} + e^{-TR/T_1}\right) e^{-TE/T_2} \tag{3.24}$$

3.3 Optimizing Sequence Parameters

3.3.1 T_1 and T_2 Estimation of Melanoma

T_1 and T_2 values of uveal melanoma are necessary for subsequent theoretical optimization of the TSE and FLASH sequences and are not available in the current literature. Therefore the following approach was used to estimate these relaxation times. Images used for estimation originate from University Hospital Essen, Department of Diagnostic and Interventional Radiology and Neuroradiology, Essen, Germany and were obtained at a Siemens MAGNETOM Aera 1.5 T using two small surface coils (diameter < 5 cm) [9, 83]. A SE (T_1 weighted) and a TSE sequence (T_2 weighted) were used to obtain the images.

T_{1w} SE sequence The SE sequence was obtained with the following parameters, TR = 642 ms, TE = 16 ms, FOV = 108 x 80 mm, matrix = 344 x 512, NEX = 2, slices = 22, slice thickness = 2 mm, flip angle = 90°, bandwidth = 60 Hz/pixel and acquisition time = 8:49 min.

T_{2w} TSE sequence TSE imaging was carried out using the following parameters, TR = 6440 ms, TE = 171 ms, FOV = 108 x 80 mm, matrix = 344 x 512, NEX = 3, slices = 22, slice thickness = 2 mm, flip angle = 150°, bandwidth = 70 Hz/pixel, turbo-factor = 13 and acquisition time = 10:12 min.

Signal intensities of several tissues including eye muscles, fatty tissue surrounding the eye, vitreous humor and melanoma were obtained by drawing the exact same regions of interest (ROI) in both images using a middle slice through the bulb including the melanoma. To obtain relationships between these tissues the mean pixel values of the ROIs were plotted, normalized to muscle, against each other (T_{1w} x-axis, T_{2w} y-axis). In oder to replicate these relationships the T_{1w} SE and the T_{1w} TSE sequences were simulated like described in Section 3.2.3 and 3.2.2, respectively with the same settings as used on the MR scanner at the University Hospital Essen. Simulated T_{1w} and T_{2w} signal values for tissues with available relaxation times from the literature (vitreous humor, fatty tissue and muscle) where plotted in the same manner as described for the obtained pixel values. Relaxation times for muscle and fatty tissue were found in the literature to be $T_1 = 1412$ ms and $T_2 = 50$ ms for muscle [84] and $T_1 = 382$ ms and $T_2 = 68$ ms for fatty tissue [85]. As no values were available in the literature for vitreous humor, they were measured in a cow eye using the method described in Section 3.3.1.1. Proton densities for

the simulated tissues where normalized to water ($\rho = 1$) and where found in the literature to be $\rho = 0.79$ for muscle [86], $\rho = 1$ for fatty tissue and $\rho = 0.9$ for melanoma [23].

3.3.1.1 T_1 /T_2 Measurement for Vitreous Humor

T_1 and T_2 values for vitreous humor were obtained from an enucleated cow eye. Muscles and surrounding fatty tissues were removed, the eye was enclosed in a 5 cm plastic sphere and embedded in agar gel. The sphere was imaged with a multi echo spin echo and an inversion recovery sequence in order to fit T_2 and T_1 values, respectively. MRI experiments were performed on a Siemens MAGNETOM Skyra 3 T using a circular polarized whole body volume coil for rats with an inner diameter of 7 cm (RAPID Biomedical GmbH, Rimpar, Germany).

Inversion Recovery Inversion recovery sequences used for T_1 measurements were carried out using the following parameters: TR = 10000 ms, TE = 13 ms, FOV = 120 mm, matrix = 512, NEX = 2, slices = 9, slice thickness = 1 mm, bandwidth = 335 Hz/pixel and turbofactor = 7. Inversion times of TI = 50, 100, 200, 400, 800, 1600, 3200 and 4200 ms were used.

Multi Echo Spin Echo The multi echo spin echo sequence used for T_2 measurements was obtained with the following parameters, TR = 5000 ms, TE = 15.2 ms, FOV = 120 mm, matrix = 512, NEX = 5, slices = 9, slice thickness = 1 mm, turbofactor = 32 and bandwidth = 200 Hz/pixel.
Relaxation times T_1 and T_2 were determined using a Marquardt-Levenberg fit of Equations 3.25 and 3.26, respectively [87].

$$M_z(TI) = |M_{z0}\,(1 - 2e^{-TI/T_1})| \tag{3.25}$$

$$M_{xy}(TE) = M_{xy0}\,e^{-TE/T_2} \tag{3.26}$$

3.3.2 Theoretical Sequence Optimization

In order to optimize the TurboFLASH and the TSE sequence, they were simulated with the methods described in Section 3.2.1 and 3.2.2, respectively for different T_1 and T_2 tissue values using MATLAB. Different sequence parameters were varied and the resulting signal behavior was plotted.

3.3.2.1 TurboFLASH

The TurboFLASH sequence was simulated for a 128 x 128 matrix with a preparation flip angle α of 90°. The flip angle β was varied from 1° to 90°, TI_1 was modified from 1 ms to 500 ms, TI_2 differed in a range of 1 ms to 100 ms and TE was altered from 1 ms to 100 ms.

3.3.2.2 Turbo Spin Echo

Simulations for the TSE sequence were carried out using a turbofactor of 18 and an echo spacing of 11.3 ms. The sequence was replicated for 1000 off resonance frequencies ranging from -70 Hz to +70 Hz. To achieve the final signal the average value of these 1000 resulting signal intensities was calculated. The refocusing flip angle, TE and TR were modified for different tissues. TR was varied in a range of 200 ms to 10 000 ms, TE differed from 11.3 ms to 203.4 ms and the refocusing flip angle was modified from 1° to 180°.

3.3.2.3 SPACE

The SPACE sequence was optimized on a Siemens MAGNETOM Skyra 3 T using the standard head coil Siemens Head/Neck 20 A 3T Tim Coil. In order to optimize the sequence on the same tissue types as TurboFLASH and TSE sequence, pork belly was used to represent fatty tissue and muscle tissue. For vitreous humor a bottle of distilled water was used as a phantom. The sequence was operated with the following settings FOV = 190 mm, matrix = 256, NEX = 1, slice thickness = 2 mm, bandwidth = 630 Hz/pixel and turbo factor 38. The variable flip angle was optimized for T_1 measurement. The TR was varied from 306 ms to 6000 ms in the following steps: 306, 400, 600, 900, 1200, 1500, 2000, 2500, 3000, 4000, 5000 and 6000 ms with a TE set to 12 ms. TE was modified in a range of 4.1 ms to 78 ms in the steps of 4.1, 8.3, 12, 17, 21, 25, 37, 45, 54, 62 and 78 ms with a TR set to 700 ms.

3.3.3 Practical Sequence Optimization

The practical implementation of the theoretically optimized sequences was done on a Siemens MAGNETOM Skyra 3 T. All three sequences were first tested on a phantom using the standard head coil Siemens Head/Neck 20 A 3T Tim Coil. Further improvement of image quality, SNR and resolution was done on healthy test subjects. Finally the sequences were implemented, for initial patient tests, at the University Hospital Graz at a Siemens MAGNETOM Verio 3 T using a Siemens 32 channel head coil.

3.4 medEyeTrack

Introduction As part of a cooperation between the Medical University of Graz (Department of Therapeutic Radiology and Oncology), Graz University of Technology (Institute for Computer Graphics and Vision) and M&R Automation GmbH [49], a revolutionary system called medEyeTrack was developed. This system enables recording of the viewing direction of a patient during treatment at a rate of 10 times per second. If a predefined threshold of the desired eye position is exceeded, the medEyeTrack provides a signal

which can for instance be used to trigger external systems like CT, LINAC or MR. This non-invasive eye tracking solution enables multiple radiation therapy treatment sessions of tumors within the orbits per person for the first time [49].

medEyeTrack in Detail By using a camera system the relative position of the eyes to a desired position is fully automatically monitored 10 times per second (schematic structure can be seen in Figure 3.4a). Each eye is observed with an individual camera and is illuminated with an infrared light source. The exact eye position can be recorded during the course of the measurement and as soon as the predefined threshold is exceeded the medEyeTrack can trigger external systems within milliseconds. The user interface of the eye tracking software including the current eye position (blue cross) and the desired position (white circle with cross in the middle) can be seen in Figure 3.4b. Also included in this figure is the graph showing the deviation of the desired eye position. A blinking LED positioned between both cameras helps the patient to keep the eye position constant and is used as a reference point for the desired eye position. To avoid head movement an individually fitted head mask, that can be mounted on the medEyeTrack, is used for each patient (Figure 3.5). The whole system was constructed in order to be compatible with different medical imaging and treatment systems like CT, LINAC or MR [49].

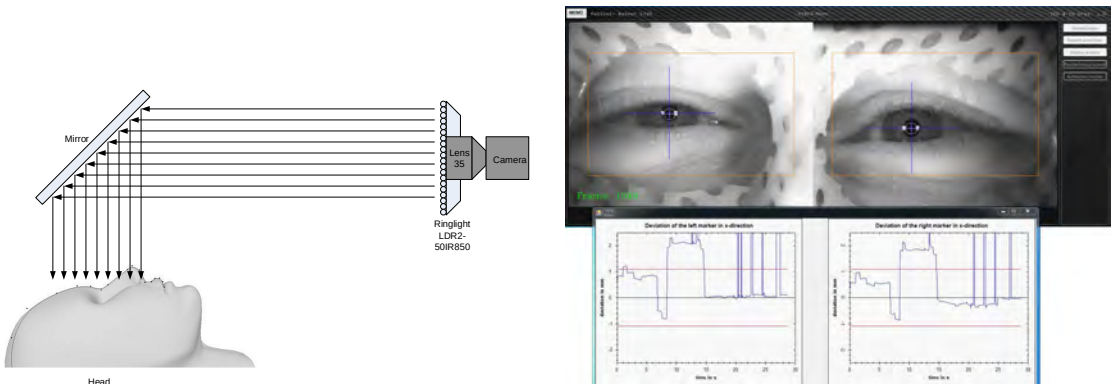

(a) (b)

Figure 3.4: Schematic camera setup of the medEyeTrack consisting of camera, light source, mirror and a phantom head (a). The interface of the eye tracking software shows the current eye position (blue cross), the desired position (circle with cross in the middle), the current frame number and the deviation of the desired position (graph at the bottom) (b).

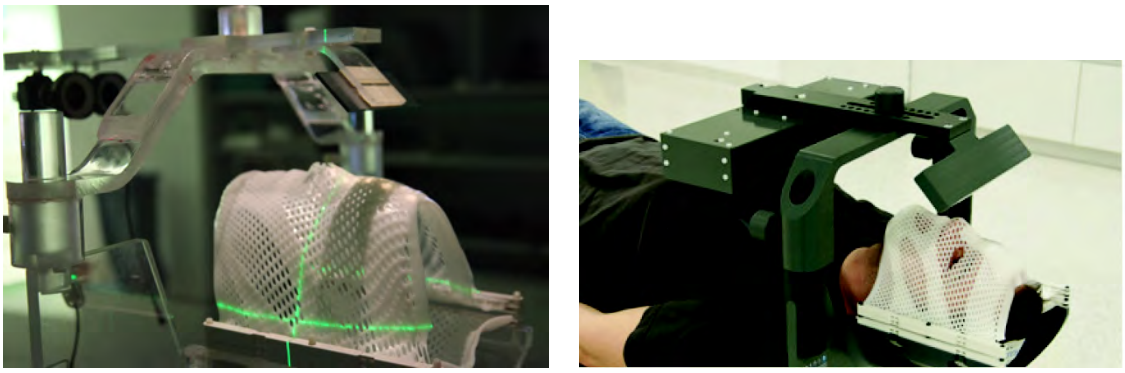

(a) (b)

Figure 3.5: Early prototype of the medEyeTrack system with custom fitted patient mask to avoid patient head movement (a). Current setup of the system manufactured by M&R Automation GmbH (b).

3.5 Triggering of an MR Sequence using the medEyeTrack System

3.5.1 MR Trigger Setup

Figure 3.6 shows the general setup for the trigger experiment. The medEyeTrack was installed on a Siemens MAGNETOM Skyra 3 T system with the standard head coil Siemens Head/Neck 20 A 3T Tim Coil. The scanner was connected to the medEyeTrack via the external trigger connection. For this test setup the trigger signal was generated by a waveform generator (HP 33120A, Hewlett Packard, California, USA). A simple square-wave signal with $U_{ss} = 4\,\mathrm{V}$, $U_{offset} = +2\,\mathrm{V}$, f = 2.9 Hz (specifications were extracted from the scanner handbook) was used. The waveform generator was operated in the "External Gated Burst Mode", which allows an external signal to toggle the output of the generator. When a high TTL level is present on the external trigger input terminal, the function generator outputs the carrier waveform. When a low TTL level is present, the output is disabled. Whenever the current eye position exceeds the predefined threshold of the desired position the relais unit applies a low TTL level to the external trigger input and the output of the waveform generator is disable which pauses the MR scanner.

3.5.2 MR Sequence used for Triggering

A 3D TurboFLASH sequence (MP-RAGE) with the following parameters was used for acquisition: TR = 326 ms, TE = 2.91 ms, TI = 180 ms, FOV = 170 mm, matrix = 192, NEX = 1, slices = 40, slice thickness = 1 mm, flip angle = 12°, bandwidth = 270 Hz/pixel, turbofactor = 40 and acquisition time = 2:05 min.

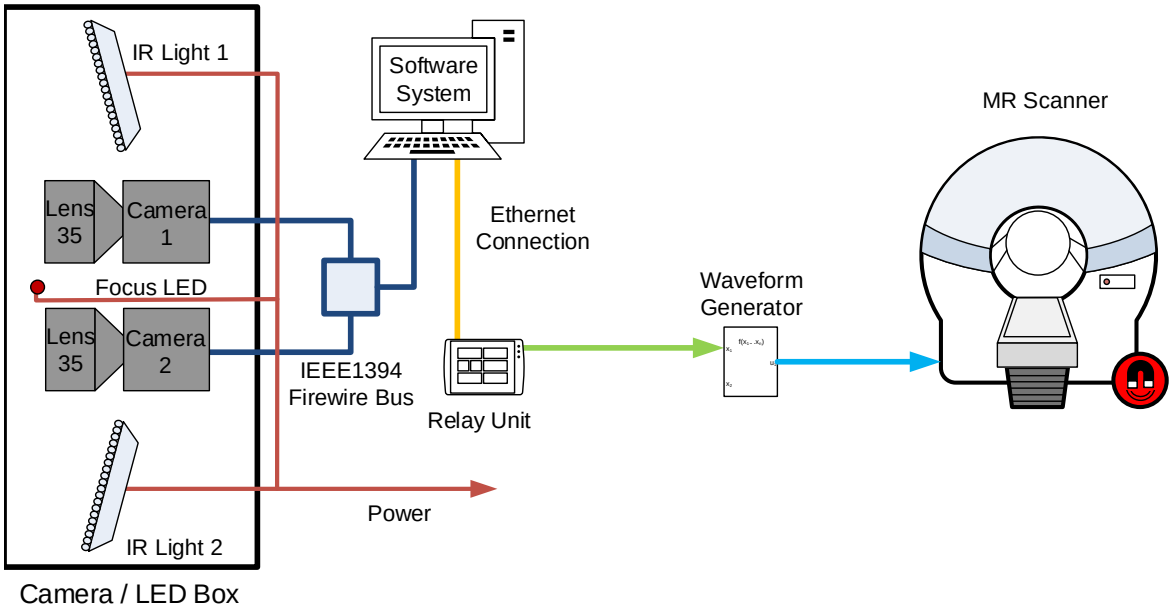

Figure 3.6: The schematic setup of the medEyeTrack in combination with the connected MR scanner and the waveform generator in order to trigger an MR sequence.

3.5.3 Subject Setup

Six test subjects, five female and one male ranging from age 23 to 31, were evaluated. All subjects gave written informed consent, and the study was approved by the institutional ethics committee. For every test subject an individually fitted mask was manufactured at the University Hospital Graz. Subjects were placed in the eye tracker and fixated with the mask to prevent head motion. A total of six different experiments, with varying eye movement schemes, were conducted using the MR sequence described above. For the different movement schemes the subjects were asked to close and hold their eyes still as good as possible (1), fixate the LED during the whole measurement (2), move their eyes away from the LED every 10 (3) and every 20 seconds (4). The schemes with voluntary eye movements (10 s and 20 s) were carried out twice, untriggered (3-4) and triggered (5-6). To advise the test subject when to start the eye movement a light impulse was used. Therefor the scan room was darkened and a projector was used to show a bright image every 10 or 20 seconds to enlighten the room which was noticeable by the test subjects. The bright image was shown for 2 seconds and subjects were instructed to look away from the LED as long as the bright image is present and to resume fixating the LED as soon as the room turned dark again.

3.5.4 Image Analysis

3.5.4.1 Qualitative Image Analysis

The qualitative image analysis was performed by 7 experts of different fields of expertise (ophthalmology, radiooncology, radiology, MRI engineering). At the time of evaluation the examiners where blinded to the test subjects' identity and the used eye movement scheme. Test subjects and movement schemes were presented in random order on the same workstation with Perseus software. For every imaging setup 3 slices of the mid section of the bulb were presented and examiners were able to change slices and the applied window setting as desired. The evaluators were asked to only pay attention to the orbital region. The analysis was performed via a grading system from 1 - 5 for three different criteria including overall image quality in the orbital region, anatomical recognizability and amount of artifacts present in the image. For the rating of overall image quality and anatomical recognizability the scale was 1 = excellent, 2 = good, 3 = moderate, 4 = poor and 5 = non-diagnostic. Artifacts in the images were rated with 1 = none, 2 = minimal, 3 = moderate, 4 = major and 5 = non-diagnostic.

3.5.4.2 Quantitative Image Analysis

To automatically evaluate the amount of motion artifacts in the recorded images, a metric called gradient entropy, introduced by McGee et al. [88], was used. The gradient entropy can be calculated by applying a one dimensional image gradient along the phase encoding direction of the image. The entropy is calculated from the resulting gradient image (see Equation 3.27). Calculations were performed in MATLAB.

$$F = -\sum_{i,j} h_{i,j}\, log_2\, h_{i,j} \tag{3.27}$$

where

$$h_{i,j} = \frac{\left| \begin{bmatrix} 1 \\ 0 \\ -1 \end{bmatrix} * g_{i,j} \right|}{\sum_{i,j} \left| \begin{bmatrix} 1 \\ 0 \\ -1 \end{bmatrix} * g_{i,j} \right|}$$

For evaluation of images from the different eye movement schemes only a 40 pixel high band depicting the eye was used (example see Figure 3.7). The gradient entropy was calculated in phase and frequency encoding direction and both values were summed up. Such

a gradient entropy was calculated for 20 slices building the whole 3D volume containing the eye. Values for every single slice where summed up to yield the over all gradient entropy of the desired 3D volume.

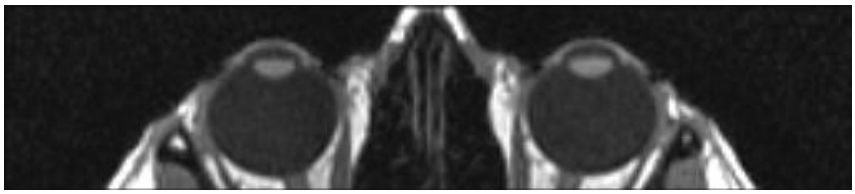

Figure 3.7: A 40 pixel high band depicting the eye was used from every slice to calculate the gradient entropy in phase and frequency encoding direction. In this figure an example of one slice can be seen.

3.6 Statistical Methods

SNR Measurements The statistical significance between groups for the SNR data was assessed using analysis of variance (ANOVA) for repeated measurements, followed by pairwise t-test corrected with Holm as post hoc test. Statistical tests were performed using the statistic language and environment R (R Foundation for Statistical Computing, Vienna, Austria) [89]. A p-value lower than 0.05 was considered statistically significant.

Qualitative Image Analysis The nonparametric Wilcoxon matched pairs signed rank test was used for every criteria in the qualitative analysis as normal distribution of the data could not be assumed. A p-value lower than 0.05 was considered statistically significant. Statistical tests were performed using GraphPad Prism 6 (GraphPad Software, Inc., CA, USA).

Quantitative Image Analysis To evaluate the difference of calculated gradient entropy between different movement schemes a single paired t-test was used. A p-value lower than 0.05 was considered statistically significant. Statistical tests were performed using GraphPad Prism 6.

Chapter 4

Results

4.1 Signal to Noise Ratio Measurements of Different Coil Settings

For SNR calculations of different coil settings 10 phantom measurements and 11 test subject measurements with three different coil settings were conducted. SNR values in the following are given as average over 10 phantom or 11 test subject measurements and were calculated as described in Section 3.1.

4.1.1 SNR Phantom Measurements

When using a small surface coil, without or in combination with the standard head coil, for imaging the phantom, SNR values were observed to be considerably higher compared to usage of the head coil alone. SNR values appeared to be highly dependent on the distance to the coil and decrease drastically with increasing distance (Figure 4.1). When normalizing the measured SNR data to the standard head coil, the small surface coil yields higher SNR values up to a distance of about 4.5 cm, compared to the head coil. Combined usage of the L7 coil and the standard head coil resulted in slightly lower SNR values in close distance to the surface coil (up to a distance of about 2 cm) compared to using just the L7 coil. At 2 cm the SNR values exceed the SNR values for the surface coil alone and showed SNR enhancement starting from there. The combination showed higher SNR values compared to the head coil up to about 6 cm and yielded equal results from there on.

SNR data achieved with the FLASH sequence in the transversal plane (Figure 4.2a) showed a significant difference for the three coil settings used (ANOVA with repeated measurements $F(2,18) = 1261$, $p = 2 * 10^{-16}$). A 3.34 ($p = 5.3 * 10^{-12}$) and 3.15 fold ($p = 1 * 10^{-12}$) increase in SNR was observed when using the surface coil (L7) and L7 in combination with the head coil compared to using only the head coil, respectively.

Using only the L7 coil resulted in a significantly higher SNR compared to combined usage with the head coil (146.72 and 138,27, respectively, p = 0.021). Similar results can be observed for the coronal plane (Figure 4.2b). A significant difference (F(2,18) = 438,9, p = $5.34 * 10^{-16}$) was observed over the three coil settings. Using only the L7 coil resulted in a 3.27 fold increase of SNR compared to the head coil (p = $7.5 * 10^{-9}$). A 3.09 fold increase in SNR was observed using the L7 in combination with the head coil in contrast to the head coil alone (p = $5.9 * 10^{-9}$). Similarly to the transversal measurement, the L7 resulted in a significantly higher SNR than the combination of L7 and head coil (p = 0.0078).

Using a TrueFISP sequence with the same coil test setup showed similar results as the FLASH sequence. Transversal as well as coronal scans yielded significant SNR differences (F(2,18) = 729.2, p = $2 * 10^{-16}$ and F(2,18) = 596.6, p = $2 * 10^{-16}$, respectively). In the transversal scans (Figure 4.3a) both settings, L7 alone and L7 in combination with the head coil, led to a significant increase in SNR measured against the head coil alone (3.2 fold (p = $3.9 * 10^{-12}$) and 3.01 fold (p = $6.5 * 10^{-10}$), respectively). No significant difference could be observed when using the L7 coil in combination with the head coil instead of using the L7 coil alone (p = 0.053), the mean SNR values of both setups were calculated to be 270.5 and 285.9, respectively. In the coronal scan plane (Figure 4.3b) on the contrary, a significant difference between these two coil settings could be observed (p = 0.01). The mean SNR value for L7 alone was 283.6 and for L7 in combination with the head coil 263.7. Comparing these two setups to the head coil alone resulted in a significant SNR gain of 3.33 (p = $7.1 * 10^{-10}$) and 3.10 (p = $7.3 * 10^{-10}$), respectively.
For a clear overview all SNR mean values and the SNR enhancement of the given setup compared to the head coil alone are summarized in Table 4.1.

4.1.2 SNR In Vivo Measurements

Results of the SNR measurements of 11 test subjects showed a similar picture to the phantom measurements, as the SNR values for the small surface coil were observed to be higher than with the head coil alone. For the FLASH sequence in the transversal as well as in the coronal plane a significant difference in SNR values was observed (F(2,20) = 20.49, p = $1.44 * 10^{-5}$ and F(2,18) = 31.96, p = $1.39 * 10^{-6}$, respectively). The post hoc test for the transversal plane (Figure 4.4a) showed a significant increase in SNR for L7 and for L7 in combination with the head coil compared to the head coil alone (1.48 fold (p = 0.00036) and 1.47 fold (p = 0.00192), respectively). A significant change in SNR when comparing L7 alone with L7 in combination with the head coil could not be seen (p = 0.878). Mean SNR values of 42.2 and 41.2, respectively were encountered for these two setups. Comparing them in the coronal plane (Figure 4.4b) on the other hand resulted in a significant difference (p = 0.0036) as the mean values differed from 48.2 for

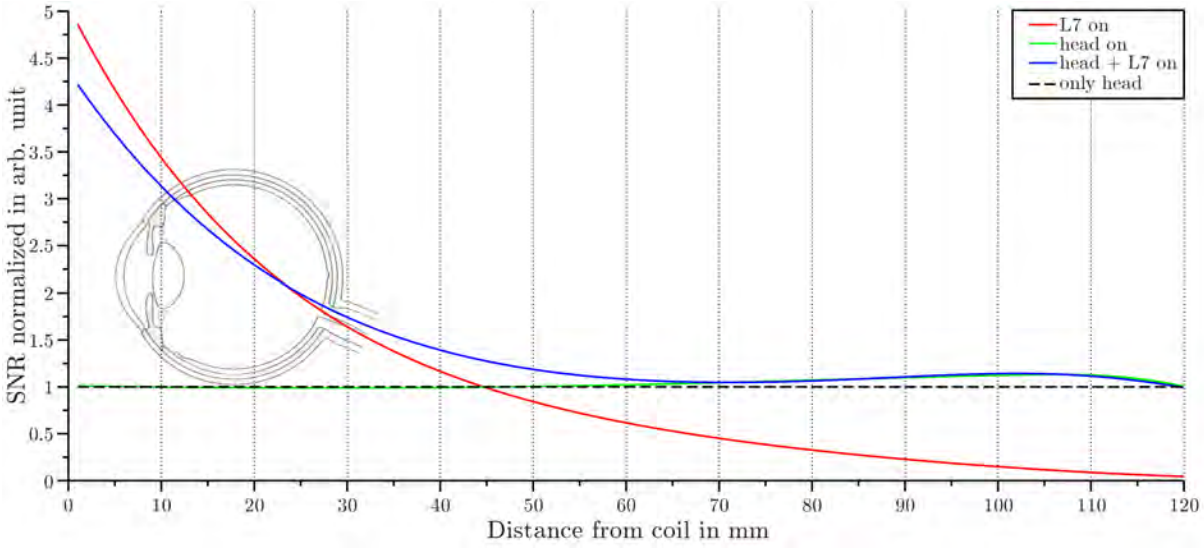

Figure 4.1: SNR enhancement compared to the standard head coil as a function of distance from the surface coil measured in phantoms (n=10) for different coil setups. The setups "L7 on", "head on" and "head + L7 on" are the same ones used for the following phantom measurements. Therefor, coils were setup in combination and were only enabled/disabled from the scanner software. For "only head" the standard head coil alone was used in the absence of any other coil. The schematic picture of the eye is depicted in actual distance to the surface coil and serves as an indicator for eye position and size, and to show the SNR trend as function of the distance along the course of the bulb.

L7 alone to 37.58 for the combination with the head coil. A comparison of both setups with the head coil alone yielded a significant gain of SNR. A 1.59 fold ($p = 1.1 * 10^{-5}$) increase for L7 alone and a 1.24 fold ($p = 0.027$) increase for the combination with the head coil was observed.

The same test setup executed with the TrueFISP sequence resulted in outcomes akin to the FLASH sequence. For both orientations, transversal as well as coronal, a significant difference in SNR values for the three coil settings could be observed ($F(2,20) = 24.29$, $p = 4.45 * 10^{-6}$ and $F(2,18) = 18.34$, $p = 2.99 * 10^{-5}$, respectively). Comparing the L7 coil alone to the combination with the head coil in the transversal plane (Figure 4.5a) did not lead to a significant increase in SNR ($p = 0.069$). Mean SNR values of 150.4 and 137.78, respectively were detected. In contrast to only the head coil these two setups showed a significant increase in SNR. Values of 1.69 ($p = 4.4 * 10^{-6}$) and 1.55 ($p = 0.00053$) times higher were revealed. Similar to the transversal plane also for the coronal plane (Figure 4.5b) mean values of 152 and 126.4 for L7 and L7 in combination with the head coil, respectively did not show a significant difference ($p = 0.069$). Significant SNR enhancement of 1.67 times ($p = 8.3 * 10^{-6}$) and 1.39 times ($p = 0.014$) could be shown for L7 and L7 in combination with the head coil, respectively when comparing them with the head coil alone.

For a clear overview all SNR mean values and the SNR enhancement of the given setup

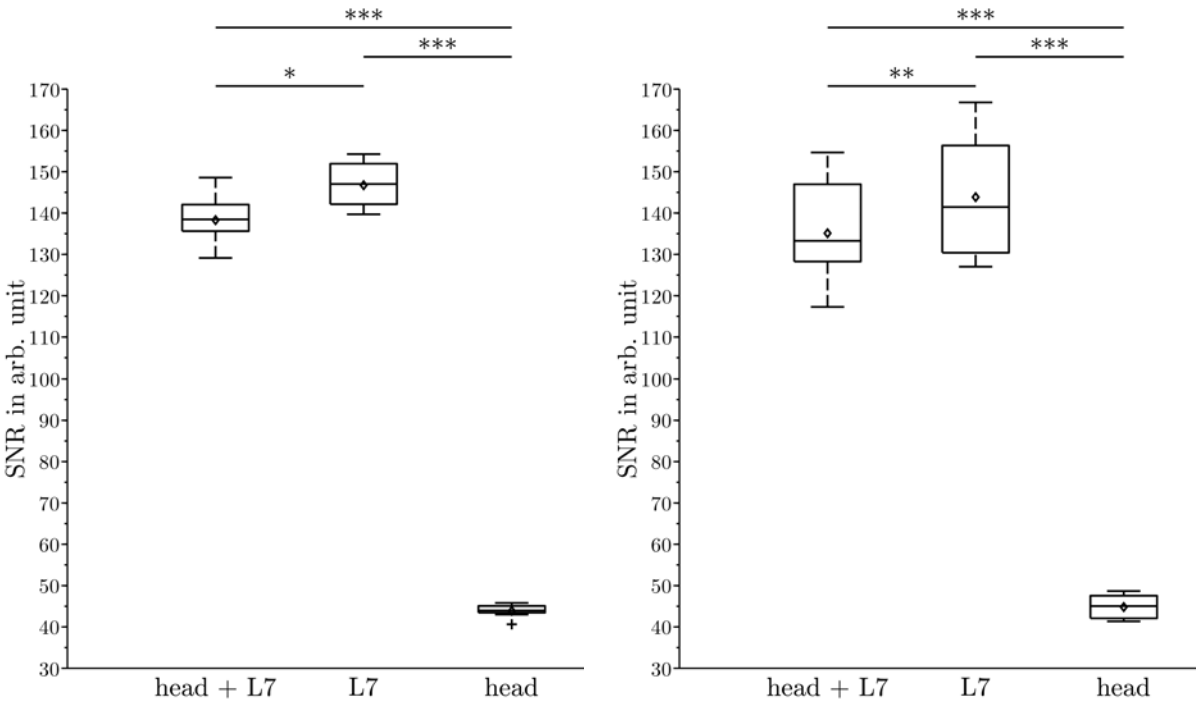

Figure 4.2: SNR box plots for the FLASH sequence transversal (a) and coronal (b) measured in phantoms (n = 10) with three different coil setups. The centerline of the box denotes the median value, the extremes of the box the interquartile range and the bars the upper and lower limits that are not considered outliers. The plus represent outlying data (1.5 times the interquartile range beyond the 25th or 75th percentile). The mean of every particular data set is depicted as diamond. *** $p < 0.001$, ** $p < 0.01$, * $p < 0.05$, ns $p \geq 0.05$.

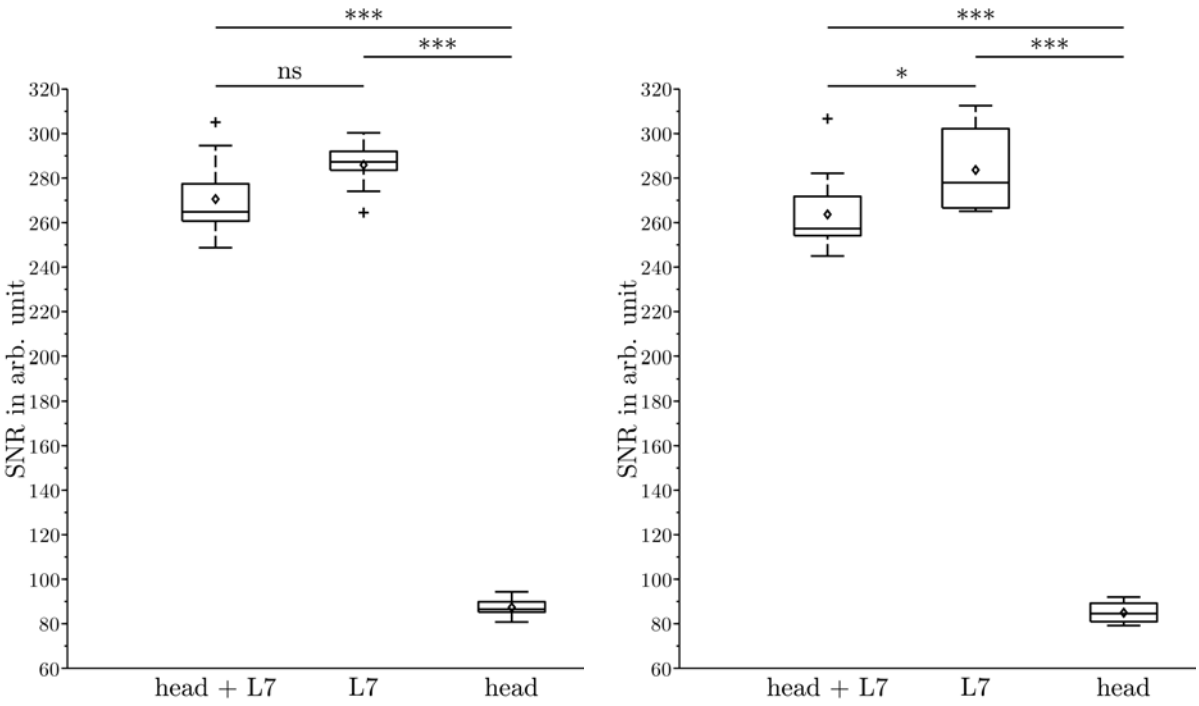

Figure 4.3: SNR box plots for the TrueFISP sequence transversal (a) and coronal (b) measured in phantoms (n = 10) with three different coil setups. The centerline of the box denotes the median value, the extremes of the box the interquartile range and the bars the upper and lower limits that are not considered outliers. The plus represent outlying data (1.5 times the interquartile range beyond the 25th or 75th percentile). The mean of every particular data set is depicted as diamond. *** $p < 0.001$, ** $p < 0.01$, * $p < 0.05$, ns $p \geq 0.05$.

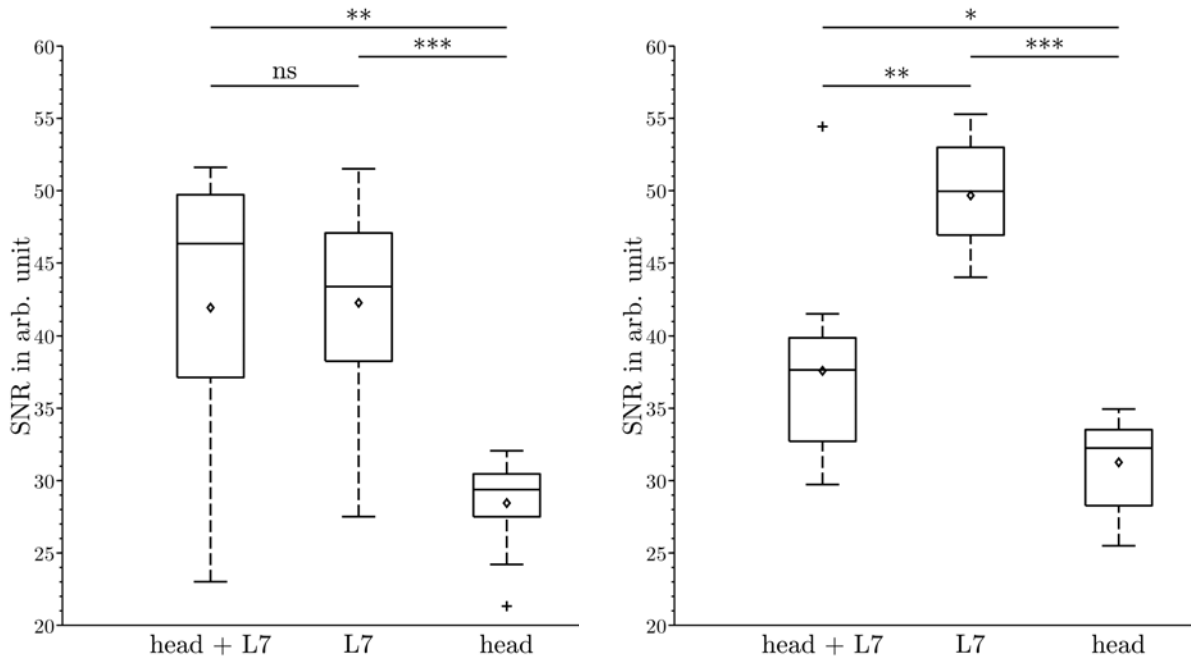

Figure 4.4: SNR box plots for the FLASH sequence transversal (a) and coronal (b) measured in test subjects (n = 11) with three different coil setups. The centerline of the box denotes the median value, the extremes of the box the interquartile range and the bars the upper and lower limits that are not considered outliers. The plus represent outlying data (1.5 times the interquartile range beyond the 25th or 75th percentile). The mean of every particular data set is depicted as diamond. *** $p < 0.001$, ** $p < 0.01$, * $p < 0.05$, ns $p \geq 0.05$.

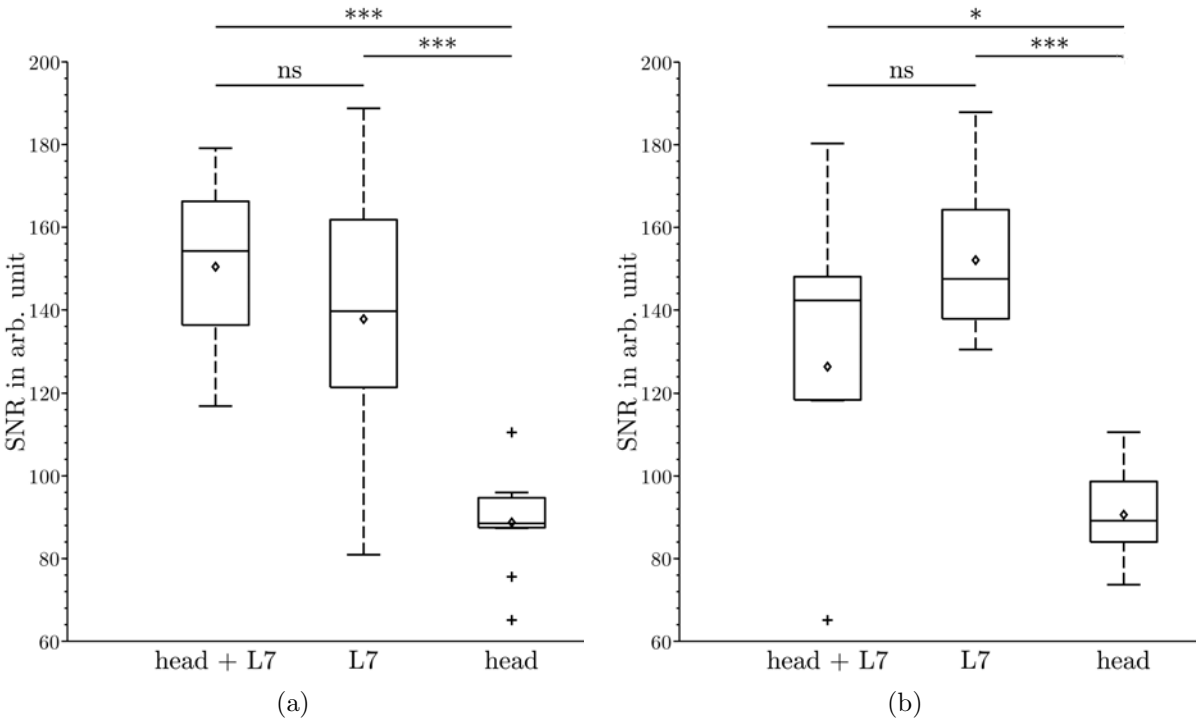

Figure 4.5: SNR box plots for the TrueFISP sequence transversal (a) and coronal (b) measured in test subjects (n = 11) with three different coil setups. The centerline of the box denotes the median value, the extremes of the box the interquartile range and the bars the upper and lower limits that are not considered outliers. The plus represent outlying data (1.5 times the interquartile range beyond the 25th or 75th percentile). The mean of every particular data set is depicted as diamond. *** $p < 0.001$, ** $p < 0.01$, * $p < 0.05$, ns $p \geq 0.05$.

Table 4.1: SNR mean values for FLASH and TrueFISP sequence measured in phantoms (n = 10) with three different coil setups. SNR enhancement is shown as comparison of the particular setup with the setup of the head coil alone.

Sequence	Orientation	Coil Setup	Mean SNR	Standard Deviation	SNR Enhancement
FLASH	transversal	head + L7	138.27	5.58	3.15
FLASH	transversal	L7	146.72	5.53	3.34
FLASH	transversal	head	43.88	1.44	1
FLASH	coronal	head + L7	135.1	12.64	3.01
FLASH	coronal	L7	143.84	15.03	3.2
FLASH	coronal	head	44.81	2.61	1
TrueFISP	transversal	head + L7	270.57	17.26	3.09
TrueFISP	transversal	L7	285.89	10.42	3.27
TrueFISP	transversal	head	87.34	3.85	1
TrueFISP	coronal	head + L7	263.68	18.58	3.1
TrueFISP	coronal	L7	283.62	18.5	3.33
TrueFISP	coronal	head	84.95	4.65	1

compared to the head coil alone are summarized in Table 4.2.

4.2 Optimizing Sequence Parameters

4.2.1 T_1 and T_2 Estimation of Melanoma

Due to unavailable T_1 and T_2 values for uveal melanoma in the literature, the values were estimated by using a T_1 weighted SE sequence and a T_2 weighted TSE sequence of the exact same region. Images originate from University Hospital Essen, Germany. Methodic details can be found in Section 3.3.1. A middle slice through the eye bulb including the melanoma (Figure 4.6) was used for estimation. Pixel values of several tissues including eye muscles, fatty tissue surrounding the eye, vitreous humor and melanoma were obtained by drawing the exact same regions of interest in both images. Plotting the obtained pixel values from T_1 and T_2 weighted images against each other resulted in Figure 4.7. The calculated means for every tissue are depicted with a red dot. It could be observed that the mean pixel value of uveal melanoma forms the middle of the line between vitreous humor and fatty tissue (Figure 4.7b). Tissue values found in Section 3.3.1 were used to simulate both SE and TSE sequence with the parameters found in Section 3.3.1. Results of simulations of eye muscles, fatty tissue surrounding the eye, vitreous humor are shown in Figure 4.8. This figure shows a similar triangular shape as seen in Figure 4.7. As mentioned before, the melanoma value lies exactly between vitreous humor and fatty

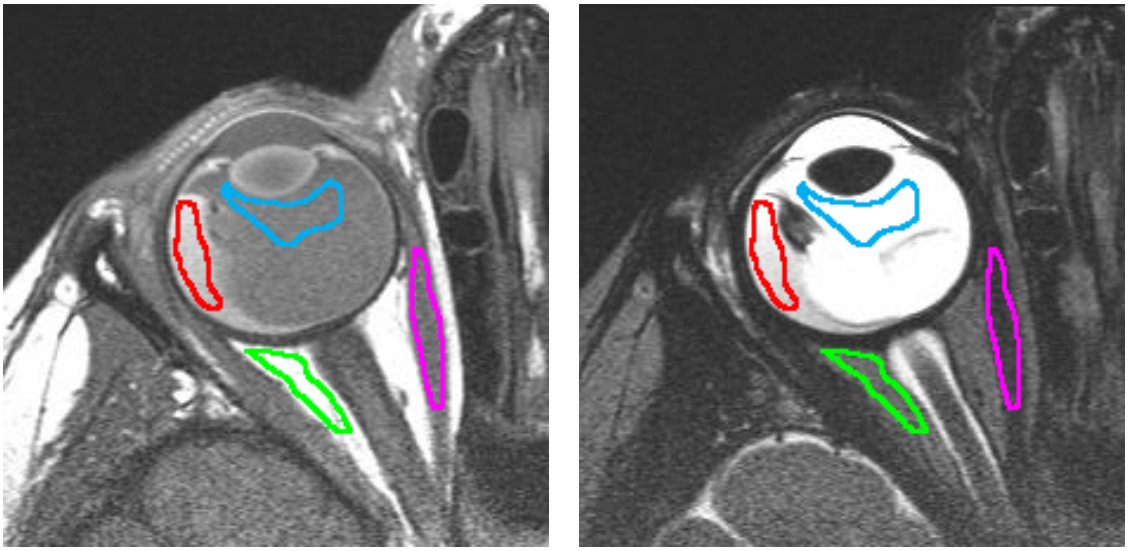

(a) T_1 weighted SE sequence (b) T_2 weighted TSE sequence

Figure 4.6: T_1 and T_2 weighted image of uveal melanoma (provided by the University Hospital Essen) used for relaxation time estimation of uveal melanoma. Regions of Interest (ROI) in tissues used for estimation are depicted in different colors. Red = uveal melanoma, blue = vitreous humor, green = fat and purple = eye muscle.

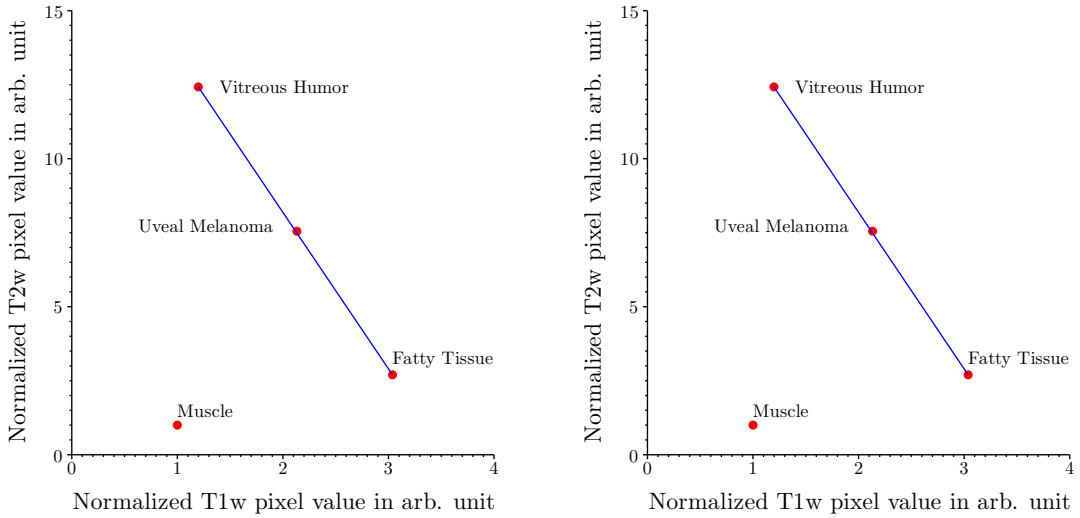

Figure 4.7: Plotting pixel values for T_1 weighted SE against T_2 weighted TSE sequence for different tissues obtaind from ROIs in images 4.6a and 4.6b results in chart (a). Plotting the mean values normalized by the value for muscle of every particular tissues, shows that the uveal melanoma lies exactly in the middle of the line formed between fatty tissue and vitreous humor (b).

Table 4.2: SNR mean values for FLASH and TrueFISP sequence measured in test subjects (n = 11) with three different coil setups. SNR enhancement is shown as comparison of the particular setup with the setup of the head coil alone.

Sequence	Orientation	Coil Setup	Mean SNR	Standard Deviation	SNR Enhancement
FLASH	transversal	head + L7	41.91	9.72	1.47
FLASH	transversal	L7	42.24	6.82	1.48
FLASH	transversal	head	28.44	3.15	1
FLASH	coronal	head + L7	37.58	7.14	1.24
FLASH	coronal	L7	48.24	5.83	1.59
FLASH	coronal	head	30.19	4.68	1
TrueFISP	transversal	head + L7	150.42	19.63	1.69
TrueFISP	transversal	L7	137.78	33.08	1.55
TrueFISP	transversal	head	88.74	11.49	1
TrueFISP	coronal	head + L7	126.43	41.04	1.39
TrueFISP	coronal	L7	152.06	17.31	1.67
TrueFISP	coronal	head	90.61	10.43	1

tissue. This fact was used to determine the T_1 and T_2 combination resulting in a signal value comparable to the midpoint of these two tissues. Signal values for a variety of T_1 and T_2 combinations were simulated. The combination in which the resulting signal value is closest to the midpoint yielded

$$T_1 = 992\,\text{ms}$$
$$T_2 = 164\,\text{ms}.$$

4.2.2 Theoretical Sequence Optimization

4.2.2.1 TurboFLASH

The relaxation values for different tissues including vitreous humor, muscle, fatty tissue and melanoma where simulated for different sequence parameter settings. The resulting signal values for every particular tissue were plotted against the sequence parameter varied for a specific range (Figure 4.10). Changing the flip angle β from 1° to 90° led to the graph shown in Figure 4.10a. For all tissues a maximum signal value could be observed for a flip angle between 11° to 13°. By varying TE from 1 ms to 100 ms (Figure 4.10b) it was seen that the signal for melanoma only dropped minimally over the range of the echo time variation. For all tissues the highest signal values could be seen with very short echo times. Also the best signal contrast between tissues could be detected at relatively low echo times ranging from 0 ms to 30 ms. With higher echo times the signal for fatty tissues converged to the signal level observed for melanoma. At about 40 ms the signal

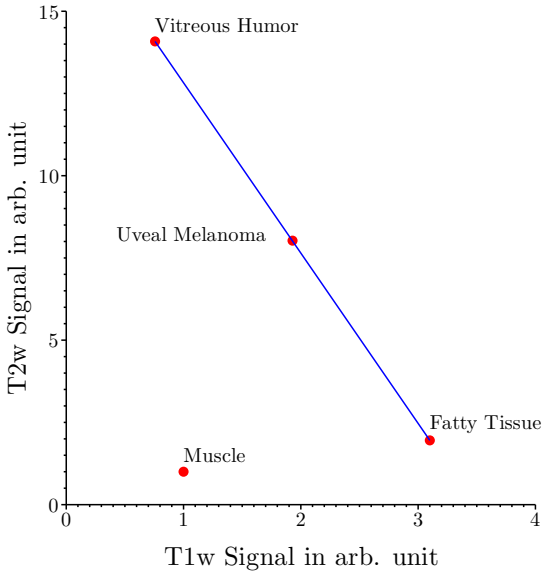

Figure 4.8: Simulated signal values for T_1 weighted SE against T_2 weighted TSE sequence for different tissues including the uveal melanoma which was simulated with $T_1 = 1092\,\text{ms}$ $T_2 = 165\,\text{ms}$ in order to be exactly in the middle of the line formed by vitreous humor and fatty tissue.

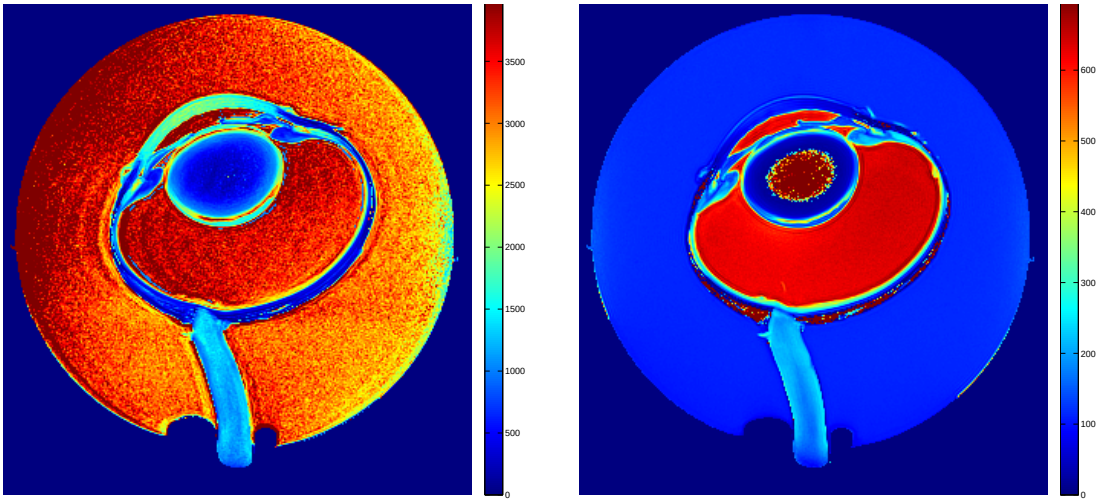

(a) T_1 map (b) T_2 map

Figure 4.9: Color maps of a cow eye showing the different T_1 (a) and T_2 (b) values of eye tissues in ms. Images were acquired using a multi echo spin echo (T_2) and an inversion recovery sequence (T_1).

for muscle dropped below the signal observed for vitreous humor. The time between the excitation pulse and the first low angle shot TI_1 was modified from 1 ms to 500 ms, signal values for all tissues showed slight increase for longer TI_1 values (Figure 4.10c). The ratio between signals of different tissues did stay almost constant over the whole range. TI_2, the time between subsequent low angle excitation pulses, was differed in a range of 1 ms to 100 ms. It showed increasing signal values for all tissues with rising TI_2 (Figure 4.10d).

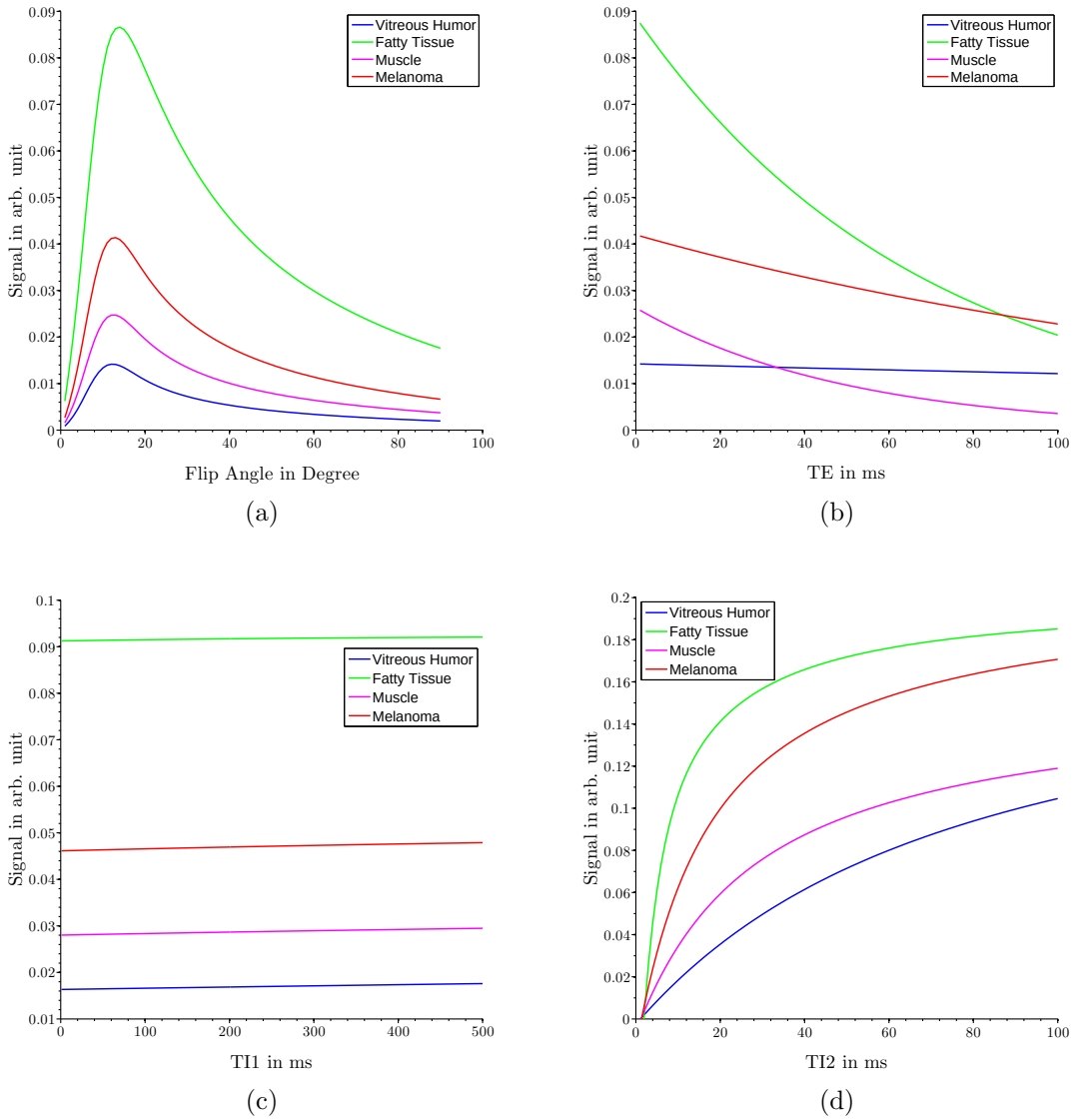

Figure 4.10: The TurboFLASH sequence was simulated for different tissues including vitreous humor, muscle, fatty tissue and melanoma. Different sequence parameters were altered to find the optimal value. The flip angle β was varied from 1° to 90° (a), TE was altered from 1 ms to 100 ms (b), TI_1 was modified from 1 ms to 500 ms (c) and TI_2 differed in a range of 1 ms to 100 ms (d).

4.2.2.2 Turbo Spin Echo

For the TSE sequence, relaxation values of different tissues including vitreous humor, muscle, fatty tissue and melanoma were simulated with different sequence parameter settings. The resulting signal values for every particular tissue were plotted against the sequence parameter varied for a specific range (Figure 4.11). By varying the refocusing flip angle an increase in contrast between all simulated tissues could be observed with enlarging flip angle (Figure 4.11a). Especially the signal values for vitreous humor and the melanoma diverged with increasing refocusing flip angle. Signal values for all four tissues showed similar results for short TE and started to separate at about 20 ms (Figure 4.11b). Melanoma and vitreous humor showed the same signal values for TE of about 35 ms and started diverging from there on. Muscle and fatty tissue showed decreasing signals with rising TE. By varying TR up to 10 000 ms for all tissues except for vitreous humor a plateau was observed. Fatty tissue and muscle exhibited relatively low signal values of about 0.16 and 0.08, respectively over the course of varying TR. Vitreous humor and melanoma displayed a similar signal value for a TR of 3100 ms and started growing apart from there. The biggest contrast between vitreous humor and melanoma in the simulated range for TR was observed at 10 000 ms.

4.2.2.3 SPACE

Pork belly was used as a phantom to represent fatty tissue and muscle, for vitreous humor a bottle of distilled water was chosen. ROIs were placed in homogeneous regions of fatty tissue and muscle tissue of the pork belly for images obtained with SE and TSE sequences. To represent vitreous humor a ROI in the middle of the water bottle was used. Plotting the obtained mean pixel values from T_1 and T_2 weighted images, normalized to muscle tissue, against each other results in Figure 4.12. The same phantom setup was used to vary TR and TE for the space sequence described in Section 3.3.2.3. Plotting the mean pixel values of ROIs placed in the particular tissues against TR and TE leads to Figure 4.13a and 4.13b, respectively. With variable TR for water a plateau could be observed starting at a TR value of about 3000 ms. Muscle tissue reached a similar signal plateau at about 4500 ms. Water on the other hand was observed to have increasing pixel values with longer TR and never reached a maximum within the tested range. Very similar signal values for all three tissues could be obtained for a TR of about 3000 ms. A very good contrast between all tissues was shown between about 500 ms and 2000 ms. By modifying TE all tissues besides water showed decreasing pixel vales with longer TE times. Water showed almost constant pixel values throughout the whole range tested. The biggest contrast between all three tissues could be observed with relatively short TE values between 5 ms and 30 ms.

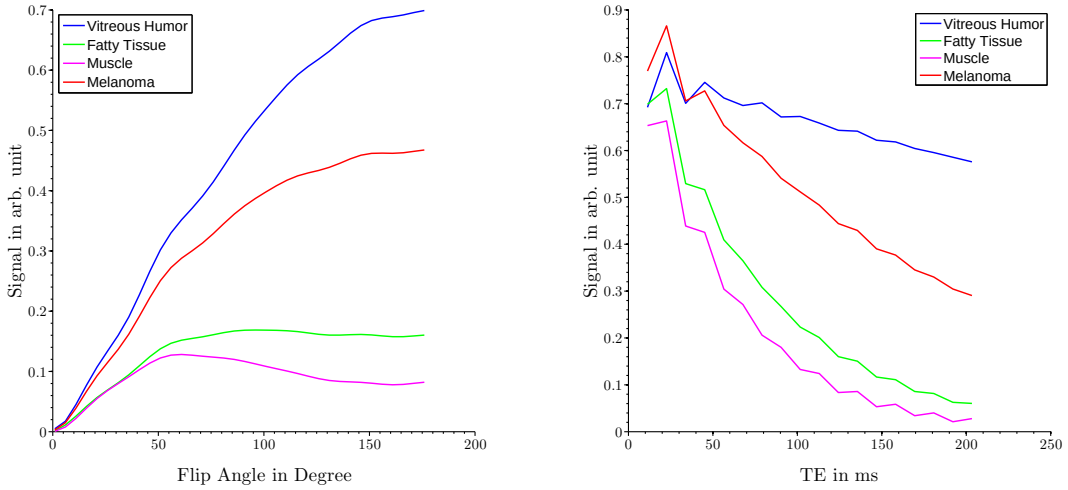

(a)

(b)

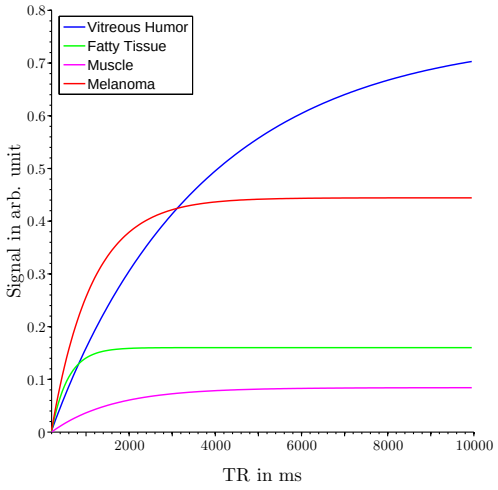

(c)

Figure 4.11: The TSE sequence was simulated for different tissues including vitreous humor, muscle, fatty tissue and melanoma. Different sequence parameters were altered to find the optimal value. The refocusing flip angle varied from 1° to 180° (a), TE was altered up to 200 ms (b), and TR was modified up to 10 000 ms (c).

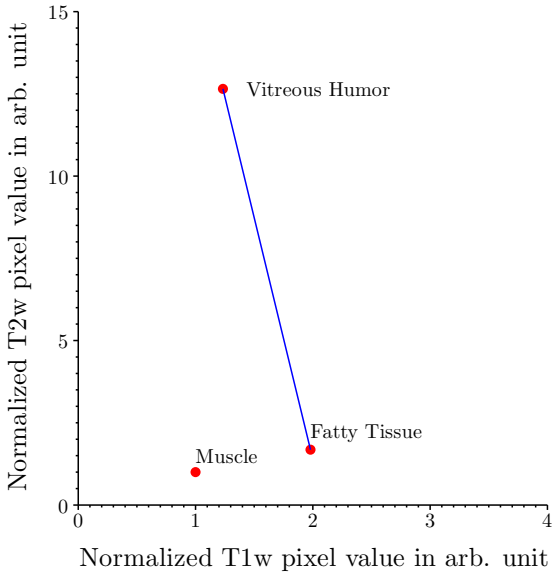

Figure 4.12: Plotting pixel values for T_1 weighted SE against T_2 weighted TSE sequence of different tissues obtained from a measurement where pork belly (for muscle and fatty tissue) and destilled water (for vitreous humor) were used as a phantom. Mean values of placed ROIs are plotted normalized by the value for muscle of each particular tissue.

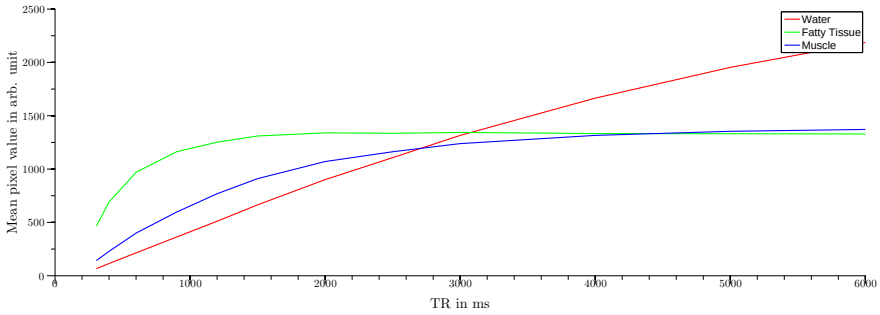

(a)

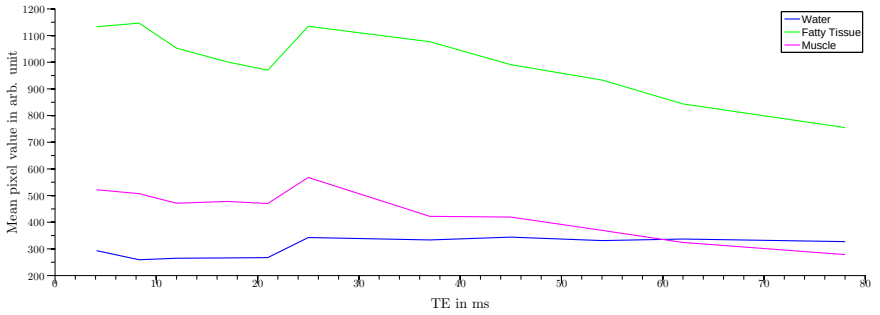

(b)

Figure 4.13: Optimization of the SPACE sequence using pork belly (for muscle and fatty tissue) and a bottle of distilled water (for vitreous humor) as a phantom. Mean pixel values from ROIs, placed in the respective tissue are plotted against TR (a) and TE (b). The TR was varied from 306 ms to 6000 ms with a TE set to 12 ms. TE was modified in a range of 4.1 ms to 78 ms with a TR set to 700 ms.

4.2.3 Practical Optimization

4.2.3.1 Implemented Sequence Parameters

TurboFLASH The optimized TFL sequence was implemented as a 3D sequence with the following parameters: TR = 326 ms, TE = 3.1 ms, TI = 180 ms, FOV = 170 mm, matrix = 256, NEX = 2, slice thickness = 1.25 mm, flip angle = 12°, bandwidth = 270 Hz/pixel, echo spacing = 7.1 ms, turbofactor = 40, acquisition time = 5:35 min and a resulting voxel size of 0.66 x 0.66 x 1.25 mm. A phase oversampling of 100% was used.

Turbo Spin Echo The practical implementation of the optimized TSE sequence was operated with the following parameters: TR = 7000 ms, TE = 124 ms, FOV = 180 mm, matrix = 320, NEX = 2, slice thickness = 1 mm, flip angle = 135°, bandwidth = 260 Hz/pixel, turbofactor = 18, echo spacing = 11.3 ms, acquisition time = 4:56 min and a resulting voxel size of 0.56 x 0.56 x 1 mm. A phase oversampling of 24% was used. The TSE sequence was implemented as a 2D sequence with 31 slices.

SPACE The optimized SPACE sequence was implemented as a 3D sequence with the following parameters: TR = 700 ms, TE = 12 ms, FOV = 190 mm, matrix = 256, NEX = 1, slice thickness = 1 mm, bandwidth = 630 Hz/pixel, turbofactor = 38, echo spacing = 4.13 ms, acquisition time = 5:35 min and a resulting voxel size of 0.74 x 0.74 x 1 mm. A slice oversampling of 80% and two saturation slabs were used. The flip angle mode was set to T_1 variable and the T_1 and T_2 for the organ under examination were set to the relaxation values estimated in Section 4.2.1.

4.2.3.2 Images of Implemented Sequences at the University Hospital Graz

Images of different patients using the current 3D FLASH sequence (Figure 4.14), the optimized TurboFLASH sequence (Figure 4.15) and the optimized Turbo Spin Echo sequence (Figure 4.16). All images were acquired in the absence of the medEyeTrack. Images in Figure 4.14a and Figure 4.16a, Figure 4.15a and Figure 4.16b, Figure 4.15b and Figure 4.16c as well as Figure 4.14b and Figure 4.15b originate from the same patient, respectively. The patient in Figure 4.15c and Figure 4.16c did not suffer an ocular tumor.

4.3 Triggering of an MR Sequence Using the medEyeTrack System

4.3.1 Qualitative Image Analysis

Every test subject was imaged six times with identical MR pulse sequences described in Section 3.5.2. Subjects were asked to perform a different eye movement scheme (total of 6)

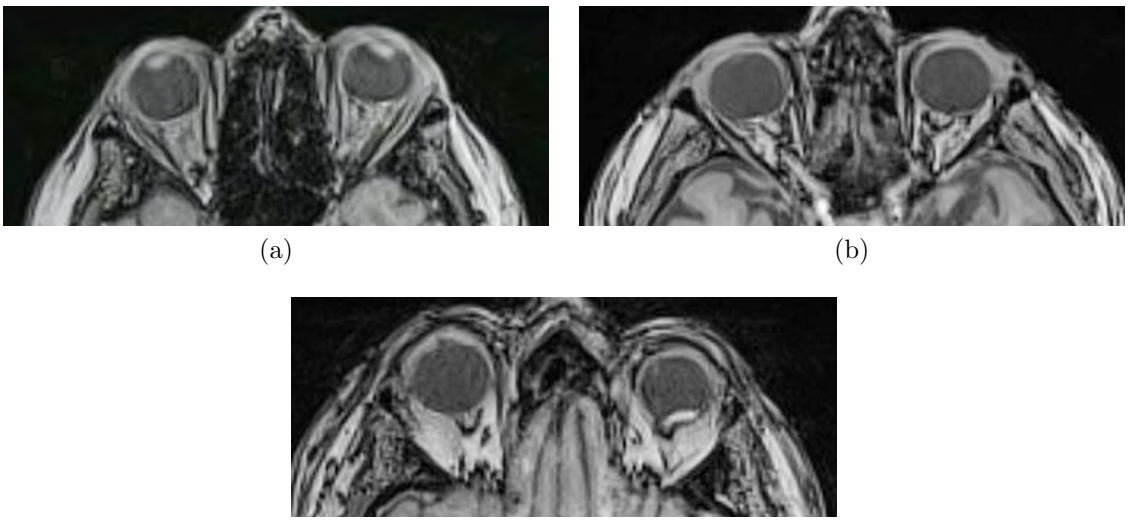

(a) (b)

(c)

Figure 4.14: Images acquired at the University Hospital Graz with the currently used 3D FLASH sequence without administered contrast agent. Depicting three different patients with uveal melanoma.

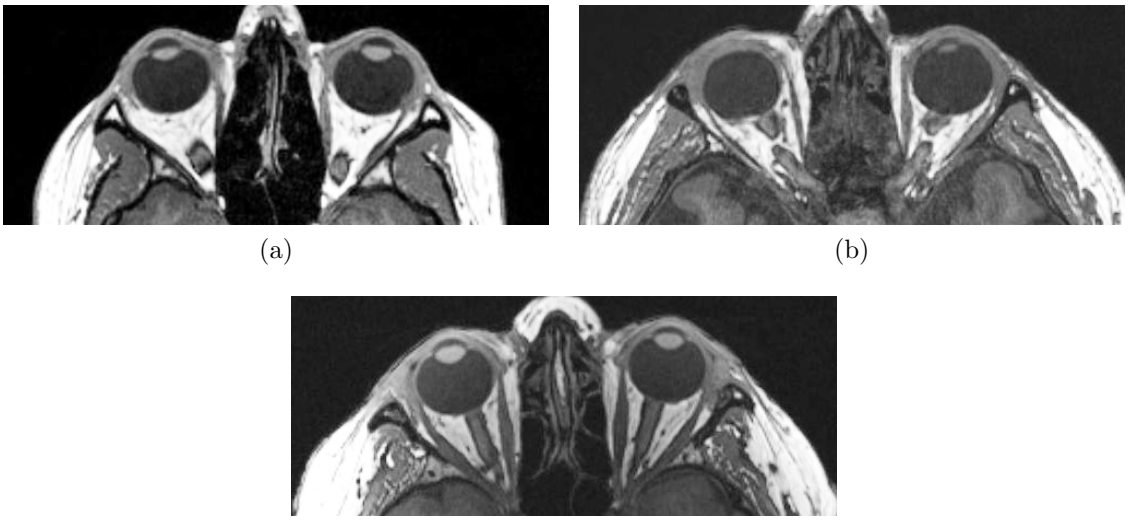

(a) (b)

(c)

Figure 4.15: Images acquired at the University Hospital Graz with the optimized TurboFLASH sequence. Depicting three different patients, two with uveal melanoma (a and b).

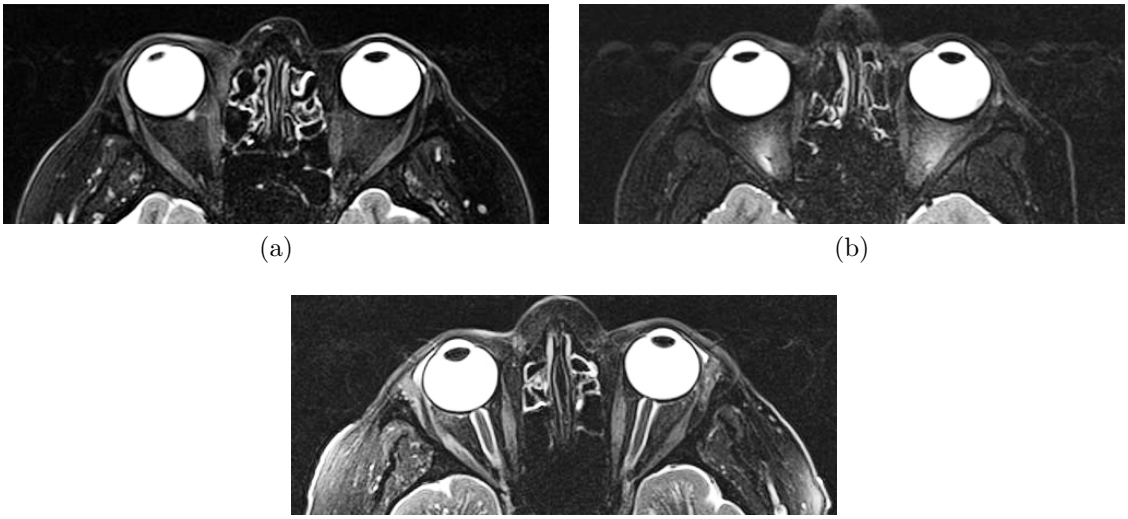

(a) (b)

(c)

Figure 4.16: Images acquired at the University Hospital Graz with the optimized Turbo Spin Echo sequence. Depicting three different patients, two with uveal melanoma (a and b).

for every measurement, including closing the eyes and trying not to move them, fixating the LED during the whole measurement, averting the gaze away from the LED every 10 seconds, triggered and untriggered, and averting the gaze away every 20 seconds, triggered and untriggered. For all subjects, triggering the 10 second movement scheme resulted in substantial decrease of motion artifacts in and around the bulb (Figure 4.17). The triggered image showed a much cleaner image of the eye. Especially in the anterior region around the pupils the fine structures were more recognizable. The 20 second untriggered movement scheme led to less overall artifacts compared to the 10 second untriggered scheme and triggering resulted in a slight reduction of artifacts in most subjects (Figure 4.18b). Improvements of the images were mostly found in the anterior region of the eye and outside the eye in phase encoding direction. The outcome of keeping the eyes closed in comparison to the LED fixation scheme was observed to be slightly poorer (Figure 4.19). By closing the eyes more motion artifacts were induced in the majority of test subjects. These artifacts were mainly located in the anterior region. In some subjects also the loss of control over the eye movement was observed. This led to differences in the orientation of the optic axis of the eyes, for example to a rotation of the bulb (Figure 4.20).

Images acquired from 6 test subjects with all 6 different movement schemes (36 images in total) were qualitatively analyzed by 7 experts. Images were shown in random order and evaluators were blinded to the test subjects' identity as well as to the eye movement scheme used for the given picture. The analysis was performed via a grading system (see Section 3.5.4.1) for three different criteria including overall image quality, anatomical recognizability and amount of artifacts present in the image. For visualization of the outcome of this expert evaluation the data for every criteria was used to calculate the rank

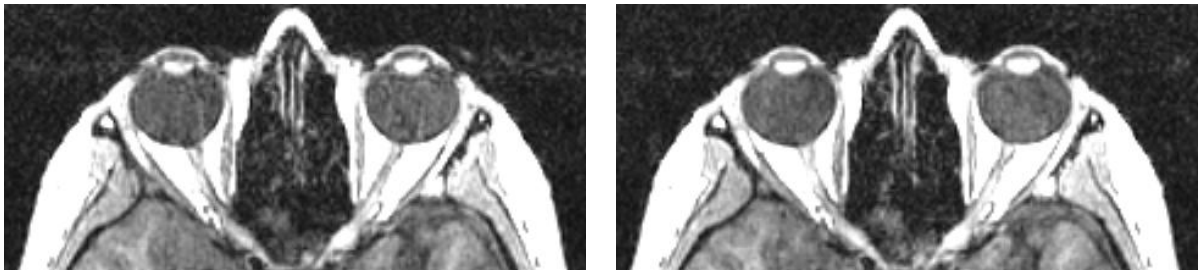

(a) not triggered 10 s (b) triggered 10 s

Figure 4.17: Images show a transversal slice right in the middle of eyes from a test subject imaged with the 10 second movement scheme. Motion artifacts were drastically reduced for both eyes by triggering (b) compared with the same sequence not triggered (a). A window setting to show motion artifacts best was used.

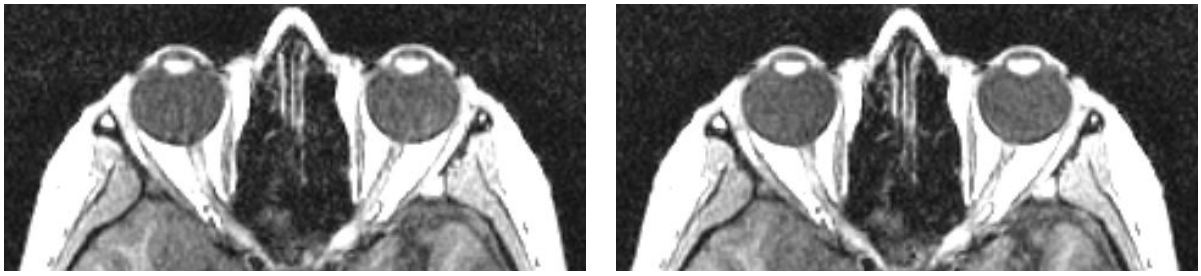

(a) not triggered 20 s (b) triggered 20 s

Figure 4.18: Images show a transversal slice right in the middle of eyes from a test subject imaged with the 20 second movement scheme. Motion artifacts were reduced for both eyes by triggering (b) compared with the same sequence not triggered (a). A window setting to show motion artifacts best was used.

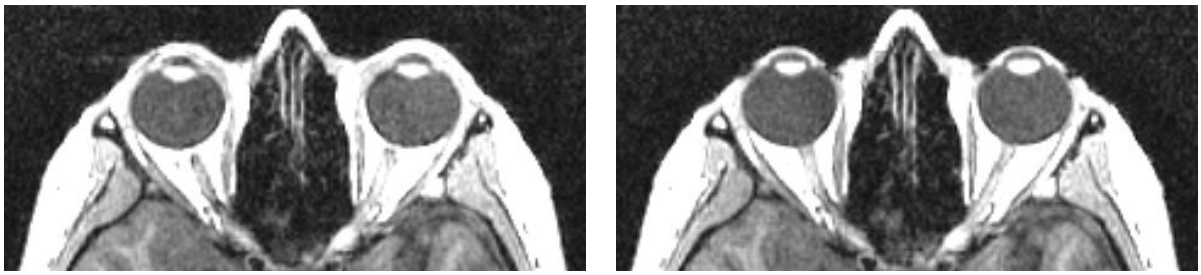

(a) Eyes closed (b) Eyes fixate LED

Figure 4.19: Images show a transversal slice right in the middle of eyes from a test subject. Motion artifacts were slightly reduced when the subject fixates the LED (b) compared to when eyes are just held close (a). This effect can be seen particularly at the left eye. A window setting to show motion artifacts best was used.

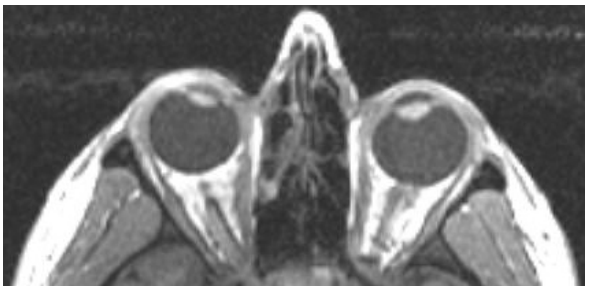

Figure 4.20: Image shows a transversal slice right in the middle of eyes from a test subject. Differences in the orientation of the optic axis, as seen here as an inward rotation, could be observed during closed eye scheme.

sum for every movement scheme (Figure 4.21). The rank sum for schemes was calculated using MATLAB and the function *tiedrank*, which automatically adjusts for ties. For this evaluation a high rank sum value represents poor grading and a low value good grading. The overall image quality (Figure 4.21a) was evaluated to be the best for eyes fixating the blinking LED, followed by the eyes closed. No significant difference was detected between these two groups ($p = 0.1344$). The 10 second and 20 second untriggered movement schemes showed the poorest results. Triggering these two movement schemes led to significant improvements in judged overall image qualities ($p < 0.0001$ and $p = 0.0326$, respectively). Anatomical recognizability (Figure 4.21b) was rated to be worst for the movement schemes where the gaze was averted away from the LED every 10 seconds or 20 seconds. Triggering these movement schemes significantly enlarged the possibility to recognize the anatomy of and within the bulb ($p < 0.0001$ and $p = 0.0281$, respectively). Classifying the LED fixation scheme compared to the eyes closed scheme yielded a significantly better result ($p = 0.0003$). Artifacts in the images could be dramatically reduced by triggering the 10 and 20 second movement scheme ($p < 0.0001$ and $p = 0.0203$, respectively) (Figure 4.21c). Fixating the blinking LED was assessed to have the least amount of artifacts in the image, and was rated significantly better than keeping the eyes closed ($p = 0.0039$).

4.3.2 Quantitative Image Analysis

In Figure 4.22 the normalized gradient entropy values F for different eye movement schemes are visualized. For every test person the different gradient entropy values were normalized by their value for the LED fixation scheme. It could be shown that closing the eyes resulted in higher gradient entropy values than fixating the LED. Triggering the 10 second eye movement scheme led to a lower F value compared to the not triggered scheme. In contrast, triggering the 20 second movement scheme did not have any effect on the gradient entropy values. By assessing the data statistically no significant difference between triggered and untriggered images of the 20 second movement schemes could be

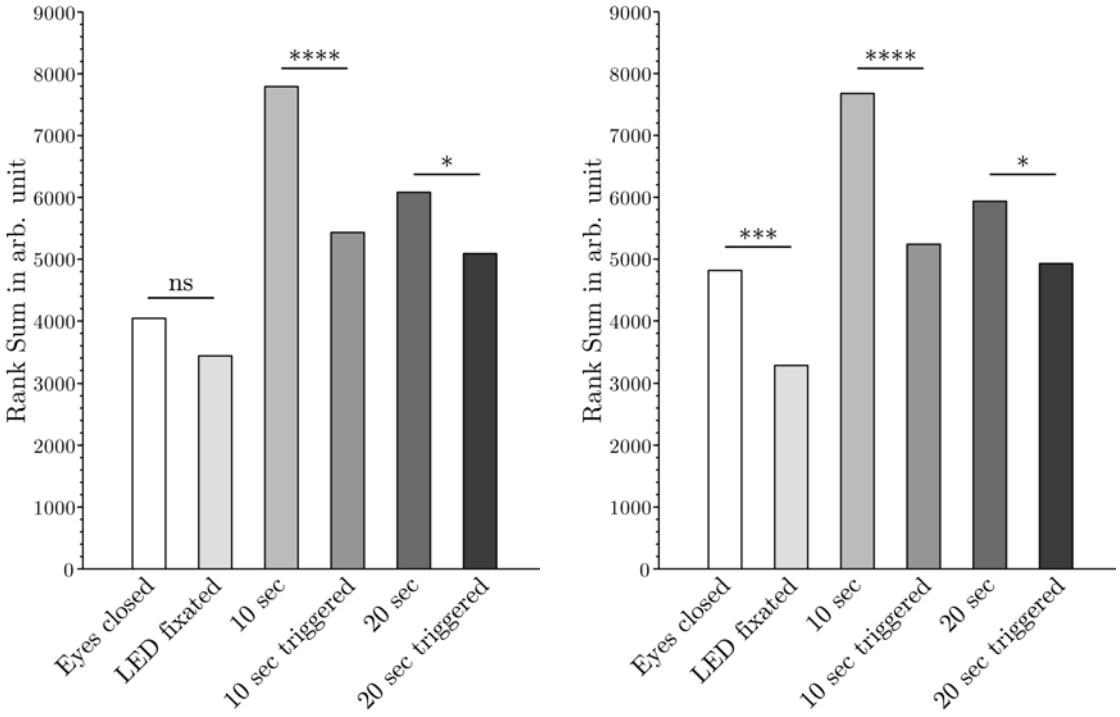

(a) Overall Image Quality

(b) Anatomical Recognizablitiy

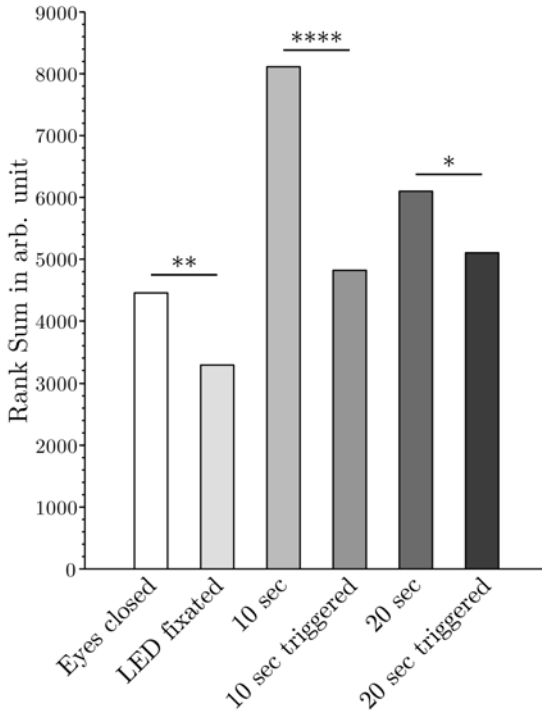

(c) Artifacts

Figure 4.21: Qualitative image analysis performed by 7 experts (different fields of expertise). Images acquired from 6 test subjects with all 6 different movement schemes, were evaluated via a grading system for three different criteria including overall image quality (a), anatomical recognizability (b) and amount of artifacts present in the image (c). A higher rank sum value represents poorer grading. Evaluators where blinded to the test subjects' identity as well as the eye movement scheme used and images where shown in random order. **** $p < 0.0001$, *** $p < 0.001$, ** $p < 0.01$, * $p < 0.05$, ns $p \geq 0.05$.

found (p = 0.2236). Furthermore no statistically significant difference was observed when comparing the data for eyes closed and eyes fixated on the LED (p = 0.0782). However comparing the untriggered and triggered images for the 10 second movement schemes showed a significant discrepancy in favor of the triggered scheme (p = 0.029).

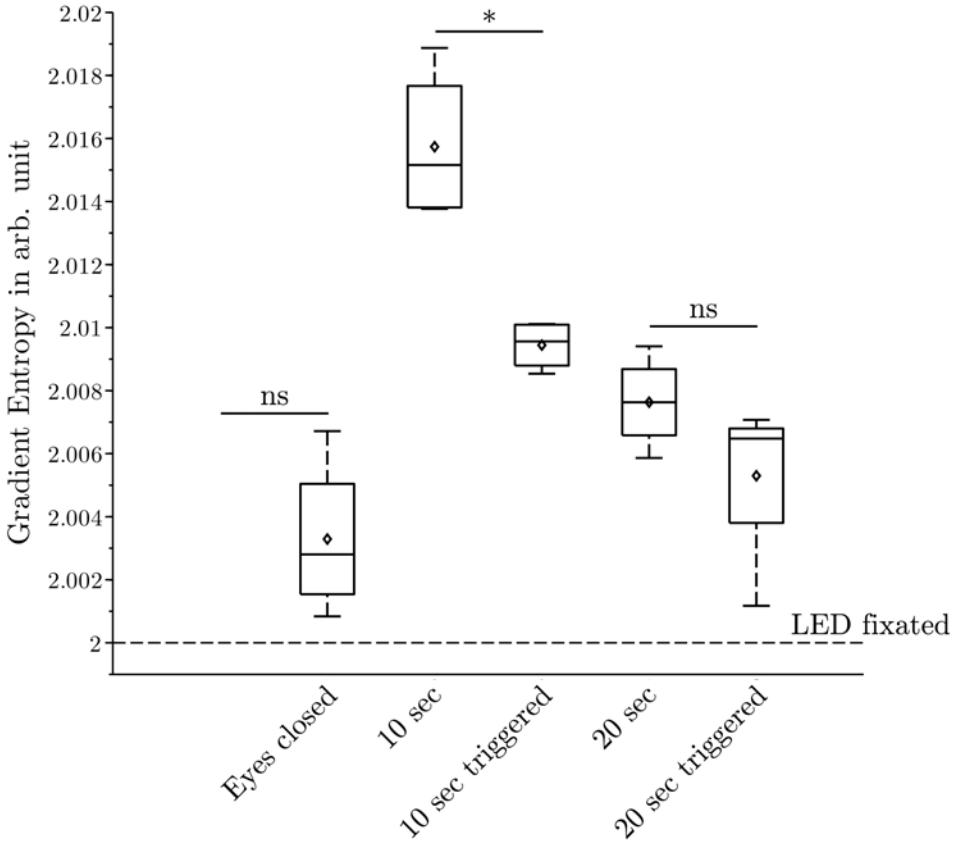

Figure 4.22: Gradient entropy values for different eye movement schemes. Values were plotted normalized to the LED fixation scheme (depicted by the dashed line). A higher gradient entropy value represents a higher amount of motion artifacts in the image. Median values are indicated by the line within the box plot. The centerline of the box denotes the median value, the extremes of the box the interquartile range and the bars the upper and lower limits that are not considered outliers. Outlying data would be represented with a plus (1.5 times the interquartile range beyond the 25th or 75th percentile). The mean of every particular data set is depicted as diamond. *** p <0.001, ** p <0.01, * p <0.05, ns p $\geq$ 0.05.

Chapter 5

Discussion

5.1 Signal to Noise Ratio Measurements of Different Coil Settings

In an MR image the ratio of signal intensity to noise level is called the signal to noise ratio (SNR). In order for an MR image to be diagnostically useful, a very important aspect of image optimization is to provide a high enough SNR level. Images with low SNR will appear fuzzy and make it very easy to miss small anatomical details [21]. Especially in ocular imaging, where structures are very small, this plays an extensive role in order to provide useful and reliable images for patient treatment. For obtaining adequate SNR levels in orbital MRI imaging, the choice of an appropriate coil is of major importance. The head coil usually provides insufficient SNR values for the necessary resolution of the orbital region. Therefore, the literature suggests that ophthalmological MRI should be performed with small surface coils, which were already intensively studied in orbital and ocular lesion imaging publications, throughout all field strengths, over the past years [28, 30, 32, 34, 38, 40–44]. The higher signal level achieved through application of small surface coils can not only be invested in better image quality or higher SNR. By keeping the image quality and SNR level approximately constant, faster acquisition times can be achieved. This is of great interest as motion artifacts due to eye movement pose a major problem in ophthalmological MRI. The most important source of motion artifacts are voluntary eye movements and blinking. As discussed by Fanea and Fagan [19] the average time between blinks is 2.8 s in men and approximately 4 s in women, with a duration of 0.3 s to 0.4 s [90]. By achieving faster acquisition times motion artifacts in ophthalmological MRI images can be drastically reduced.

In this thesis the SNR advantage of a Siemens 3 T Loop 7 cm surface coil compared to the standard head coil Siemens Head/Neck 20 A 3 T Tim Coil was analyzed. The results show that the achievable SNR with the small L7 surface coil strongly depends on the distance to the coil (Figure 4.1). Depending on the head shape and size the surface

coil can be placed fairly close to the eye and the resulting distance from the coil to he bulb is only several millimeters. The schematic picture of the eye depicted in Figure 4.1 is shown in an average distance from the surface coil and is represented in proportional size. Depending on the structure of interest within the bulb a SNR enhancement of 4 to 4.5 fold for anterior and almost 2 fold for posterior regions compared to the standard head coil could be observed. Taking the relationship of SNR and the number of averages into account ($SNR \propto \sqrt{averages}$) the 2 fold gain in SNR within the bulb could result in a scan time reduction of factor 4 at minimum. Phantom measurements where a ROI in similar size to the eye was drawn in a distance of about 5 mm to the surface coil (Figure 4.2 and 4.3) showed significant increase in SNR values compared to the standard head coil. Additionally it was shown that the combination of the standard head coil and the small surface coil showed in most cases a significantly poorer SNR outcome compared to the L7 surface coil alone. This indicates that the two coils are not perfectly matched and are not optimized for combined operation. The substantially higher standard deviation of the mean when using the L7 coil compared to the head coil is related to strong SNR distance dependency of the surface coil. A slightly different placed ROI can have a significant impact on the mean SNR within the ROI and therefore lead to a higher standard deviation over the 10 phantom measurements.

Similar results were observed in the test subject study including 11 voluntary subjects. Using the small surface coil yielded significant SNR enhancement compared to the standard head coil. The ROIs for SNR analysis were placed in the vitreous humor in a manner that maximizes the area of the ROI while targeting mainly a homogeneous region that is not affected by artifacts. Achieved mean SNR values with the L7 coil in the in vivo study were observed to be significantly higher than those from the head coil, but lower compared to the phantom measurements. Nevertheless, SNR enhancement found in this in vivo study still allows an acquisition time reduction by the factor 2 while keeping the same image overall quality. Also in this experiment higher standard deviations of the means could be observed for the measurements including the L7 coil. This effect was especially noticeable with the TrueFISP sequence and can be interpreted by the above explained distance dependency of SNR values. The application of the L7 coil can be quite challenging. Depending on the subjects head form and size the surface coil has slightly a different position related to the eye resulting in deviating SNR values. In the in vivo setup in contrast to the phantom measurements no significant difference of the surface coil and the combination of surface coil and head coil could be observed. Both sequences used for SNR measurements (FLASH and TrueFISP) showed similar SNR enhancement with the different coil setups. For the statistical evaluation of the FLASH sequence in the coronal plane the number of subjects was reduced from 11 to 10 because one subject was not analyzable due to a major artifact in the orbital region. For all other setups it was possible to conduct the evaluation with all 11 test subjects.

By calculating the SNR as described in Equation 3.2 it is assumed that the noise within the ROI in the difference image is Gaussian distributed. This assumption is only valid if the mean signal value is sufficiently larger than the standard deviation of the noise. Therefore, the ROI must be positioned in tissue with sufficiently high SNR (and not in the image background). If this is not the case, more complicated distributions, such as the Rician or noncentral chi distribution, have to be used [91]. In this study the assumption of Gaussian distribution was fulfilled because ROIs were placed only in the vitreous humor, which showed very high signal values. The approach to calculate the SNR with Equation 3.2 also assumes that the second image is acquired under precisely the same conditions as the first image. This assumption was taken care of by setting the number of measurements of every sequence to 10 in order to make sure a steady state was given and that the a minimum amount of time between subsequent images elapsed. This approach also guarantees that no system adjustment or calibration is performed between scans. Since this way of calculating the standard deviation involves a difference operation between two images, the image noise measurement must be corrected by a division by $\sqrt{2}$. When calculating the difference image directly on the Siemens MR scanner software (Evaluate/Dynamic Analysis/Subtract) one has to be particular careful because if "Auto Scale" is not enabled for the subtraction all negative values in the resulting image will be set to 0. This will of course alter the standard deviation in the resulting difference image and yield false SNR values. Especially for SNR measurements in ophthalmological MRI it is very important to use very fast sequences, as employed in this study, to keep motion artifacts to a minimum. Motion artifacts will not only lead to wrong signal values, but can also be very variable between two subsequently acquired images. This will highly influence the calculation of the standard deviation in the difference image and therefore make the SNR calculation unfeasible.

Erb-Eigner et al. [40] concluded in their study that small surface coils yield a higher SNR only in the anterior region of the eye and that ocular imaging at 3 T with only the head coil also yields acceptable results. They implied that for reasons of easier usage and manageability the head coil should be favored in clinical everyday use over the surface coil. However, this present study showed significantly better SNR when using the L7 coil compared to the head coil. This major increase in SNR can be invested in higher resolution or reducing the scan time with the factor of two. In ophthalmological MR imaging both these factors play a major role and therefore the usage of small surface coils is strongly recommended. Nevertheless, we highly agree with Erb-Eigner et al. that the handling and manageability of the head coil is a lot easier and more practical in everyday clinical use. Especially with the very rigid surface coil from Siemens it is not a simple task to fixate the coil on to the subjects' head in a manner that provides an acceptable prevention from slippage or displacement. Slippage of the surface coil during a measurement as well as between measurements must absolutely be avoided. Even minimal displacement changes

the local illumination of the underlying anatomy and drastically reduces SNR values in the not illuminated regions. The Siemens L7 surface coil might not be the perfect coil for the use in ophthalmological MRI but there are more flexible and suitable alternatives on the market that are specially developed for this use case and are much easier to handle.

5.2 Optimizing Sequence Parameters

For the development of new MRI methodology and the adaptation of existing MRI sequences for specific applications, the following procedure is frequently used. Existing and newly developed MRI protocols are investigated in a first step with mathematical simulations in order to theoretically optimize measurement parameters for the given applications. Subsequently, a practical implementation on an MR scanner takes place and the optimized sequences are carefully evaluated and improved on appropriate MR phantoms. Finally, the development work is concluded with in vivo tests and optimization in test subjects. Thereafter, study protocols are developed, which are used in specific test studies before the new techniques are provided for use in scientific and medical research projects. For the development of new methods, it is occasionally necessary to collect normal values for specific structures and to determine the measurement and physiological reproducibility of measurement parameters in targeted small studies. The main priority in this study was to optimize sequences especially for ophthalmological MR imaging including uveal melanoma and to maximize the contrast between uveal melanoma and the vitreous humor to simplify visual detectability in clinical daily routine.

5.2.1 T_1 and T_2 Estimation of Melanoma

At present there are no available T_1 and T_2 relaxation times for uveal melanoma in the literature. Yet, in oder to conduct theoretical simulations to optimize measurement parameters these values are indispensable. This study presents an estimation of T_1 and T_2 relaxation values using two differently weighted MR images (T_{1w} and T_{2w}) of the exact same anatomical region. Pixel values of these images were used to establish relationships between several tissues (muscle, fatty tissue, vitreous humor and melanoma). Sequences used for acquisition of the differently weighted MR images were simulated with the identical measurement parameters. These simulations yielded similar tissue relationships as obtained from the actual images. Using these relationships to estimate relaxation values for uveal melanoma yielded T_1 and T_2 values between fatty tissue and vitreous humor. This was expected due to its intermediate signal intensity between those two tissues in the T_{1w} as well as the T_{2w} images. Due to the fact that resulting pixel values in the image are not only dependent on relaxation times but also strongly depend on proton density of the imaged tissue [92, 93] an estimation of T_1 and T_2 relaxation simply based on the

brightness values in an image is not recommended. Half the signal intensity in an T_{1w} or T_{2w} image does not necessarily imply half the T_1 or T_2 relaxation time, respectively. The estimation used in this publication takes the proton density as well as relaxation times for all the tissues used into account and therefore gives a good first indication of where the T_1 and T_2 values for melanoma are positioned. The fact that this estimation is only based on one particular case of uveal melanoma though makes the resulting T_1 and T_2 relaxation times not representable in general. Finding general T_1 and T_2 values that are valid for all uveal melanoma characteristics might be even impossible taking into account the diversity of melanoma [31]. To confirm the estimated values, further evaluations would be necessary. This could not be done in the course of this study because no further image sets were available. In vivo T_1 and T_2 measurements of uveal melanoma as demonstrated by Patz et al. for other fine structures in the human eye [44] could allow for even better and more accurate values.

5.2.2 Theoretical Optimization

To maximize the contrast of orbital imaging, especially between uveal melanoma and the vitreous humor, the TFL and TSE sequences were simulated using the methods presented in Section 3.5.4.1. For both simulated sequences the flip angle proved to be of major importance in achieving the perfect contrast between melanoma and vitreous humor and should be chosen wisely. For the TFL sequence a flip angle around 12° showed favorable results and for the TSE the contrast increased with higher flip angles. Thus for the TSE sequence flip angles close to 180° are favorable for optimal contrast between uveal melanoma and vitreous humor. For the TFL sequence the time between the excitation pulse and the first low angle shot TI_1 did not influence the contrast and thus should be chosen as small as possible to keep the acquisition time to a minimum. Varying the TE for the TSE sequence resulted in higher signal for the second echo compared to the first. This can be explained by stimulated echoes that appear starting after the third excitation pulse [52]. Figure 4.11c depicts a very good example why theoretical simulation is very important. At a TR of around 3100 ms vitreous humor and melanoma show similar results and therefore would hardly be discriminable in an image using TR near this value.

The SPACE sequence could not be simulated since the exact formalism that is used for calculating the flip angle train is not documented in the literature and therefore makes a simulation unfeasible. Instead of an mathematical simulation with varying sequence parameters, the sequence was operated at the MR scanner with different TR and TE values. For this experiment pork belly and a bottle of distilled water was used as a phantom. As seen in Figure 4.12 this phantom shows almost the same relationships as the tissue values achieved from the images from University Hospital Essen (Figure 4.6). Therefore pork belly and distilled water represent an adequate phantom for this initial experiment.

Only the fatty tissue showed slightly deviating values, which might be explainable by the firmer structure of the pork belly fat compared to fatty tissue found in the orbital region. For future experiments an enucleated cow or swine eye, including surrounding fatty tissue and eye muscles, would be a more suitable phantom.

5.2.3 Practical Optimization

For ophthalmological MR imaging, acquisition time is one of the key factors in artifact prevention. The longer the scan time, the more artifacts are induced in the resulting image. Therefore, the objective of this present study was to keep the overall scan time of a sequence below 5 min while maximizing SNR, contrast and resolution. Sequences were implemented on the MR scanner (Siemens MAGNETOM Skyra) with parameters as suggested by the simulations. Not all parameter combinations that yielded the best outcome in the simulations were feasible at the scanner. In most cases the closest value to the simulated parameter was chosen. For the TSE sequence intentionally parameters differing from the optimum values according to the simulation were chosen. Due to the fact that in TSE imaging multiple RF pulses are applied in a very short time, SAR can be very high. Reducing the flip angle (<180°) is an effective way to decrease SAR [56–58]. Thus, the refocusing flip angle was set to 135° although in the simulation a value of 180° resulted in a maximal contrast between melanoma and vitreous humor. Also TE was reduced from an optimal value (>200 ms) to 124 ms in order to still provide adequate signals for muscle and fatty tissue as these structures are equally important for clinical diagnostic and planning stereotactic radiotherapy. For the 3D TFL an echo spacing (TI_2) of 7.2 ms was used although the simulation showed better contrast with longer echo spacing. The echo spacing for a given sequence is automatically calculated on the MR scanner software and thus can not be changed directly. For the TFL sequence the same applies for TE, hence the automatically calculated value of 3.1 ms was used for practical implementation. The simulation for variable TE shows the best contrast at low TE values, therefore the automatically calculated value of 3.1 ms is near the optimum. Although in the literature an in plane resolution smaller than 0.5 mm is documented all sequences were implemented using an in plane resolution greater than the values in the literature. The gained SNR by reducing the in plane resolution was invested in reduction of the slice thickness. Slice thicknesses of 1 mm for the TSE and SPACE sequence and 1.25 mm for the TFL sequence were realized. Thin slices are especially important for small melanomas that could be easily missed with thick slices. For the TSE and the TFL sequences a phase oversampling of 24 % and 100 %, respectively were used. Due to the fact that SNR is proportional to $\sqrt{N_{phase}}$, where N_{phase} is the number of phase encoding steps, phase oversampling will increase SNR. Of course with increasing phase encoding steps also the acquisition time will be increased. For the SPACE sequence slice oversampling and two saturation slabs

were used to keep back folding artifacts to a minimum.

Finally sequences were implemented at the MR Scanner of the University Hospital Graz (Siemens MAGNETOM Verio 3 T). Unfortunately the SPACE sequences was not applicable, due to a different software version of the used MR scanner where the SPACE sequence is not available for T_{1w} imaging. The TurboFLASH and the Turbo Spin Echo were implemented with the same sequence parameter as tested on the Siemens MAGNETOM Skyra. First tests on patients, where both sequences where applied in addition to the standard MR protocol, showed promising results. Improvements in over all image quality and anatomical recognizability compared to the images acquired with the currently used 3D FLASH sequence (images see Section 4.2.3.2) were observed. Especially the TFL sequence showed promising results in anatomical recognizability. As seen in Figure 4.15a and Figure 4.15c small structures in the bulb like the lens and the ciliar body are depicted well defined. Also the optic nerve, eye muscles and the surrounding fatty tissue are very good recognizable. TSE images in one patient showed great contrast between vitreous humor and a small melanoma (seen in Figure 4.16b, left eye). Further patients with uveal melanoma, imaged with the current 3D FLASH and the newly optimized TSE and TFL sequences would be necessary to further optimize the sequences and further improve the contrast between melanoma and vitreous humor.

5.3 Triggering of an MR Sequence Using the medEyeTrack System

MR image quality can be substantially reduced by motion artifacts. In particular in ophthalmological MRI these artifacts represent an enormous problem and may hinder a reliable diagnosis. As described by Fanea and Fagan [19], the major source of artifacts are voluntary eye movements and blinking. Several approaches have been demonstrated to minimize artifacts caused by eye movement during the MR examination. Lemke et al. demonstrated a method, where test subjects were asked to relax and look straight ahead and close the eyes just before the start of the measurement, which only achieved limited success [28]. Berkowitz et al. investigated a new approach to prevent artifacts introduced by blinking, that utilized a special cyclic blink protocol where subjects were asked to withhold blinking during a 12 s imaging period and blink to their need in a 3 s rest period [38]. Bert et al. systematically evaluated several approaches to minimize motion artifacts due to eye movements. They found that imaging the eye taped closed with a water-soaked gauze, while the contralateral eye fixated a target, yielded a minimum disturbance from motion artifacts [45]. Authors of several other studies advise the usage of general anesthesia, moderate sedation or local retrobulbar anesthesia in order to keep eye movement to a minimum [28, 29, 32]. This work presents a new and revolutionary

approach to prevent motion artifacts from voluntary movements of the eye by triggering an MR sequence with the medEyeTrack introduced by the Department of Therapeutic Radiology and Oncology (Medical University of Graz) in cooperation with the Institute for Computer Graphics and Vision (Graz University of Technology) and M&R Automation GmbH [49]. Expert evaluation of pictures from 6 test subjects with 6 different eye movement schemes (36 images in total), revealed a significant improvement of triggered images regarding all three judged criteria (overall image quality, anatomical recognizability, artifacts). In addition, also a significant improvement in anatomical recognizability and artifact prevention could be shown with the eye fixation scheme compared to the eyes closed scheme, which highly coincides with the available literature. The quantitative image analysis assessing the gradient entropy metric showed similar results. No significant differences could be shown for the eye fixation scheme compared to the eyes closed scheme and for 20 second untriggered compared to the triggered scheme. However, a clear trend could be observed that the medEyeTrack in combination with a triggered MR sequence can greatly reduce motion artifacts, as seen for the 10 second movement scheme.

In this study the connection between the medEyeTrack and the MRI scanner was realized with an external trigger signal. Due to technical limitations this was the only approach feasible. However a gating solution like described by Ehman et al. [94] in combination with a fast imaging sequence would be a desirable alternative for future experiments to eliminate the dependency on the duration of TR. The choice of an appropriate sequence for the trigger setups is very important. Many of the standard sequences do offer the possibility to enable a variety of trigger options including electrocardiography (ECG), pulse, respiratory and external triggering. Yet, not all sequences which offer the trigger setting do support triggering in practical use. If a sequence does not support triggering huge artifacts will arise and make the image diagnostically unusable. Such an example image of an 3D FLASH sequence not supporting external triggering can be seen in Figure 5.1. This present work used a 3D TurboFLASH sequence, that does support triggering. The cyclic nature of the 3D TurboFLASH sequence, where every imaging cycle can be initiated with a trigger impulse, makes it perfectly applicable for triggering [75]. Sequences with very short TR times are favorable, because during one single TR period no trigger impulse can be processed therefore making an eye movement in this time interval undetectable. Following, eye movement occurring in one single TR interval will still induce unpreventable motion artifacts.

The outcome of ophthalmological MR images also highly depends on the cooperation of the patient [9], therefore two different eye movement schemes with different time intervals, of 10 and 20 seconds, between averting the gaze away from the fixation LED were applied. In addition to these two movement schemes, which were implemented triggered and untriggered, a scheme with eyes closed and one with eyes fixating the LED were employed. The eyes closed scheme was chosen because this approach is currently used at the

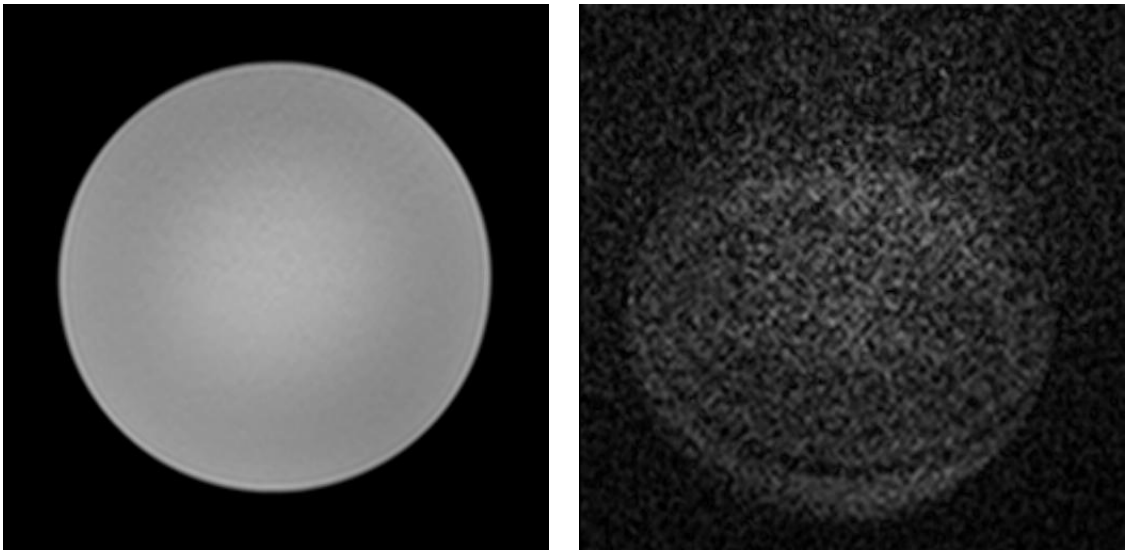

(a) (b)

Figure 5.1: Not all sequences which offer trigger settings do support triggering in practical use. 3D FLASH sequence, measured with a bottle phantom, does not support triggering and results in huge image artifacts (b). Acquisition with identical sequence parameters untriggered (a) does not show any artifacts.

University Hospital Graz with ophthalmological MRI for planning stereotactic radiotherapy. Fixation of the eye is suggested by the literature to result in the least artifact prone images and was therefore also included in this study. Triggering MRI sequences results in a scan time elongation due to induced pauses. With the 10 and 20 second triggered movement schemes the elongation of the 3D TurboFLASH sequences was 17% and 11%, respectively. This elongation has to be taken into consideration when planning the MRI methodology for patients.

For quantitative image analysis a metric called gradient entropy, introduced by McGee et al. [88] was used. This metric found broad use in recent publications in the field of retrospective motion correction of MR images and is the best known metric to detect motion artifacts at present [88, 95]. Ghosting artifacts induced by motion redistribute signals from anatomical regions of the image into the background in phase encoding direction. Hence motion reduces the average anatomical signal and increases the average background pixel intensity [88]. Image entropy as an autocorrection metric favors large homogeneous background areas with pixel values of zero. Ghosting artifacts increase the non zero pixels in the background, thus increase the entropy [96]. The image gradient is minimal for uniform areas (e.g. background) and increases on the edges of areas with different pixel intensity values, so the image gradient basically functions as an edge detection. The gradient entropy is less sensitive to the size of the present edges, but rather sensitive to values near zero. It basically detects how uniform areas are, especially, how uniform the background is [88]. Therefore it requires a significantly large image back-

ground area to work best [96]. The gradient entropy is strongly dependent on the image content, and thus makes a comparison between different test subjects or even between various slices very difficult. Artifacts in the 3D TurboFLASH sequence do not appear uniformly distributed over all reconstructed slices. One slice may present almost no artifacts while the next subsequent slices may show major artifacts. To prevent an influence of gradient entropy by the choice of slice an accumulated gradient entropy was calculated over 20 slices depicting the eye. Further, the gradient entropy was not calculated for the whole image but only for a 40 pixel high band depicting the eye to focus only on eye movement. In order to make a comparison of all 6 test subjects possible, the gradient entropy value of every movement scheme was normalized by the gradient entropy value for the LED fixation scheme since the literature suggests that fixating the eye yields the least amount of motion artifacts [45]. When comparing different test subjects, it is assumed that all detected motion is due to movement of the eye. Therefore, all test subjects carried a personally fitted head mask that was mounted on the medEyeTrack and prevented head motion. Unfortunately, for two test subjects the fitting of the head mask was not perfect and total head immobilization was not given. Therefore these subjects had to be excluded from the quantitative image analysis by gradient entropy. This underlines the essential role of very accurate mask fitting, because smallest movements of the head can induce disturbing artifacts in the acquired images. Also for subsequent radiotherapy an accurately fitted mask is indispensable to ensure localized treatment of only the target region.

The approach of fixating the eyes on a static target like the LED not only results in less artifacts due to reduced voluntary movements it also guarantees a defined eye position, which is reproducible throughout different systems (MRI, CT, LINAC). This is of major importance for radiotherapy treatment planning where CT and MR image data have to be merged together. Ensuring the same eye position on these two imaging systems could greatly benefit the image fusion and dramatically accelerate the radiotherapy treatment planning process. Keeping the eyes closed during measurement can lead to a loss of control over the eye movement and to differences in the orientation of the optic axis of the eyes. Thereby making the image fusion overly complicated. Such a dis-orientation of the optic axis was seen in one proband in form of an inward motion of the bulb (Figure 4.20). Keeping the eyes open can result in susceptibility artifacts at the eye air border region. In order to minimize such artifacts Bert et al. suggested to tape the eyes closed with a water soaked gauze while the contralateral eye fixates a target. Due to the conjugate gaze, eye movement is also reduced for the eye taped close [45]. This methodology was not established in this study but is highly recommended in clinical use to reduce susceptibility artifacts, especially when the anterior part of the eye is the region of interest. The medEyeTrack can not only detect voluntary eye movements but also disease induced drifts of the eye [90] and the MR sequence can then be triggered accordingly. Also

for not triggerable MR sequences the medEyeTrack proved to be very useful in artifact prevention. Fixating the LED yielded the best image rating by evaluators in all three categories and also showed the best outcome with quantitative image analysis. Thus using the medEyeTrack will lead to considerably better image results compared to eyes closed even without triggering the sequence. Further, the medEyeTrack can be used to determine the percentage of image acquisition time the proband fixated the LED. This value allows the establishment of a threshold if a measurement has to be retaken. In this in vivo study the test subjects showed an average percentage of 99% for the LED fixation scheme and 85% and 94% for the 10 second and 20 second schemes, respectively.

Eye blinks represent the most important and dominant source of motion artifacts in clinical ophthalmological MRI [38]. The average time between blinks for men is 2.8 s and for women 4 s with a blink duration varying from 0.3 s to 0.4 s [19] . The current time resolution of the camera system (10 times per second) hinders reliable blinking detection by the medEyeTrack. A next step to detect blinking would be to incorporate a faster camera system with significantly higher time resolution than the average blink duration in order to guarantee the detectability of blinks. Moreover instead of triggered MR sequences, gated sequences should be used where the sequence runs continuously at a present TR and the gating signal is used to determine which k-space lines will be kept and used for image reconstruction. This approach will involve sequence programming and adaption of the currently available gating signal interfaces. Hence the future evaluation of a gating approach should be conducted in cooperation with an MR equipment manufacturer.

5.4 Conclusion

This study was performed to evaluate the achievable motion artifact reduction in ophthalmological MR images obtained by triggered MR sequences using the medEyeTrack system and to advance the current ophthalmological MRI methodology by optimized sequences and choice of appropriate MR imaging coils. This investigation showed a substantial improvement of artifacts and anatomical recognizability in the orbital region for images acquired with triggered MR sequences. All triggered movement schemes showed enhanced outcome in the qualitative as well as in the quantitative image analysis. One shortcoming of this approach was the restriction on the external trigger source, hence the dependency of motion artifact prevention on the TR of the used sequence. Further studies should rather pursue a gating procedure which would be independent of the TR used and would enable nearly continuous prohibition of motion artifacts. Concluding, an application of the medEyeTrack system is highly recommended also in combination with not triggered MR sequences. Not only does it provide a controlled eye position but it further minimizes motion artifacts by eye fixation on the incorporated LED.

Optimizing MR sequences especially for application in ophthalmology has shown great improvements regarding image quality and resolution. The enhancement in resolution and contrast between melanoma and vitreous humor will greatly benefit the classification and treatment planning of occular lesions. First tests in patients are the basis for further improvements of these sequences. As a next step T_1 and T_2 values for uveal melanoma should be quantified in vivo and used for further simulations to maximize the contrast. Further trials with uveal melanoma patients will be necessary to establish and further improve the sequences in clinical use.

The usage of small surface coils for ophthalmologic MRI has shown major SNR enhancement and is therefore highly recommended. Although the handling and manageability of standard small surface coils in everyday clinical use may be quite challenging, the gained SNR highly justifies the usage. The SNR improvement can be invested in faster acquisition time or higher resolution images, both of which can improve the outcome of ophthalmological MR substantially. Several manufacturers nowadays offer specially developed orbit coils which allow easier and faster handling. In future studies the evaluation of such coils is recommended.

Bibliography

[1] Wolffsohn JS Peterson RC. Anterior ophthalmic imaging. *Clinical and Experimental Optometry*, 89(4):205–214, 2006.

[2] Fink W. Refractive correction method for digital charge-coupled device-recorded scheimpflug photographs by means of ray tracing. *Journal of biomedical optics*, 10(2):024003–0240036, 2005.

[3] Linnola RJ, Findl O, Hermann B, Sattmann H, Unterhuber A, Happonen RP, Drexler W. Intraocular lens–capsular bag imaging with ultrahigh-resolution optical coherence tomography: Pseudophakic human autopsy eyes. *Journal of Cataract & Refractive Surgery*, 31(4):818–823, 2005.

[4] Foster FS, Pavlin CJ, Harasiewicz KA, Christopher DA, Turnbull DH. Advances in ultrasound biomicroscopy. *Ultrasound Med. Biol.*, 26(1):1–27, 2000.

[5] Stachs O, Martin H, Behrend D, Schmitz KP, Guthoff R. Three-dimensional ultrasound biomicroscopy, environmental and conventional scanning electron microscopy investigations of the human zonula ciliaris for numerical modelling of accommodation. *Graefe's Archive for Clinical and Experimental Ophthalmology*, 244(7):836–844, 2006.

[6] Nayak BK, Desai S, Maheshwari S, others . Interpretation of magnetic resonance imaging of orbit: Simplified for ophthalmologists (part i). *Journal of Clinical Ophthalmology and Research*, 1(1):29, 2013.

[7] Lemke AJ, Kazi I, Felix R. Magnetic resonance imaging of orbital tumors. *Eur Radiol*, 16(10):2207–2219, Oct 2006.

[8] Langner S, Krüger PC, Stachs O, Hosten N. MR-Mikroskopie des humanen Auges. *Tumor-Diagnostik & Therapie*, 34(01):39–44, 2013.

[9] de Graaf P, Göricke S, Rodjan F, Galluzzi P, Maeder P, Castelijns JA, Brisse HJ. Guidelines for imaging retinoblastoma: imaging principles and mri standardization. *Pediatric radiology*, 42(1):2–14, 2012.

[10] Dieckmann K, Bogner J, Georg D, Zehetmayer M, Kren G, Pötter R. A linac-based stereotactic irradiation technique of uveal melanoma. *Radiotherapy and Oncology*, 61(1):49–56, 2001.

[11] Alai-Omid M. *Untersuchungen des Auges mit einer Oberflächenspule in einem 3-Tesla-MRT*. PhD thesis, Berlin, Charite , Univ.-Med., Diss., 2010, 2010.

[12] Schünke M. *Prometheus Kopf und Neuroanatomie.* Thieme Georg Verlag, 2005.

[13] Bron A, Tripathi R, Tripathi B. *Wolff's Anatomy of the Eye and Orbit Eight edition.* CRC Press, 1998.

[14] Poloschek CM, Lagrèze WA, Ridder GJ, Hader C. Klinische und neuroradiologische Diagnostik bei Orbitatumoren. *Der Ophthalmologe*, 108(6):510–518, 2011.

[15] Hosten N. *Auge und Orbita.* Thieme, 1995.

[16] Zhou Q. *Die Rolle der orbitalen MRT in der Differentialdiagnose von Erkrankungen der Augenmuskeln, des extrakonalen und subperiostalen Kompartimentes.* PhD thesis, Humboldt-Univ., 2003.

[17] Zalpour C. *Für die Physiotherapie: Anatomie Physiologie: Lehrbuch für Physiotherapeuten, Masseure, medizinische Bademeister und*

Sportwissenschaftler. Urban & Fischer im. Elsevier, 2006.

[18] Malhotra A, Minja FJ, Crum A, Burrowes D. Ocular anatomy and cross-sectional imaging of the eye. *Semin Ultrasound CT MR*, 32(1):2–13, Feb 2011.

[19] Fanea L Fagan AJ. Review: Magnetic resonance imaging techniques in ophthalmology. *Molecular vision*, 18:2538, 2012.

[20] Smith TB Nayak KS. MRI artifacts and correction strategies. *Imaging*, 2(4):445–457, 2010.

[21] McRobbie DW, Moore EA, Graves MJ, Prince MR. *MRI from Picture to Proton*. Cambridge University Press, 2007.

[22] Erasmus LJ, Hurter D, Naudé M, Kritzinger HG, Acho S. A short overview of MRI artefacts. *South African Journal of Radiology*, 8(2):13–17, 2004.

[23] Weishaupt D, Koechli VD, Marincek B. *Wie funktioniert MRI? Eine Einfü hrung in Physik und Funktionsweise der Magnetresonanzbildgebung (German Edition)*. Springer, 2009.

[24] Townsend KA, Wollstein G, Schuman JS. Clinical application of MRI in ophthalmology. *NMR Biomed*, 21(9):997–1002, Nov 2008.

[25] Mafee MF, Rapoport M, Karimi A, Ansari SA, Shah J. Orbital and ocular imaging using 3- and 1.5-T MR imaging systems. *Neuroimaging Clin N Am*, 15(1):1–21, Feb 2005.

[26] Kazi I, Felix R, Lemke AJ. Orbitaerkrankungen und ihr Erscheinungsbild in der MRT. *Radiologe*, 45:783–789, 2005.

[27] Weigel M, Lagreze WA, Lazzaro A, Hennig J, Bley TA. Fast and quantitative high-resolution magnetic resonance imaging of the optic nerve at 3.0 tesla. *Invest Radiol*, 41(2):83–86, Feb 2006.

[28] Lemke AJ, Alai-Omid M, Hengst SA, Kazi I, Felix R. Eye imaging with a 3.0-T MRI using a surface coil–a study on volunteers and initial patients with uveal melanoma. *Eur Radiol*, 16(5):1084–1089, May 2006.

[29] de Graaf P, Barkhof F, Moll AC, Imhof SM, Knol DL, van der Valk P, Castelijns JA. Retinoblastoma: MR imaging parameters in detection of tumor extent. *Radiology*, 235(1):197–207, Apr 2005.

[30] Lemke AJ, Hosten N, Bornfeld N, Bechrakis NE, Schüler A, Richter M, Stroszczynski C, Felix R. Uveal melanoma: correlation of histopathologic and radiologic findings by using thin-section mr imaging with a surface coil. *Radiology*, 210(3):775–783, Mar 1999.

[31] Lemke AJ, Hosten N, Wiegel T, Prinz RD, Richter M, Bechrakis NE, Foerster PI, Felix R. Intraocular metastases: differential diagnosis from uveal melanomas with high-resolution mri using a surface coil. *Eur Radiol*, 11(12):2593–2601, 2001.

[32] Schüler AO, Hosten N, Bechrakis NE, Lemke AJ, Foerster P, Felix R, Foerster MH, Bornfeld N. High resolution magnetic resonance imaging of retinoblastoma. *Br J Ophthalmol*, 87(3):330–335, Mar 2003.

[33] Lemke AJ, Kazi I, Hosten N, Bechrakis NE, Foerster MH, R F. Evaluierung der MR-Volumetrie kleiner Volumina am Beispiel von Augentumoren mittels Phantomuntersuchungen. *Fortschr Röntgenstr*, 175:958–962, 2003.

[34] Lemke AJ, Kazi I, Mergner U, Foerster PI, Heimann H, Bechrakis N, Schüler A, von Pilsach MIS, Foerster M, Felix R, Hosten N. Retinoblastoma - MR appearance using a surface coil in comparison with histopathological results. *Eur Radiol*, 17(1):49–60, Jan 2007.

[35] Galluzzi P, Hadjistilianou T, Cerase A, De Francesco S, Toti P, Venturi C. Is CT still useful in the study protocol of retinoblastoma? *AJNR. American journal of neuroradiology*, 30:1760–1765, 2009.

[36] Razek AAKA Elkhamary S. MRI of retinoblastoma. *Br J Radiol*, 84(1005):775–784, Sep 2011.

[37] De La Garza BH, Muir ER, Shih YI, Duong TQ. 3D magnetic resonance microscopy of the ex vivo retina. *Magn Reson Med*, 67(4):1154–1158, Apr 2012.

[38] Berkowitz BA, McDonald C, Ito Y, Tofts PS, Latif Z, Gross J. Measuring the human retinal oxygenation response to a hyperoxic challenge using MRI: eliminating blinking artifacts and demonstrating proof of concept. *Magn Reson Med*, 46(2):412–416, Aug 2001.

[39] Zhang Y, Nateras OSE, Peng Q, Kuranov RV, Harrison JM, Milner TE, Duong TQ. Lamina-specific anatomic magnetic resonance imaging of the human retina. *Invest Ophthalmol Vis Sci*, 52(10):7232–7237, Sep 2011.

[40] Erb-Eigner K, Warmuth C, Taupitz M, Willerding G, Bertelmann E, Asbach P. Impact of magnetic field strength and receiver coil in ocular MRI: a phantom and patient study. *Rofo*, 185(9):830–837, Sep 2013.

[41] Richdale K, Wassenaar P, Teal Bluestein K, Abduljalil A, Christoforidis J, Lanz T, Knopp M, Schmalbrock P. 7 tesla MR imaging of the human eye in vivo. *J Magn Reson Imaging*, 30(5):924–932, Nov 2009.

[42] Fea AM, Annetta F, Cirillo S, Campanella D, De Giuseppe M, Regge D, Grignolo FM. Magnetic resonance imaging and orbscan assessment of the anterior chamber. *J Cataract Refract Surg*, 31(9):1713–1718, Sep 2005.

[43] Beenakker JWM, van Rijn GA, Luyten GPM, Webb AG. High-resolution MRI of uveal melanoma using a microcoil phased array at 7T. *NMR Biomed*, 26(12):1864–1869, Dec 2013.

[44] Patz S, Bert RJ, Frederick E, Freddo TF. T1 and T2 measurements of the fine structures of the in vivo and enucleated human eye. *J Magn Reson Imaging*, 26(3):510–518, Sep 2007.

[45] Bert RJ, Patz S, Ossiani M, Caruthers SD, Jara H, Krejza J, Freddo T. High-resolution MR imaging of the human eye 2005. *Acad Radiol*, 13(3):368–378, Mar 2006.

[46] Langmann G, Pendl G, Klaus-MŸllner , Papaefthymiou G, Guss H. Gamma knife radiosurgery for uveal melanomas: an 8-year experience. *J Neurosurg*, 93 Suppl 3:184–188, Dec 2000.

[47] Modorati G, Miserocchi E, Galli L, Picozzi P, Rama P. Gamma knife radiosurgery for uveal melanoma: 12 years of experience. *Br J Ophthalmol*, 93(1):40–44, Jan 2009.

[48] Wackernagel W, Holl E, Tarmann L, Avian A, Schneider MR, Kapp K, Langmann G. Visual acuity after gamma-knife radiosurgery of choroidal melanomas. *Br J Ophthalmol*, 97(2):153–158, Feb 2013.

[49] M&R Automation GmbH . Eye-Tracker ermöglicht neuartige Behandlungsverfahren bei Augen-Tumoren. *Human Technology Styria, Botenstoff*, pages 11 –12, 2013.

[50] Hennig J, Nauerth A, Friedburg H. RARE imaging: a fast imaging method for clinical MR. *Magn Reson Med*, 3(6):823–833, Dec 1986.

[51] Hennig J, Weigel M, Scheffler K. Multiecho sequences with variable refocusing flip angles: optimization of signal behavior using smooth transitions between pseudo steady states (TRAPS). *Magn Reson Med*, 49(3):527–535, Mar 2003.

[52] Bernstein MA, King KF, Zhou ZJ. *Handbook of MRI pulse sequences*. Elsevier, Amsterdam, Boston, Heidelberg, 2004.

[53] Meiboom S Gill D. Modified Spin-Echo method for measuring nuclear relaxation times. *Review of Scientific Instruments*, 29(8):688–691, 1958.

[54] Constable RT, Anderson AW, Zhong J, Gore JC. Factors influencing contrast in fast spin-echo MR imaging. *Magn Reson Imaging*, 10(4):497–511, 1992.

[55] Mulkern RV, Melki PS, Jakab P, Higuchi N, Jolesz FA. Phase-encode order and its effect on contrast and artifact in single-shot RARE sequences. *Med Phys*, 18(5):1032–1037, 1991.

[56] Alsop DC. The sensitivity of low flip angle RARE imaging. *Magn Reson Med*, 37(2):176–184, Feb 1997.

[57] Hennig J Scheffler K. Easy improvement of signal-to-noise in RARE-sequences with low

refocusing flip angles. rapid acquisition with relaxation enhancement. *Magn Reson Med*, 44(6):983–985, Dec 2000.

[58] Hennig J Scheffler K. Hyperechoes. *Magn Reson Med*, 46(1):6–12, Jul 2001.

[59] Mugler JP. Optimized three-dimensional fast-spin-echo MRI. *J Magn Reson Imaging*, 00:000 – 000, Jan 2014.

[60] Scott KT Schmeets SH. SPACE: An innovative solution to rapid, low SAR, T2-weighted contrast in 3D spin echo imaging. *MAGNETOM FLASH*, 2:92 – 95, February 2005.

[61] Mugler JP, Bao S, Mulkern RV, Guttmann CRG, Jolesz FA, Brookeman JR. Three-dimensional spin-echo-train proton-density-weighted imaging using shaped signal evolutions. In *Proceeding of the 7th Annual Meeting of ISMRM, Philadelphia*, 1999. (abstract 1631).

[62] Mugler JP, Kiefer B, Brookeman JR. Three-dimensional T2-weighted imaging of the brain using very long spin-echo trains. In *Proceeding of the 8th Annual Meeting of ISMRM, Denver*, 2000. (abstract 687).

[63] Mugler JP, Bao S, Mulkern RV, Guttmann CR, Robertson RL, Jolesz FA, Brookeman JR. Optimized single-slab three-dimensional spin-echo MR imaging of the brain. *Radiology*, 216(3):891–899, Sep 2000.

[64] Wielopolski P, Achten E, Groot JCd. A dual echo tree-dimensional inversion recovery HASTE sequence: initial experience and potential applications for the quantification of white matter lesions and brain tissue volumes. In *Proceedings of the 4th Annual Meeting of ISMRM, New York*, 1996. (abstract 554).

[65] Mugler J, Brookeman JR, Mulkern RV, Guttmann CRG, Jolesz FA. Tingle-slab three-dimensional spin-echo-based pulse sequences for high-resolution T1-weighted and T2-weighted imaging of the brain. In *Proceeding of the 5th Annual Meeting of ISMRM, Vancouver, BC Canada*, 1997. (abstract 137).

[66] Hennig J. Multiecho imaging sequences with low refocusing flip angles. *J Magn Reson*, 78(3):397–407, July 1988.

[67] Busse RF, Hariharan H, Vu A, Brittain JH. Fast spin echo sequences with very long echo trains: design of variable refocusing flip angle schedules and generation of clinical T2 contrast. *Magn Reson Med*, 55(5):1030–1037, May 2006.

[68] Mugler JP Brookeman JR. Efficient spatially-selective single-slab 3D turbo-spin-echo imaging. In *Proceeding of the 12th Annual Meeting of ISMRM, Kyoto, Japan*, 2004. (abstract 695).

[69] Haase A, Frahm J, Matthaei D, HŠnicke W, Merboldt KD. FLASH imaging: rapid NMR imaging using low flip-angle pulses. *J Magn Reson*, 67(2):258–266, Dec 1986.

[70] Brant-Zawadzki M, Gillan GD, Nitz WR. MP RAGE: a three-dimensional, T1-weighted, gradient-echo sequence–initial experience in the brain. *Radiology*, 182(3):769–775, Mar 1992.

[71] Haase A. Snapshot FLASH MRI. applications to T1, T2, and chemical-shift imaging. *Magn Reson Med*, 13(1):77–89, Jan 1990.

[72] Holsinger AE Riederer SJ. Variable flip angle snapshot GRASS imaging. In *Proceeding of the 9th Annual Meeting of ISMRM, New York*, 1990. (abstract 453).

[73] Atkinson DJ, Burstein D, Edelman RR. First-pass cardiac perfusion: evaluation with ultrafast MR imaging. *Radiology*, 174(3 Pt 1):757–762, Mar 1990.

[74] Runge VM. *The Physics of Clinical MR Taught Through Images*. Thieme, 2004.

[75] Mugler JP Brookeman JR. Three-dimensional magnetization-prepared rapid gradient-echo imaging (3D MP RAGE). *Magn Reson Med*, 15(1):152–157, Jul 1990.

[76] Brix G, Schad LR, Deimling M, Lorenz WJ. Fast and precise T1 imaging using a TOMROP sequence. *Magn Reson Imaging*, 8(4):351–356, 1990.

[77] Epstein FH, Mugler JP, Brookeman JR. Optimization of parameter values for complex pulse sequences by simulated annealing: application to 3D MP-RAGE imaging of the brain. *Magn Reson Med*, 31(2):164–177, Feb 1994.

[78] Mugler JP, Epstein FH, Brookeman JR. Shaping the signal response during the approach to steady state in three-dimensional magnetization-prepared rapid gradient-echo imaging using variable flip angles. *Magn Reson Med*, 28(2):165–185, Dec 1992.

[79] National Electrical Manufacturers Association . *Determination of Signal-to-Noise and Ratio (SNR) and in Diagnostic and Magnetic Resonance and Imaging*, 2008.

[80] Nishimura D. *Principles of Magnetic Resonance Imaging*. Lulu.com, 2010.

[81] Majumdar S, Orphanoudakis SC, Gmitro A, O'Donnell M, Gore JC. Errors in the measurements of T2 using multiple-echo MRI techniques. i. effects of radiofrequency pulse imperfections. *Magn Reson Med*, 3(3):397–417, Jun 1986.

[82] Hargreaves BA, Vasanawala SS, Pauly JM, Nishimura DG. Characterization and reduction of the transient response in steady-state MR imaging. *Magn Reson Med*, 46(1):149–158, Jul 2001.

[83] Quinsten AS, Blex S, Keiper SL, Nicola Goericke. Optimized examination technique reduces examination time for children with retinoblastoma by half. *MAGNETOM Flash*, 2:68–73, 2011.

[84] Stanisz GJ, Odrobina EE, Pun J, Escaravage M, Graham SJ, Bronskill MJ, Henkelman RM. T1, T2 relaxation and magnetization transfer in tissue at 3T. *Magn Reson Med*, 54(3):507–512, Sep 2005.

[85] de Bazelaire CMJ, Duhamel GD, Rofsky NM, Alsop DC. Mr imaging relaxation times of abdominal and pelvic tissues measured in vivo at 3.0 T: preliminary results. *Radiology*, 230(3):652–659, Mar 2004.

[86] Bottomley PA. Human in vivo NMR spectroscopy in diagnostic medicine: clinical tool or research probe? *Radiology*, 170(1 Pt 1):1–15, Jan 1989.

[87] Lorenzato C, Cernicanu A, Meyre ME, Germain M, Pottier A, Levy L, de Senneville BD, Bos C, Moonen C, Smirnov P. MRI contrast variation of thermosensitive magnetoliposomes triggered by focused ultrasound: a tool for image-guided local drug delivery. *Contrast Media Mol Imaging*, 8(2):185–192, 2013.

[88] McGee KP, Manduca A, Felmlee JP, Riederer SJ, Ehman RL. Image metric-based correction (autocorrection) of motion effects: analysis of image metrics. *J Magn Reson Imaging*, 11(2):174–181, Feb 2000.

[89] R Core Team . *R: A Language and Environment for Statistical Computing*. R Foundation for Statistical Computing, Vienna, Austria, 2013. http://www.R-project.org.

[90] Yarbus AL. *Eye Movements and Vision*. Plenum Press New York, 1967. Section: Eye movements during fixation on stationary objects and saccadic eye moevements. Pages 103 - 146.

[91] Dietrich O, Raya JG, Reeder SB, Reiser MF, Schoenberg SO. Measurement of signal-to-noise ratios in MR images: influence of multichannel coils, parallel imaging, and reconstruction filters. *J Magn Reson Imaging*, 26(2):375–385, Aug 2007.

[92] Stollberger R Wach P. Imaging of the active B1 field in vivo. *Magn Reson Med*, 35(2):246–251, Feb 1996.

[93] HR H, WG B, CJ L. *MRI: The Basics*. Lippincott Williams & Wilkins, 2010.

[94] Ehman RL, McNamara MT, Pallack M, Hricak H, Higgins CB. Magnetic resonance imaging with respiratory gating: techniques and advantages. *AJR Am J Roentgenol*, 143(6):1175–1182, Dec 1984.

[95] Loktyushin A, Nickisch H, Pohmann R, Schölkopf B. Blind retrospective motion cor-

rection of MR images. *Magn Reson Med*, 70(6):1608–1618, Dec 2013.

[96] Atkinson D, Hill DL, Stoyle PN, Summers PE, Keevil SF. Automatic correction of motion artifacts in magnetic resonance images using an entropy focus criterion. *IEEE Trans Med Imaging*, 16(6):903–910, Dec 1997.

List of Figures

List of Tables